Miniature Magnetic Sensors

by

Saman Nazari Nejad

A thesis
presented to the University of Waterloo
in fulfillment of the
thesis requirement for the degree of
Doctor of Philosophy
in
Electrical and Computer Engineering

Waterloo, Ontario, Canada, 2015

©Saman Nazari Nejad 2015

AUTHOR'S DECLARATION

I hereby declare that I am the sole author of this thesis. This is a true copy of the thesis, including any required final revisions, as accepted by my examiners.

I understand that my thesis may be made electronically available to the public.

Abstract

Magnetic sensors are widely used in nearly all engineering and industrial sectors, including high-density magnetic recording, navigation, target detection, anti-theft systems, non-destructive testing, magnetic labeling, space research, and bio-magnetic measurements in the human body. Miniature magnetic sensors with high sensitivity are particularly advantageous in biomedical and specialized industrial applications.

Amongst the various extant magnetic sensors, Micro-Electro-Mechanical System (MEMS) and Giant Magneto impedance (GMI) sensors have the ability to sense low levels of magnetic field in the order of 10 millitesla as well as the space to be further miniaturized. In this thesis, MEMS and GMI sensors are studied in detail both theoretically and experimentally. Multiphysics analyses have been developed to provide a path to further investigate these two types of sensors for various sensor configurations. Several prototype units are successfully developed, fabricated and tested to verify the validity of these models.

MEMS reed sensors consist of tri-layer beams of Au/Ni/Au. The actuation of these sensors is initiated by the magnetic force to maintain the continuity of magnetic field streamlines. The Ni layer is deployed as the main magnetic core, and the gold layers are used to enhance the contact quality of the switches. In this work, a unique fabrication process is developed that significantly reduces the number of masking and lithography steps. As well, a detailed finite element method is presented to study the behavior of these sensors and to optimize the device performance. The FEM study considers various magnetic environments, providing a performance map for the sensors. Having a performance map is essential for a system's operation and for tracking its operational behavior. The study also considers the effects of various device formations and packaging for these types of sensors. The generated magnetic force is observed to be much higher than the required mechanical force for device actuation.

The GMI sensors exhibit many advantages over their conventional counterparts. In particular, thermal stability and high sensitivity make GMI sensors attractive candidates for a wide range of applications. The GMI sensors are based on concepts different from those for conventional giant magneto resistance (GMR) sensors. GMI sensors have been under active research only in the past decade. In this thesis, thin film multilayer GMI sensors are realized using microfabrication technology. The fabricated sensors are tri-layers of $Co_{73}Si_{12}B_{15}$ /Au./ $Co_{73}Si_{12}B_{15}$ The thin film GMI sensors are studied in detail using FEM simulation, and several sensors are developed, fabricated and tested to work in the millitesla range. A post-processing step is proposed to optimize the performance of GMI

sensors and to enhance their magnetic sensitivity. The post-processing characterization shows that annealing the devices with a specific annealing cycle has the optimal effect of enhancing the magnetic characteristics of CoSiB. The sensors are treated with this post-processing recipe, demonstrating a considerable increase in their magneto impedance (MI) ratio. The research has made a contribution to establishing the engineering foundation toward the development of low-cost miniature GMI magnetic sensors for low field intensity applications.

Acknowledgements

I wish to express my sincere appreciation and gratefulness to my advisor Professor Raafat R. Mansour for his knowledge, insight, valuable guidance, and continuous encouragement throughout this research. He is always there when I need help. His advices always helped me not just in my thesis but in all aspects of my life. Indeed, my gratitude to him cannot be expressed in a few words and it is my honor to be his student.

I am grateful to Professor Edmond Cretu from University of British Columbia who served as the external examiner of this thesis and provided constructive feedback. I am also grateful to the members of my PhD examination committee, Professor Eihab Abdel-Rahman, Professor John Yeow, Professor Simarjeet Saini,and Professor Siva Sivoththaman for their time and effort to improve the quality of this thesis.

I am thankful to all members of the Centre for Integrated RF Engineering (CIRFE) research group not only for their invaluable technical assistance but also for creating a warm, friendly, and welcoming environment. In particular, Dr. Arash Akhavan Fomani has significantly contributed to the outcome of this research through many stimulating discussions.
I am indebted to many wonderful friends who have supported me even in the cold rainy days of my PhD studies. They have been always there to lend me a helping hand and made my time at Waterloo an enjoyable experience full of unforgettable memories. I would also like to recognize my colleagues Dr. Siamak Fouladi, Dr. Sara Sharifian Attar, Dr. Neil Sarak, Dr. Scott Chen, Dr. Hassan Mahboubi, Mostafa Azizi, Oliver Wong, Ahmed Abdel Aziz, Bill Joley and Maziar Moradi.

I would also like to thank my officemate Grigory Chugunov, who made our office enjoyable for long stays. Without him, the PhD days would not be fun at all. I also need to thank my friend Dr. Soheil Kolouri, without him my life would have been all dark and boring.

Extended thanks go to my Mom and Dad for their support and patience during my education life. They taught me how to start with A,B,C and finish with a Ph.D dissertation. I will never forget their endless support and kindness and I cannot be thankful enough for their sacrifices. I am thankful to my caring brother and sister, Soheil and Sara, they always ignite hope in me whenever I feel hopeless.
Last but not the least, a world of thanks goes to my friend and colleague, my love and my wife, Narges Fallahi, who stood behind me throughout this journey. I am really grateful to her collaboration, enthusiasm and support. Without her hopeful vision on the down days of my research and encouragements on the up days, this work would be far from completion.

Dedication

To my beautiful wife, Narges Fallahi

To my Mom and Dad, Farahnaz Aghili and Rahman Nazari Nejad

Table of Contents

AUTHOR'S DECLARATION ii
Abstract iii
Acknowledgements v
Dedication vi
Table of Contents vii
List of Figures ix
List of Tables xv
Chapter 1 Introduction 1
1.1 Motivation 3
1.2 Objectives 4
1.3 Thesis Outline 5
2 Chapter Two Literature Survey 6
2.1 Conventional Magnetic Sensors 6
2.1.1 Induction Sensors 6
2.1.2 Fluxgate Sensors 7
2.1.3 Magnetoresistors 9
2.1.4 Hall Effect Sensors 10
2.1.5 SQUID Sensors 12
2.1.6 Magnetodiode and Mangetotransistor Sensors 13
2.1.7 MEMS-Based Magnetic Sensors 14
2.1.8 Giant Magneto-Impedance Sensors 17
3 Chapter Three Multilayer MEMS Reed Sensors 20
3.1 Introduction 20
3.1.1 Theory 21
3.2 Nickel-based Magnetic MEMS Reed Sensors 23
3.2.1 Modeling and FEM Simulation 23
3.2.2 Design and Mask-Making 33
3.2.3 Fabrication Process 36
3.2.4 Experimental Setup and Measurements 45
3.3 Tri-layer Magnetic MEMS Reed Sensors 46
3.3.1 Modeling and FEM Simulation 47

3.3.2 Design Rules and Fabrication Process ... 57
3.3.3 Test and Experiment ... 62
4 Chapter Four Giant Magneto-Impedance Thin film Magnetic Sensors ... 64
4.1 Introduction ... 64
4.2 Theory ... 65
4.3 COMSOL FEM Simulation ... 72
4.3.1 Study the effect of thickness ... 79
4.4 Fabrication Process ... 80
4.4.2 Test Setup and Measurement ... 84
5 Chapter Five Characterization of GMI material- CoSiB ... 99
5.1 Introduction ... 99
5.2 Fabrication and Post-Processing ... 100
5.3 Magnetic Characterizations ... 101
5.3.1 Permeability Measurement ... 102
5.3.2 Hysteresis Loop and Magnetization ... 104
5.3.3 Magnetization of CoSiB Layer in a layered structure ... 106
5.4 Material Characterizations ... 107
5.4.1 Raman Spectroscopy ... 107
5.4.2 X-Ray Diffraction ... 109
5.4.3 Energy Dispersive X-Ray Spectroscopy ... 111
5.5 Results and Discussion ... 113
5.6 Experimental Tests on Tri-Layer Thin Film GMI Sensors ... 114
6 Chapter Six Conclusions and Future Plans ... 117
6.1 Future Works ... 118
Appendix A ... 120
Theory and mathematical equations for MEMS REED Sensors ... 120
Appendix B ... 130
Appendix C ... 132
Detailed Microfabrication recipe used for MEMS Reed sensors ... 132
Bibliography ... 137

List of Figures

Figure 1-1 Comparison between magnetic sensors working range [1]. 2
Figure 2-1 The basic fluxgate principle. The ferromagnetic core is excited by the ac current Iexc of frequency f into the excitation winding. The core permeability μ(t) is therefore changing with 2f frequency. If the measure dc field B0 is present, the associated core flux Φ(t) is also changing with 2f, and voltage Vind is induced in the pickup (measuring) coil having N turns. 7
Figure 2-2 Simplified fluxgate waveforms (a) in the zero field and (b) with measured field H0. 8
Figure 2-3 Orientation of the magnetization of the ferromagnetic layers in a GMR spin valve for different external fields H. (a) H = 0, the magnetization of the free ferromagnetic layer is perpendicular to the magnetization of pinned ferromagnet, R = R(0). (b) Low resistant state, H parallel to the magnetization of the pinned ferromagnet, R < R(0). (c) High resistant state, H directed opposite to the magnetization of the pinned ferromagnet, R > R(0). (d) H large enough to unpin the pinned ferromagnet, R < R(0). 9
Figure 2-4 (a) Schematic of Hall Effect sensors and (b) examples of Hall Effect products. 11
Figure 2-5 Schematic of SQUID sensor. 12
Figure 2-6 Schematic of a SQUID magnetometer. 13
Figure 2-7 Picture showing the concept of the MEMS flux concentrator. Note that there is a space between the substrate and the flux concentrators on the MEMS flaps [15]. 15
Figure 2-8 (a) SEM microphotograph of a magnetic switch, (b) zoomed-in view of the contact part [10]. 16
Figure 2-9 CMOS-MEMS magnetometer systems with integrated magnetic coil [41] 17
Figure 2-10 A Co-wire GMI sensor reported in [43] 18
Figure 2-11 Schematic view of GMI element (a) top view (b) cross sectional view [38]. 19
Figure 3-1 Schematic view of undeformed magnetic switch and a deformed one [8]. 22
Figure 3-2 Modeled magnetic MEMS switch in COMSOL 4.2 GUI. 25
Figure 3-3 Meshing of modeled magnetic MEMS switch. 27
Figure 3-4 Shows the magnetic flux density in Tesla for case a). 28
Figure 3-5 Shows magnetic flux density contours for magnetic switches. 29
Figure 3-6 Magnetic flux density streamlines between the beams for case a). 30
Figure 3-7 Whole magnetic model of the switches in the environment. 30
Figure 3-8 Shows the magnetic flux density in Tesla for case b). 31
Figure 3-9 Magnetic flux density contours for case b). 32

Figure 3-10 Magnetic flux density streamlines between the beams for case b). 32
Figure 3-11 Actuation of switch at 10 mT. 33
Figure 3-12 Final mask printed on glass. 36
Figure 3-13 The passivation dielectric layer above silicon substrate.. 37
Figure 3-14 Cr/Gold seed layer after patterning. 37
Figure 3-15 Bottom electrode fabricated on top of the substrate. 37
Figure 3-16 Patterned anchor (the gold layer on top of PI is not shown to prevent misunderstanding). 38
Figure 3-17 Wafer after patterning anchor and dimples on PI. 38
Figure 3-18 Final structure before release. 39
Figure 3-19 Optical image of switch type 1 – simple cantilever. 39
Figure 3-20 Optical image of switch type 2 – minder hinge switches. 40
Figure 3-21 Optical image of switch type 3 – narrow cantilever with wider tips. 40
Figure 3-22 Optical image of switch type 4 – two-array switches.. 40
Figure 3-23 Optical image of switch type 4 – four-arrays switches. 41
Figure 3-24 Optical image of tip of one cantilever showing the position of the upper beam with respect to the lower one; dimples and release holes are shown here. 41
Figure 3-25 Magnetic Reed SW- a) minder shape support SW – width 60um and length 380 um b)SW – width 80um and length 400 um. 42
Figure 3-26 An Array of 2 Magnetic Reed SW – width 60um and length 370 um. 43
Figure 3-27 An Array of 2 Magnetic Reed SW – width 60um and length 370 um (side view). 44
Figure 3-28 Magnetic Reed SW type 2 – width 60um and length 270 um. 44
Figure 3-29 Magnetic Reed SW with wide tip type 3 – width (w1: 20um, w2:60um) and length 500um. 45
Figure 3-30 Photo of measurement setup and stage... 46
Figure 3-31- The COMSOL geometry 2D sketch of MEMS read switches, for a a)tri-layer without packaging, b) tri-layer with glass packaging and c) nickel tip gold beams with the packaging 49
Figure 3-32 the 2D COMSOL simulation for a tri-layer MEMS without packaging, this graph illustrates the vertical displacement of sensors beams in actuated condition (10 mT magnetic field). As shown above, the upper beam is experiencing a 4 um downward displacement which is 4 times greater than our 1 um designed gap. 50

Figure 3-33 Surface plot of magnetic field on Tri-layer MEMS Reed switch with packaging, as shown above, the sensing magnetic field for the actuation is 9-11 mT. 51
Figure 3-34 the surface plot of upper beam vertical displacement. 52
Figure 3-35 magnified projected out of place displacement of both beams. The blue color is corresponded to upper beam with the downward movement whereas the red on is corresponded to the upward movement of the bottom electrode 53
Figure 3-36 Simulation setup and 3D geometric design of MEMS read sensors. 54
Figure 3-37 Magnetic field distribution over sensor in an actuation step. 55
Figure 3-38 Generated force eon the upper beam. In the positions with negative value the actuation will happen. In this figure x axis represents x direction and the unit is micro meter. 56
Figure 3-39 Working map of the MEMS Reed sensors, a) when the poles of permanent magnet are in line with longitude direction of the sensor and its moving in that direction, b) when the pole of permanent magnet are perpendicular to the longitude direction of sensors and c) when the permanent magnet is in line with the sensor but it's moving out of the plane far from sensor. 57
Figure 3-40 Fabrication steps of trilayer MEMS Reed switches 58
Figure 3-41 Optical microscopic image of trilayer MEMS Reed sensors a) 60
Figure 3-42 Optical microscopic image of trilayer MEMS Reed sensors b) 61
Figure 3-43 Optical microscopic image of trilayer MEMS Reed sensors c) 62
Figure 3-44 Summary of MEMS reed sensor actuation test 63
Figure 4-1 Schematic drawing of multilayer MI element, a) cross sectional view b)top view [37]. ... 66
Figure 4-2 Plots of the MI ratio vs. reduced frequency $\mathbf{v = \omega\omega\delta}$ for a number of parameters $\mathbf{d1/d}$ in (a) and $\mathbf{\sigma1/\sigma2}$ in (b).Typical parameters used for calculation are: $\mathbf{4\pi Ms = 6000\ G, HK = 9\ Oe, \sigma2 = 4.5 \times 1016\ s - 1}$. To avoid the divergence of $\mathbf{\mu t}$ at $\mathbf{Hex = HKand\ \omega = 0}$, a small anisotropy deviation in 5° from y-axis is introduced, the spin relaxation constant is taken to be 0.2. These magnetic parameters are used for all of the calculations [32]. 69
Figure 4-3 The MI ratio as a function of $\mathbf{Hex}$ for two frequencies v=0.04 and v=0.16, d=0.1um, $\mathbf{\sigma2 = 1.7 \times 1017s - 1}$and $\mathbf{\sigma1\sigma2 = 12}$(related to NiFe/Cu/NiFe) [32]. 70
Figure 4-4 Plots of the MI ratio vs. frequency with the film width as a parameter: d=0.5 um and d_1=d_2. The calculation is related to CoFeSiB/Cu/CoFeSiB films [37] 71
Figure 4-5- The calculated dependence of μ'; the real part of effective permeability, on applied external magnetostatic field H_{ext} 72
Figure 4-6 The calculated dependence of μ"; the imaginary part of effective permeability, on H_{ext} ... 73

Figure 4-7 Circumferential magnetic flux of the sensor at 1 MHz 74
Figure 4-8 Current density distribution along the cross section under the external field of 2400 A/m 75
Figure 4-9 Simulation results for impedance of the GMI sensor at 200 kHz 76
Figure 4-10 Simulation results for impedance of the GMI sensor at 500 kHz 77
Figure 4-11 Simulation results for impedance of the GMI sensor at 1 MHz 78
Figure 4-12 The impedance of sample for different ac frequencies under various external magnetic fields 78
Figure 4-13 Left) impedance of R-50-30 GMI sensor with 2 um thickness at 1 MHz, Right) impedance of R-50-30 GMI sensor with 1 um thickness at 1 MHz, ... 79
Figure 4-14 Left) impedance of GMI sensor with 2 um thickness at 500 kHz, Right) impedance of GMI sensor with 1 um thickness at 500 kHz, ... 79
Figure 4-15 Fabrication process sequence of GMI samples. 81
Figure 4-16 Undercut of CoSiB sample. 82
Figure 4-17 A view of one batch of fabricated sensors. Two categories of devices are shown in this figure. 83
Figure 4-18 Various types of minder shape GMI sensors. 83
Figure 4-19 DC probes and measuring the variation of impedance under magnetic field in GMI samples. 84
Figure 4-20 Schematic of measurement setup. 85
Figure 4-21 The measurement setup. 85
Figure 4-22 Impedance magnitude and phase of Device R10-40-1. 86
Figure 4-23 Impedance magnitude of Device R10-40-1 at1 and 10 MHz. 87
Figure 4-24 Impedance magnitude of Device 50-30 at1 and 10 MHz. 87
Figure 4-25 Schematic of magnetization process in magneto-thermal annealing step 89
Figure 4-26 Measured impedance of two different GMI devices with different dimensions. As expected, the sensor demonstrates a substantial increase in impedance at higher excitation frequencies. 90
Figure 4-27 Wheatstone bridge and DUT in final sensor. 91
Figure 4-28 Impedance of GMI sample, R-50-30, measured in different magnetic fields in a frequency sweep of 150 Hz to 10 MHz 92
Figure 4-29 Measured impedance for R-50-30 (this is the same sample as previous section) at constant external magnetic fields over a frequency sweep 93

Figure 4-30 The measured impedance for GMI R-50-30 which suing both measurement methods.... 94
Figure 4-31 A comparison of 3D simulation for GMI R-50-30 and the measured impedances captured with Impedance analyzer (Blue) and Oscilloscope (Red) 95
Figure 4-32 Measured impedance for R-50-30 (this sample is post process at the optimal processing condition) at constant external magnetic fields over a frequency sweep 96
Figure 4-33 Impedance of R-50-30 sample annealed in optimized condition.................................... 96
Figure 4-34 Comparison of experimental measurement and simulation results for frequency range of 1 MHz to 10 MHz. 97
Figure 4-35 Maximum GMI as a Function of frequncy 98
Figure 5-1 The relative permeability of samples thermally treated for 3 h; (b) the same for samples annealed for 4 h. 102
Figure 5-2 (a) The relative permeability of samples treated magneto-thermally for 3 h; (b) the same for samples annealed for 4 h. 102
Figure 5-3 (a) The hysteresis loop of samples thermally treated for 3 h; (b) the same samples annealed for 4 h. The square marker shows the loop for the process with the highest permeability, and the triangle marker is for the after fabrication (AF) sample. 105
Figure 5-4 (a) The hysteresis loop of samples magneto-thermally treated for 3 h; b) the same annealed for 4 h. The square marker shows the loop for the process with the highest permeability, and the triangle marker is for the after fabrication (AF) sample. 105
Figure 5-5 Schematic of annealing magnetization under a magneto-thermal post-process. It is shown how the Weiss walls are breaking up and letting the domains be aligned to the external field. 107
Figure 5-6 Raman spectroscopy for thermal post-processed samples. 108
Figure 5-7 Raman spectroscopy for magneto-thermal post-processed samples. 108
Figure 5-8 XRD graphs of samples thermally treated for 3 and 4 h. 110
Figure 5-9 XRD graph of samples magneto-thermally treated for 3 and 4 h. 110
Figure 5-10 EDX graph of a sample magneto-thermally treated for 3 h at 600 °C. It should be noted the same graph is captured for all other samples. 112
Figure 5-11 GMI thin film samples fabrication process flow a) sputtering and patterning of CoSiB b) Deposition and patterning of Metal trace layer c) sputtering and patterning of CoSiB d) A 1-inch to 1-inch die of glass wafer, containing the thin film GMI samples. 115
Figure 5-12 Measurement results of GMI R-50-30 in 500 kHz ac current. 116
Figure 6-1 The three basic subdomains typically present at magnetic MEMS [8]............................ 121

Figure 6-2 Various configurations of a deformed body [8]. 124
Figure 0-1 Bottom electrode design rules. 130
Figure 0-2 Dektak of first layer (Ni) with 0.5KÅ tip, in the above fig , 6 units are covered which results to 3 um 133

List of Tables

Table 1-1 Category of Magnetic Sensor Applications [1] 3
Table 3-1 Lithography mask layers 35
Table 3-2 Layer Names, Thicknesses, and Mask Levels 35
Table 4-1 Impedance Values for GMI R-50-30 at 500 kHz Measured with Agilent Impedance Analyzer 93
Table 4-2Measured Values for GMI R-50-30 in Oscilloscope Measurement of Impedance 94
Table 5-1 High Peaks of The Relative Permeability for Different Post-Processing Conditions 103
Table 5-2 X-Ray Diffractometer Parameters 109
Table 5-3 EDX Captured Quantitative Results. The Main Elements are Highlighted 112

Chapter 1
Introduction

For decades, magnetic sensors have helped humans analyze and control thousands of applications. Computers have nearly unlimited memory through the use of magnetic sensors in magnetic storage disks and tape drives. Airplanes experience enhanced levels of safety because of the reliability of noncontact switching employing magnetic sensing. Factories have improved productivity because of the precise stability and low cost of magnetic sensors. There are many ways to sense magnetic fields, most of which are based on the intimate connection between magnetic and electric phenomena. A common priority of magnetic sensors in all applications is that magnetic sensors provide a stronger, more reliable, and more maintenance-free technology compared to other sensor technologies [1-4].

A magnetic sensor is a system or device that can measure the magnitude of a magnetic field or each of its vector components. Magnetic sensors can be classified into scalar magnetometers and vector magnetometers according to whether they measure the magnitude or the vector components of the magnetic field. The techniques usually encompass many aspects of physics and electronics.

Magnetic sensing techniques exploit a broad range of ideas and phenomena from the fields of physics and material science. The common technologies used for magnetic field sensing include induction coil sensors, fluxgate, optically pumped nuclear precession, superconducting quantum interference device (SQUID), Hall Effect, giant magnetoresistance, magnetic tunnel junctions, giant magnetoimpedance, magnetodiode and magnetotransistor, fiber optic and magneto-optic, and microelectromechanical systems (MEMS)-based magnetic sensors. A list of the most commonly used magnetic sensor technologies is given in Fig. 1.1, in which the sensitivities of these sensors are indicated [1].

Magnetic Sensor Technology		Detectable Field (gauss)				
		10^{-10}	10^{-6}	10^{-2}	10^{2}	10^{6}
1	Coil Magnetometers					
2	Fluxgate					
3	Optically Pumped					
4	Nuclear-Precession					
5	SQUID					
6	Hall Effect					
7	Magnetoresistive					
8	Magnetodiode					
9	Magnetotransistor					
10	Magneto Optical					
11	Giant Magneto Impedance					
12	MEMS Reed Switches					

Figure 1-1 **Comparison between magnetic sensors working range [1].**

As can be seen, magnetic sensors have a broad range of applications (Table 1.1) [1]. For example, ultra-sensitive magnetic sensors are able to detect tiny magnetic fields produced outside the brain by neuronal currents, which can be used for diagnostic applications. High reliability non-contact switching with magnetic sensors leads to enhanced safety standards in aircraft, and magnetic sensors are also used in automobiles to detect positions in the engine crank shaft and wheel braking. Computers have nearly unlimited memory through the application of magnetic sensors in magnetic storage hard drives and tape drives.

Table 1-1 **Category of Magnetic Sensor Applications [1]**

<table>
<tr><th colspan="2">1E-9T</th><th colspan="2">1E-4T</th></tr>
<tr><th>Category 1</th><th colspan="2">Category 2</th><th>Category 3</th></tr>
<tr><th>High Sensitivity</th><th colspan="2">Medium Sensitivity</th><th>Low Sensitivity</th></tr>
<tr><td>Definition:
Measuring field gradients or differences due to induced (in Earth's field) or permanent dipole moments</td><td colspan="2">Definition:
Measuring perturbations in the magnitudes and/or direction of Earth's fields due to induced or permanent dipoles</td><td>Definition:
Measuring fields stronger than Earth's magnetic field</td></tr>
<tr><td>Major Applications:
Brain function mapping magnetic anomaly detection</td><td colspan="2">Major Applications:
Magnetic compass

Munitions fusing

Mineral prospecting</td><td>Major Applications:
Noncontact switching
Current measurement
Magnetic memory readout</td></tr>
<tr><td>Most Common Sensor:
SQUID
Optically pumped</td><td colspan="2">Most Common Sensor:
Coil magnetometer
Flux-gate
Magnetoresistive</td><td>Most Common Sensor:
Coil magnetometer
Hall-Effect Sensor
Magnetoresistive</td></tr>
</table>

1.1 Motivation

In light of magnetic sensors' nearly limitless applications, a magnetic sensor with a working range in millitesla would be in high demand. This magnetic field range has applications in various industries, such as biomedical devices, communication systems, and automobile and airplane industries [1], [21], [27]. Indeed, the high demand for this range has been the driving motivation for this thesis, the intent of which is to generate new magnetic sensors and applications in the millitesla range. As shown in Figure 1-1 and discussed in Chapter 2, MEMS technology magnetic sensors and GMI (giant-magneto impedance) magnetic sensors are able to perform well and accurately in this range.

MEMS technology magnetic sensors normally use a mechanical moveable part to sense the magnetic field, while the GMI type show a change in their impedance based on their materials and are

fabricated using thin film technology. In this study, both MEMS and GMI sensors are designed, fabricated, and tested.

1.2 Objectives

The major objectives of this Ph.D. thesis work are:

- The development of miniature MEMS reed magnetic sensors.

There is a limited number of publications about MEMS reed magnetic sensing. Moreover, those MEMS reed magnetic sensors have a minimum length of 1000 microns and their beams have a relatively large width of hundreds of microns. Based on the simulation results generated, their sensitivity can increase by changing the beams' thicknesses. Hence, the size of the devices was reduced by an order of 5 to 10, and the devices were fabricated as small as 20 to 80 um in width and 100 to 400 um in length. This reduction in size will ultimately help us offer an array of magnetic sensors with the same area as conventional magnetic sensors. The finite element (FE) simulations for this study are conducted in COMSOL Multiphysics. The simulations are done in 2D and 3D, and take into consideration the packaging effects.

- The development of thin film GMI magnetic sensors using CoSiB/Au/CoSiB GMI multilayer: Proposing a new method of magnetizing the ferromagnetic layer.

Very few publications have, to date, reported on GMI magnetic sensors. The reported GMI magnetic sensors have been fabricated using a costly sputtering system, which prepares a high magnetic field around the sample during the fabrication process. Preparing this magnetic field is essential in order to direct (orientation and magnetization) the GMI. However, because of the physics inherent in sputtering devices and their architecture, only a few research groups have access to the equipment. Based on our preliminary research, we determined that the fabrication of ferromagnetic material can be done in a normal conventional sputtering system. A new post-processing step is proposed in which the sample needs to be annealed in an oven with the presence of a magnetic field. During this annealing step, the magnetic domains of ferromagnetic material should lose their magnetic walls and become oriented in the same direction as the exerted magnetic field. Applying this process will reduce the cost and workload of the fabrication process.

- The study of the thermal and magneto-thermal treatment on CoSiB and metallic glass GMI materials.

In this study, various mechanical and material characterization tests are used to understand the effects of thermal and magneto-thermal treatment on GMI materials. These tests are followed by detailed magnetic characterization tests, which offer us conclusions on optimal treatment.

1.3 Thesis Outline

In the second chapter of this thesis, popular sensor technologies are described in detail. In Chapter 3, work on magnetic MEMS reed sensors is explained. The theory of these sensors is reviewed and verified using finite element multiphysics COMSOL simulations. Two different types of 2D and 3D simulations with and without the packaging effects are studied, and a sensor performance map is generated. Various types of devices are designed, and a fabrication process is developed for them. As well, devices are fabricated and a test setup developed. At the end of the chapter, the test results are discussed and compared to simulations.

Chapter 4 demonstrates some recent work on GMI magnetic sensors. In the first section, the theory of GMI sensors is reviewed and the design of our sensors is discussed. A general 3D simulation is presented for these sensors. Throughout the rest of the chapter, a custom-made test setup is designed and the experimental results of the fabricated sensors are reviewed.

Chapter 5 focuses on the material characterization and study of the effects of thermal and magneto-thermal treatments on CoSiB and metallic glass GMI materials. In the chapter, various GMI samples are prepared and undergo annealing with different situations. A comparison and study of the results of both material and magnetic test show us how to optimize the post-processing treatment to reach optimal performance of GMI sensors.

At the end of this thesis, Chapter 6 summarizes the results and discusses the study's conclusions. Finally, future work and future challenges are presented.

2 Chapter Two

Literature Survey

2.1 Conventional Magnetic Sensors

2.1.1 Induction Sensors

The principal of induction sensors is Faraday's law of induction, i.e., if the magnetic flux through a coiled core changes, a voltage proportional (emf) to the rate of change of the flux (Φ) is generated between its leads:

$$emf = -\frac{d\phi}{dt} = -\frac{d(NA\mu_0\mu_r(t)H(t))}{dt} \quad (1.1)$$

where N is the turns of the coil, A is the core cross-section area, H is the magnetic field in the sensor core, and $\mu_r(t)$ is the sensor core relative permeability (the core may be ferromagnetic or air).

Thus, we can write the general equation for induction sensors as [2]:

$$emf = -[\frac{NA\mu_0\mu_r d(H(t))}{dt} + \frac{NH\mu_0\mu_r d(A(t))}{dt} + \frac{NA\mu_0 H d(\mu_r(t))}{dt}] \quad (1.2)$$

Basic induction coils are based on the first term of Eq. 1.2. The middle term describes rotating coil sensors, where A(t) is the effective area in the plane perpendicular to the measured field. The last term is the basic fluxgate equation (fluxgate sensors are covered in next section).

To improve the sensitivity, a rod of a ferromagnetic material with a high magnetic permeability is typically inserted inside the coil to gather the surrounding magnetic field and increase the flux density B (Φ = BA). The sensitivity depends on the permeability of the core material, the area of the coil, the number of turns, and the rate of change of the magnetic flux through the coil.

In geophysics, these types of sensors serve to measure micropulsations of the Earth's magnetic field (1 mHz-1 Hz frequency range); in audio frequency applications, they are also used in magnetic recording techniques. However, limitations in sensitivity and size prevent them from being used in applications that require high resolution and small volume.

2.1.2 Fluxgate Sensors

The last term of Eq. 1.2 is the basis for fluxgate sensors. Fluxgate sensors measure the magnitude and direction of the DC or low-frequency AC magnetic field in the range of approximately 10-9 to 10-4 T. The frequency response of the sensor is limited by the excitation field and the response time of the ferromagnetic material. The basic sensor principle is illustrated in Fig. 2-1 [2].

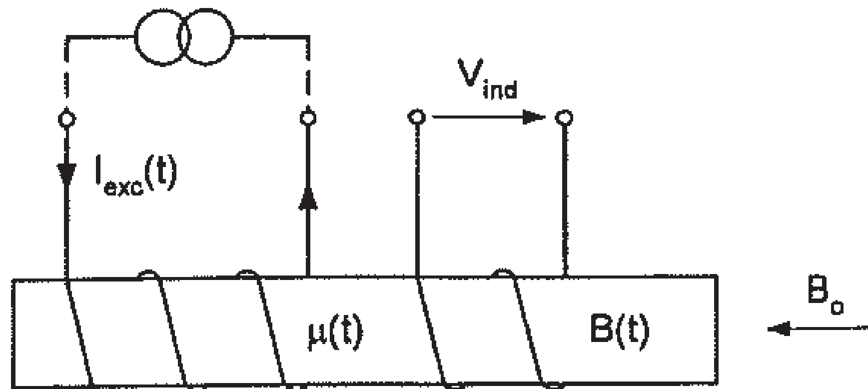

Figure 2-1 The basic fluxgate principle. The ferromagnetic core is excited by the ac current Iexc of frequency f into the excitation winding. The core permeability μ(t) is therefore changing with 2f frequency. If the measure dc field B0 is present, the associated core flux Φ(t) is also changing with 2f, and voltage Vind is induced in the pickup (measuring) coil having N turns.

The soft magnetic material of the sensor core is periodically saturated in both polarities by the AC excitation field, which is produced by the excitation current Iexc through the excitation coil. Thus, the core permeability changes, and the DC flux associated with the measured DC magnetic field B0 is modulated. The "gating" of the flux that occurs when the core is saturated gives the device its name. Figure 2-2 shows simplified corresponding waveforms [2]. The device output is usually the voltage VI induced into the sensing (pickup) coil at the second (or even higher) harmonic of the excitation frequency. This voltage is proportional to the measured field.

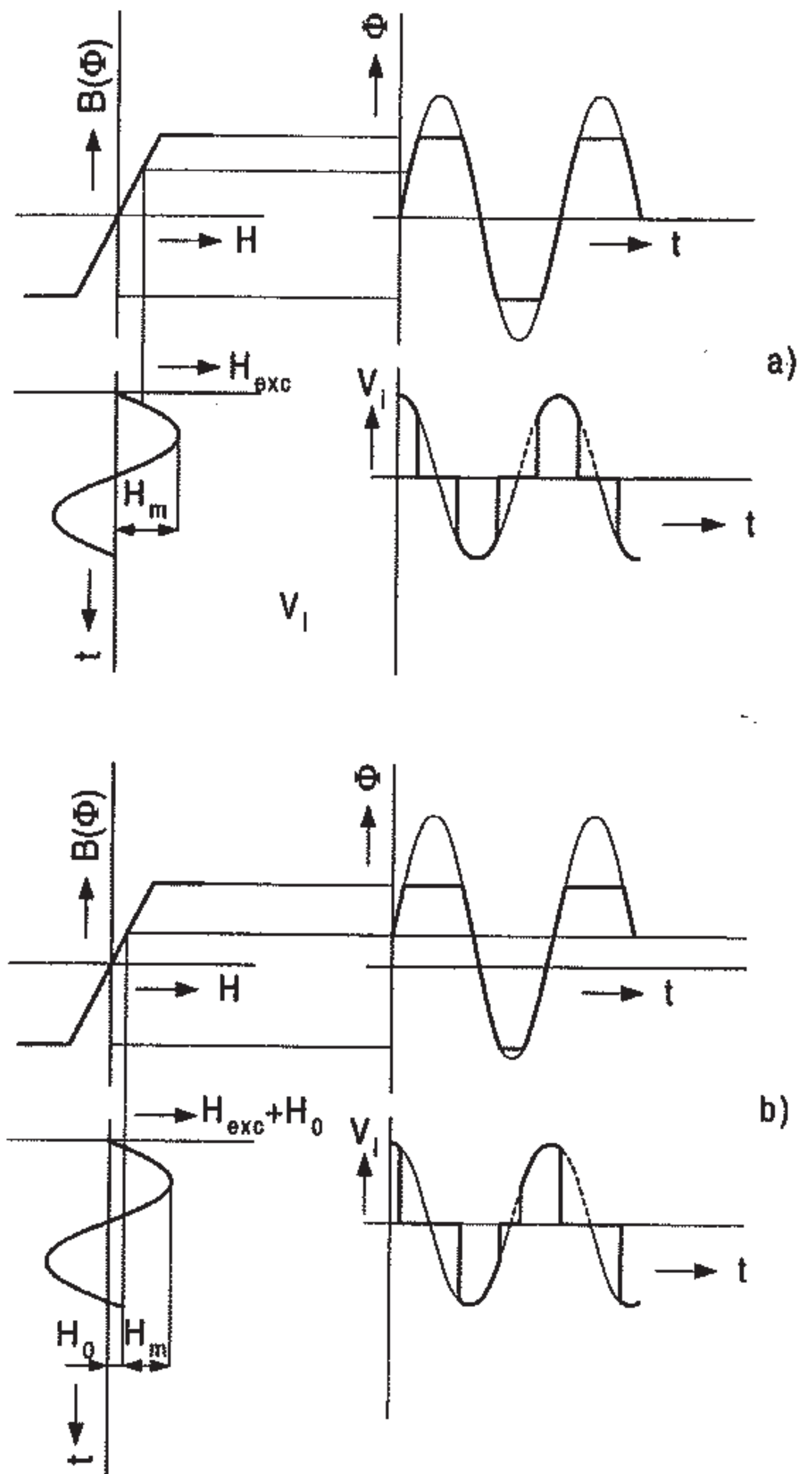

Figure 2-2 Simplified fluxgate waveforms (a) in the zero field and (b) with measured field H0.

2.1.3 Magnetoresistors

Magnetoresistive magnetometers use a change in resistance ΔR caused by an external magnetic field H. A giant magnetoresistive (GMR) could be achieved by using a four-layer structure that consists of two thin ferromagnets separated by a conductor (Fig. 2-3) [1].

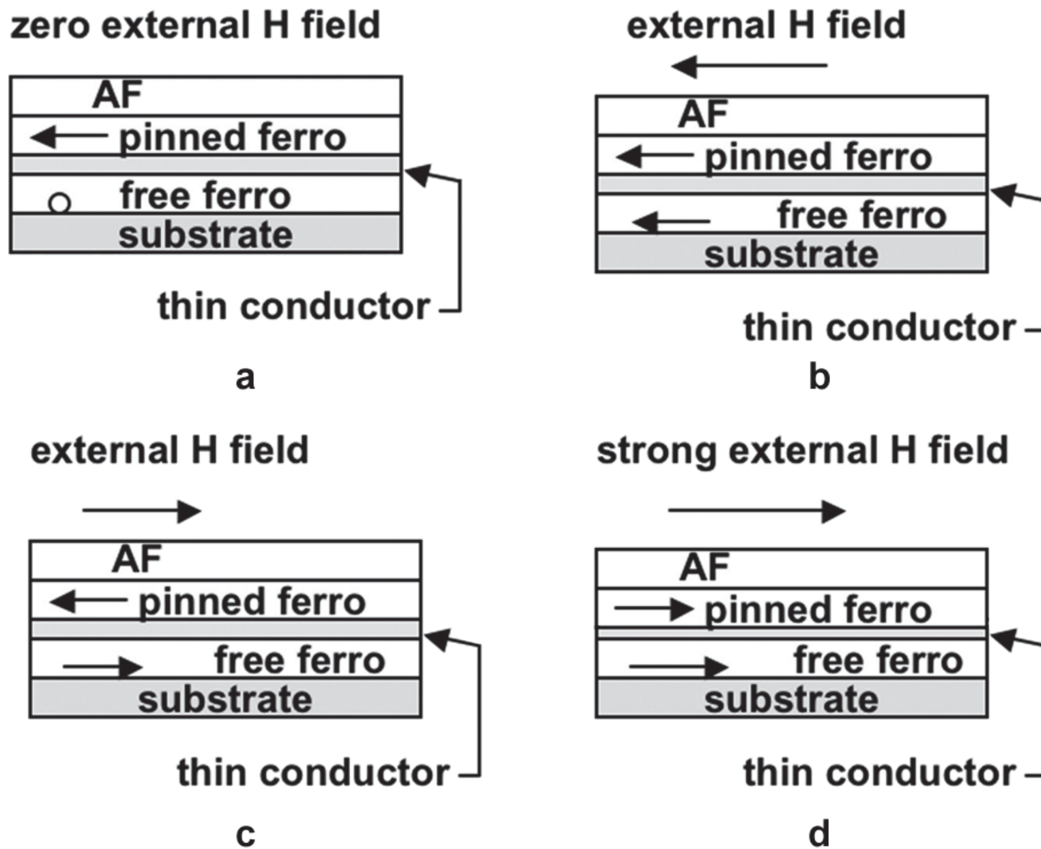

Figure 2-3 Orientation of the magnetization of the ferromagnetic layers in a GMR spin valve for different external fields H. (a) H = 0, the magnetization of the free ferromagnetic layer is perpendicular to the magnetization of pinned ferromagnet, R = R(0). (b) Low resistant state, H parallel to the magnetization of the pinned ferromagnet, R < R(0). (c) High resistant state, H directed opposite to the magnetization of the pinned ferromagnet, R > R(0). (d) H large enough to unpin the pinned ferromagnet, R < R(0).

Magnetoresistive magnetometers are very attractive for low-cost applications. So far, GMR sensors can detect from 10-8 T at 1 Hz to as large as 0.1 T.

2.1.4 Hall Effect Sensors

As shown in Fig. 2-4, Hall Effect sensors are a widely-used, low-cost sensor [1]. In the Hall Effect, a voltage difference appears across a thin rectangle of conductor placed in an external magnetic field perpendicular to the plane of the rectangle when an electric current is sent along its length. The principal of Hall Effect is the Lorentz force, which is proportional to the velocity of the particles,

$$F = Bqv \tag{1.3}$$

An electric field produced by the accumulated charges is built to balance the Lorentz force,

$$F = Eq \tag{1.4}$$

If the velocity of the moving charges and the built electric field are known, the magnetic field can be obtained.

The Hall Effect is quite small in metallic conductors but significantly larger in semiconductors. This discrepancy in sizing arises from the density of carriers being much lower in semiconductors and the velocity of carriers being much faster in semiconductors in obtaining the same current. The silicon devices have a sensitivity range of 10-3 T to 0.1 T, and the sensitivity of indium anti-monide sensors can reach as low as 10-7 T.

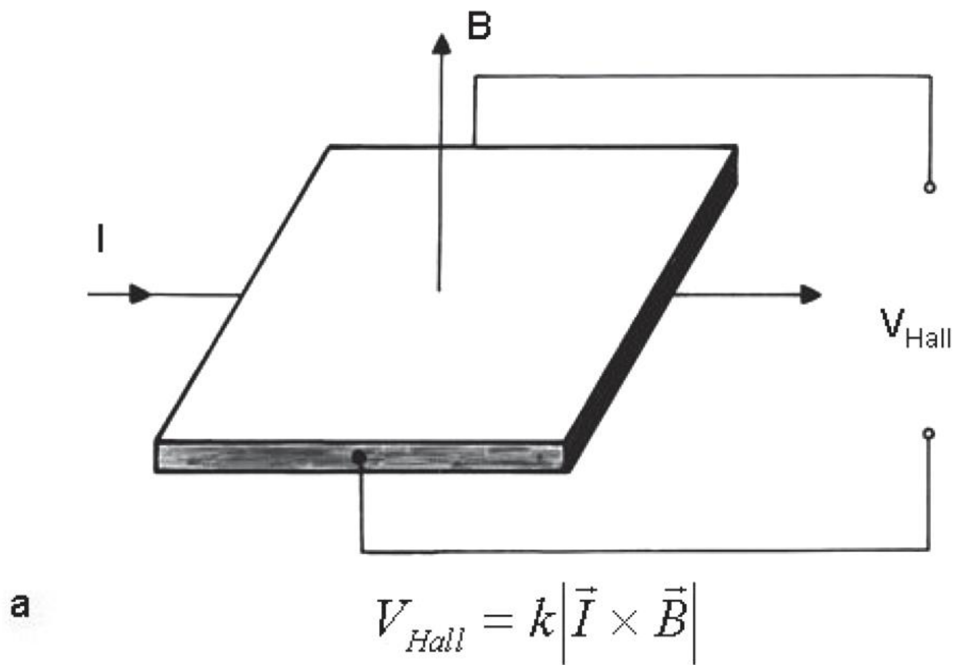

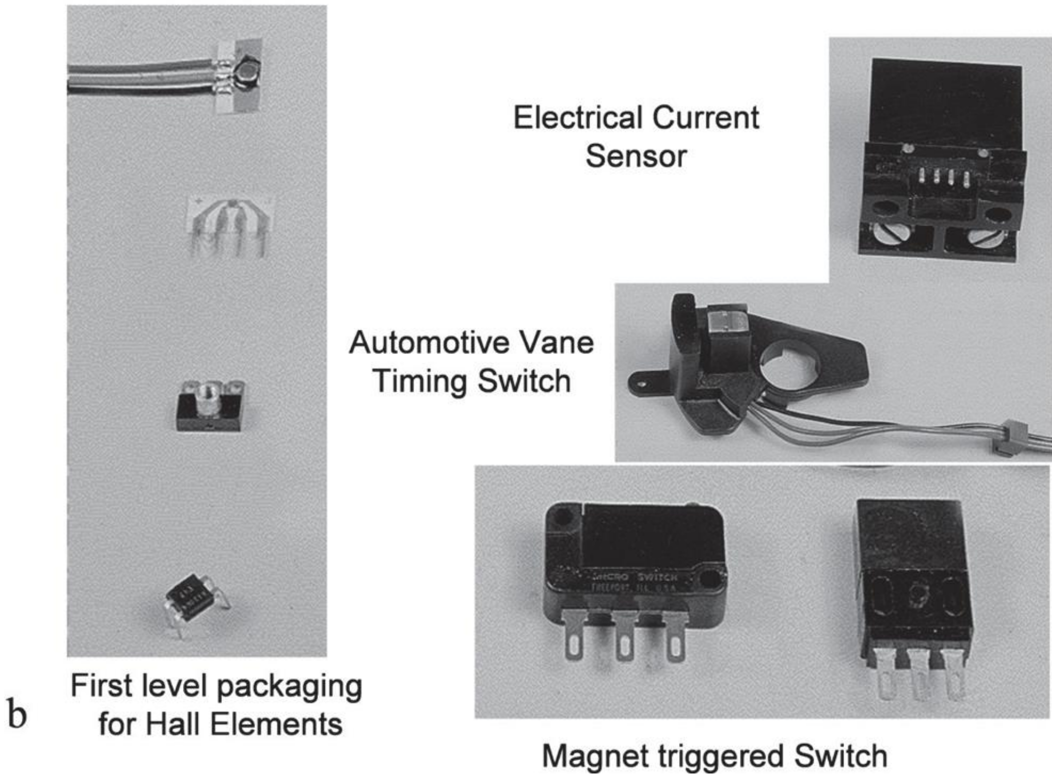

Figure 2-4 (a) Schematic of Hall Effect sensors and (b) examples of Hall Effect products.

2.1.5 SQUID Sensors

Superconducting quantum interference devices (SQUIDs) are the most sensitive of all instruments for measuring a magnetic field at low frequencies (<1 Hz). An example of a SQUID is illustrated in Fig. 2-5 [1]. The principle is based on the remarkable interactions of observed electric currents and magnetic fields when certain materials are cooled below a superconducting critical temperature. Below this critical temperature, the materials become superconductors and lose all resistance to the flow of electricity. The critical current of the SQUID is related to the external magnetic field (Fig. 2-5).

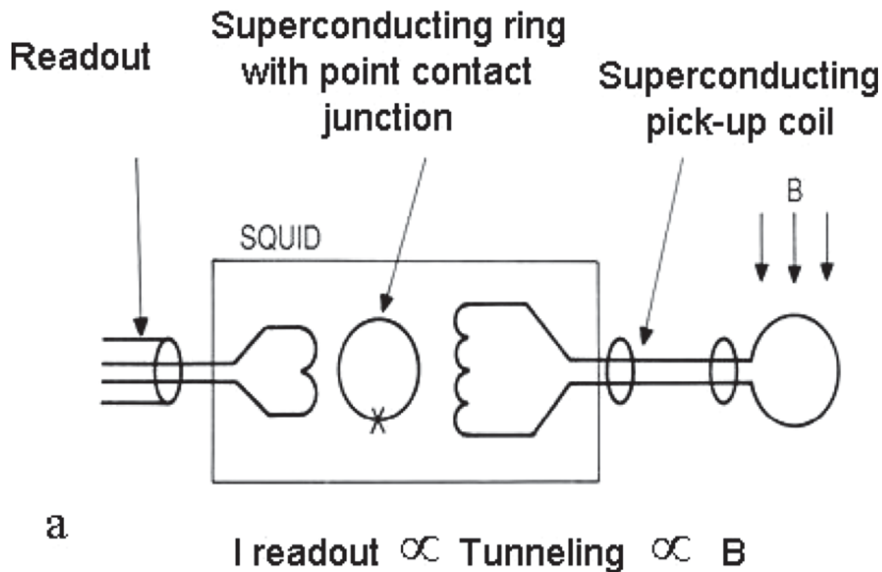

Figure 2-5 Schematic of SQUID sensor.

The typical sensitivity of SQUIDs is in the order of 10 fT. However, both the maintaining fee and the instrument are very expensive, which prevents their popular application. Figure 2-6 shows a SQUID setup.

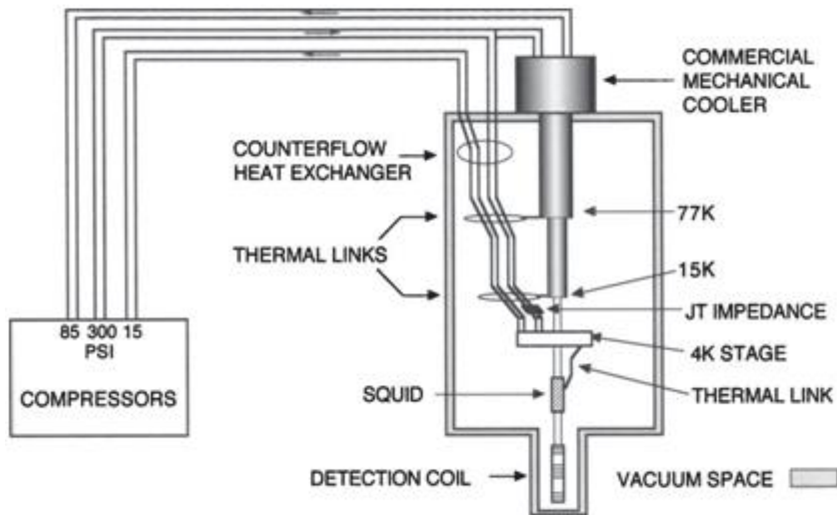

Figure 2-6 Schematic of a SQUID magnetometer.

2.1.6 Magnetodiode and Mangetotransistor Sensors

A magnetodiode is essentially a semiconductor diode, or pn junction. In a magnetodiode, however, the p region is separated from the n region by an area of undoped silicon. The device is fabricated by depositing silicon and then silicon dioxide on a sapphire substrate. If a metal contact on the p-doped region is given a positive potential and a metal contact on the n-doped region is given a negative potential, holes in the p-doped material and electrons in the n-doped material will be injected into the undoped silicon [1,3]. The current is the sum of the hole current and the electron current. Some of the carriers, particularly those near the interface between the silicon and the silicon dioxide or near the interface between the silicon and the sapphire, will recombine. The loss of charge carriers increases the resistance of the material. In the absence of a field, recombination at both interfaces contributes to the resistance.

Perpendicular to the direction of travel of the charge carriers, a magnetic field deflects them either up or down, depending on the direction of the field. Both holes and electrons are deflected in the same direction because they are traveling in opposite directions. Charge carriers near the interface between the silicon and the sapphire have a greater tendency to recombine than those near the interface between the silicon and the silicon dioxide. Thus, if the magnetic field deflects the charge carriers down, the resistance of the material is increased; if it deflects them up, the resistance is decreased. The response of a magnetodiode to a magnetic field is about ten times larger than the

response of a silicon Hall Effect device [1-3]. Devices in this method are normally used as magnetically actuated (amplified) diodes rather than sensors [1].

A magnetic field sensor was introduced at 1983 having a lateral bipolar magnetotransistor with a single emitter region and whose base region is incorporated as a well in the surface of a silicon substrate of the reverse material conduction type [58]. A magnetotransistor is an ordinary bipolar transistor so optimally designed that its electrical output characteristics, e.g. its collector current Ic or its current amplification factor, are highly sensitive to the strength and orientation of a magnetic field.[58] Known magnetotransistors have a voltage sensitivity ranging from 10 Volts/Tesla to 500 Volts/Tesla or a relative-current sensitivity ranging from 20%/Tesla to 30%/Tesla and preferably employ lateral bipolar transistors.[58]

2.1.7 MEMS-Based Magnetic Sensors

Many of the earliest designs of magnetic sensors utilized simple magnetic attraction to ferrous objects. The resulting motion was then measured to record or detect metal objects. A structure similar to a compass needle was the first magnetic field-triggered fuse for mines. With the development of micro-electromechanical systems (MEMS), the idea of using movement to sense magnetic fields is being reexamined, but fabricating these devices is challenging [44-52]. This is especially true if the fabrication process requires the use of different technologies that are not naturally compatible. For example, the use of HF that is often required to perform the release step needed to fabricate the MEMS structure can damage other parts of the sensor. Most of these sensors use the Lorentz force.

An example of this is a magnetometer based on detecting the motion of a miniature bar magnet [12]. The hard magnetic material used was deposited by electro-deposition. The choice of materials for the hard magnet was limited by the need to use HF in the release step, and the bar magnetic responded to the field without drawing any power. Fields as small as 200 nT have been detected optically.

A similar approach was employed by DiLella et al. [13], who also used the rotation of a MEMS structure containing a permanent magnet. In this case, the field was determined by measuring the feedback required to maintain a constant tunneling current. They achieved a resolution of 0.3 nT $/\sqrt{\mathrm{Hz}}$ at 1 Hz, but the accuracy of the sensor was limited by air pressure fluctuations.

An alternative approach uses a xylophone resonator [14], where an AC current whose frequency is adjusted to be equal to resonant frequency f_0 of a MEMS beam is sent through the length of the beam. A DC field applied perpendicular to the axis of the beam will energize the motion of the beam

at a frequency of f_0. The amplitude of the motion that can be detected optically is proportional to the field.

MEMS technology can improve magnetic sensors by minimizing the effect of 1/f noise. The concept for a device that can accomplish this (the MEMS flux concentrator [15]) is shown in Fig. 2-7. In this device, the flux concentrators composed of soft magnetic material are placed on MEMS flaps. The flux concentrators enhance the field, and decreasing the separation between the flaps increases the enhancement. The two MEMS flaps are forced to oscillate by applying an AC voltage to the electrostatic comb drives. By tuning the frequency, the normal mode in which the distance between the flaps oscillates can be excited. The resonant frequency for the MEMS structure is designed to be about 10 kHz. The oscillation of the MEMS flaps modulates the field at the position of the sensor and thus shifts the operating frequency of the sensor above the frequency where 1/f noise dominates. Depending on the type of magnetic sensor used, this shift in operating frequency should increase the sensitivity of magnetometers by one to three orders of magnitude.

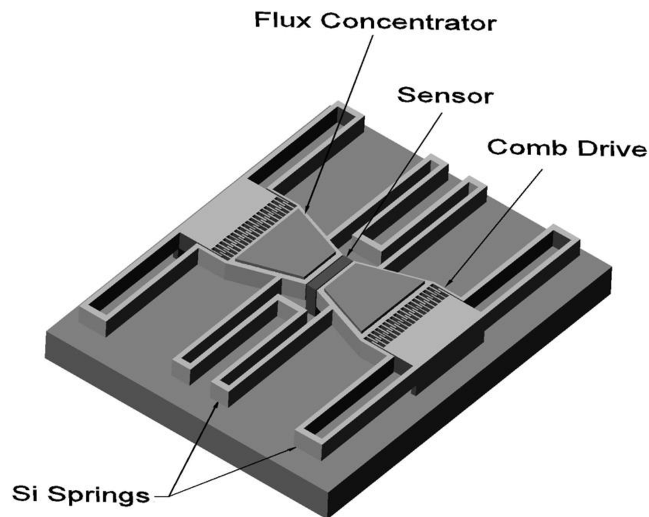

Figure 2-7 Picture showing the concept of the MEMS flux concentrator. Note that there is a space between the substrate and the flux concentrators on the MEMS flaps [15].

Tang and his colleagues [9-12], who are among only a few researchers studying magnetic micro reed switches/sensors, have proposed using nickel-based MEMS beams to fabricate a magnetic MEMS sensor/switch. In their recent work, they attempted to employ both magnetic torque and magnetic inertia to keep magnetic flux lines connected [10-12]. Their switches are a new sensing element in the millitesla range. One of the drawbacks of their research is the size of their devices, all of which are in the order of millimeters [9-12]. Figure 2-8 illustrates a sample of their devices.

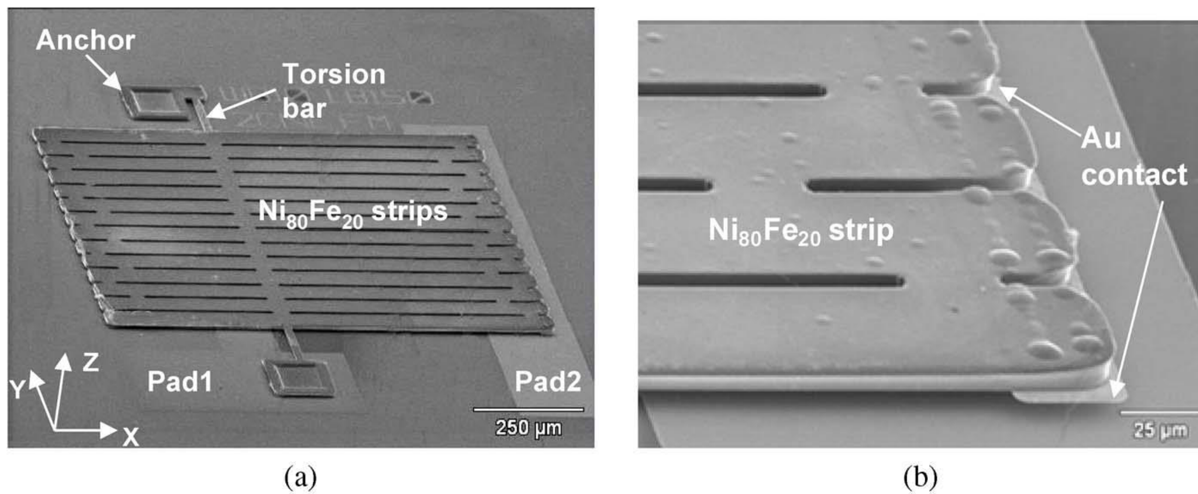

Figure 2-8 (a) SEM microphotograph of a magnetic switch, (b) zoomed-in view of the contact part [10].

In 2013, Hui and colleagues [40] developed a MEMS magnetic sensor using a MEMS multilayer resonator. The multilayer plates were a combination of a magneto-restrictive material and a piezo-electric material. The sensors could achieve a performance frequency of 200 MHz and were designed to sense magnetic field of 0 to 150 Oe.

In recent years, some groups have started to refabricate the previously reported MEMS magnetometers employing CMOS-MEMS technology [41, 42], which allows them to integrate an on-chip actuation magnetic coil to the devices. Moreover, CMOS-MEMS sensors have the advantage of using an existing foundry service, electrical routing compatibility, and monolithic integration of MEMS structures and sensing circuits. This enables them to achieve the same sensors with a better quality of fabrication.

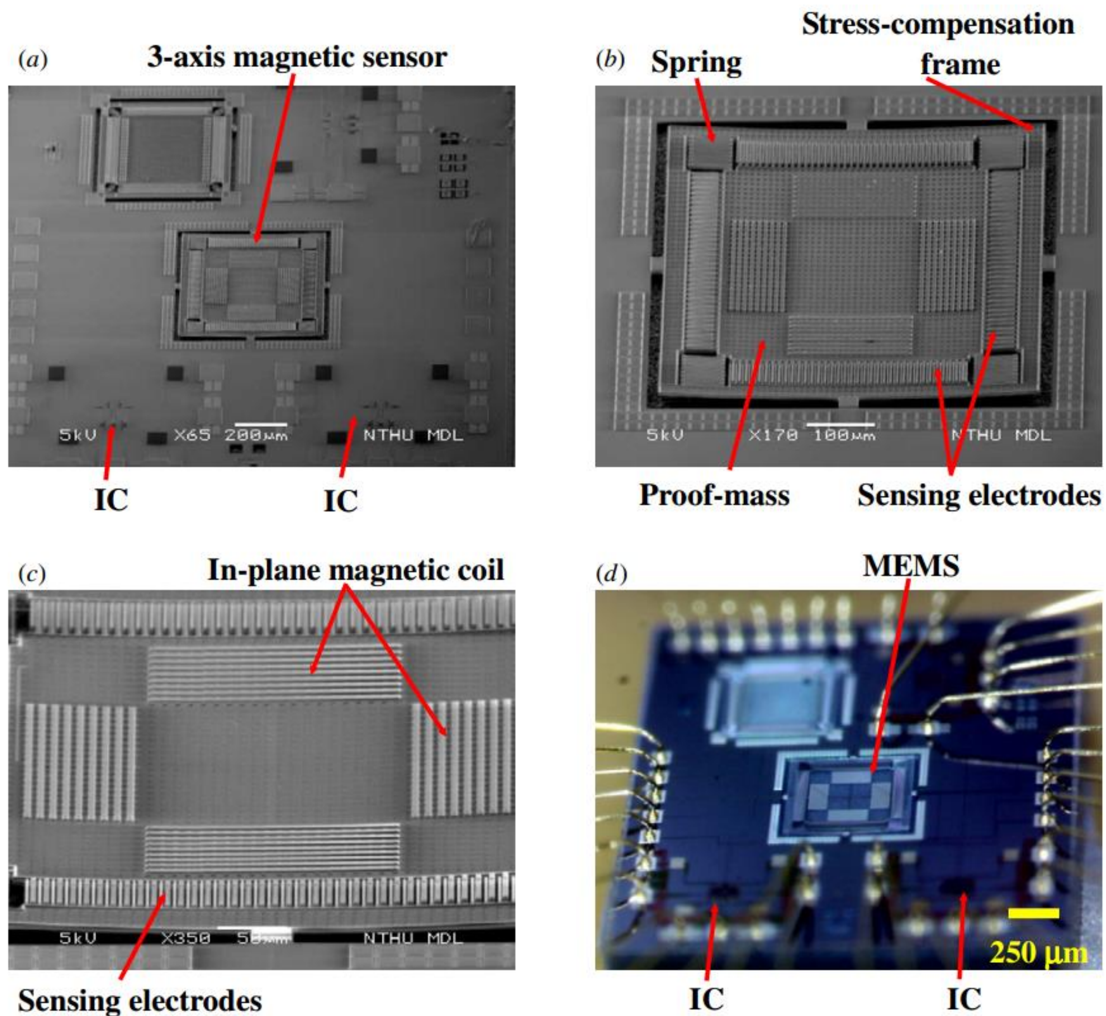

Figure 2-9 CMOS-MEMS magnetometer systems with integrated magnetic coil [41]

2.1.8 Giant Magneto-Impedance Sensors

When a soft ferromagnetic conductor is subjected to a small alternating current (AC), a large change in the AC complex impedance of the conductor can be attained when a magnetic field is applied. This is known as the giant magneto-impedance (GMI) effect [21]. The GMI effect was first observed in 1994 by Panina in her Ph.D. work [25], [34]. This was followed by experiments performed by other researchers, during which GMI was employed in wires and single thin films [25-38, 43]. Figure 2-10 shows an example of these sensors [43]. As we can see from the picture, the bulky nature of these sensors makes them unfavorable for miniature applications. Although some researchers did attempt to make multilayer GMI devices as well [33], [37], [38], the basic thrust of the GMI effect is to change

the impedance under the magnetic field. It occurs mostly in the millitesla range of the magnetic field and in frequencies of tens of MHz [30]. Since GMI changes as a function of the external DC magnetic field or applied DC/AC current, it is possible to design GMI-based sensors that can measure either magnetic fields or DC/AC currents. GMI is also sensitive to applied stress, and this provides a new opportunity for developing stress sensors. These sensors will be briefly described and evaluated below [21].

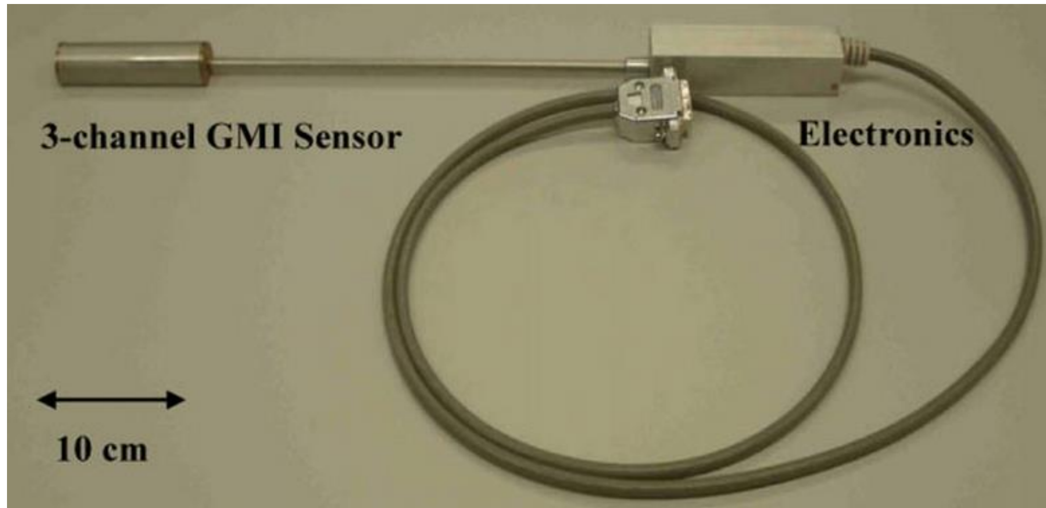

Figure 2-10 A Co-wire GMI sensor reported in [43]

A magnetic sensor based on the GMI effect (or the so-called GMI sensor) was designed and produced by Mohri et al. [34]. Continuous efforts have been devoted to improving the sensitivity of the sensor by optimizing the processing parameters and/or the design of the electrical circuit [30-38]. Detailed investigations of how the processing parameters can be controlled, as well as the influences of these parameters on the performance of a designed GMI sensor, can be found in [27] and [38]. In these sensors, the sensing elements can be amorphous wires [25-29 and 33-35], thin films [37-38], or ribbons [21]. They can be used for measuring or tracking the presence of both homogeneous and inhomogeneous magnetic fields. While GMI sensors provide numerous advantages (e.g., low power consumption, small dimension) over conventional magnetic, their high sensitivity is the most important advantage. Indeed, the resolution is even higher than that obtained from the flux gate (FG) sensor. In addition, the GMI sensor has better thermal stability compared to conventional sensors [27-35]. A general schematic of GMI sensors is shown in Figure 2-11.

In addition to GMI sensors designers, some researchers started to investigate applications of these sensors in real life. In 2014, Li[50] offered a study of surface acoustic wave (SAW) GMI sensors. Using the SAW element, they achieved a wireless GMI sensor.

Although there are many publications on GMI sensors, this field currently suffers from a lack of material characterization and FEM simulations of this phenomenon. A few publications [47-49] on simulation are attempting to solve GMI-related equations numerically for a GMI single ribbon. GMI-related equations and analytical models are discussed in detail in Chapter 4.

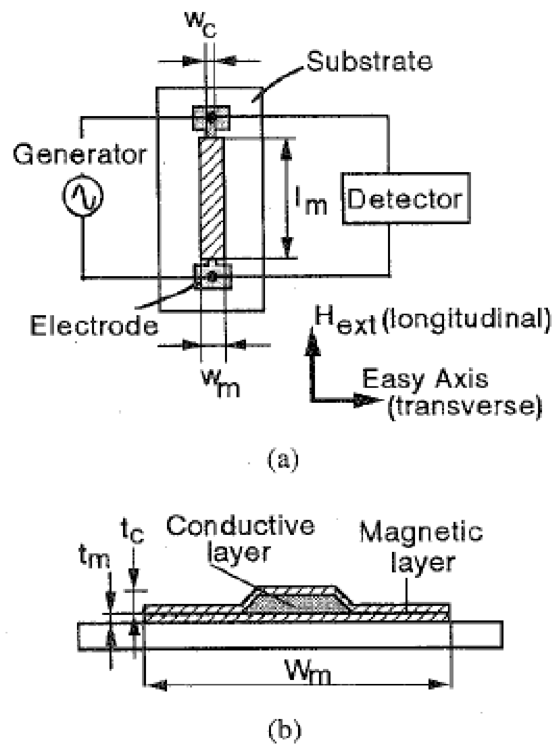

Figure 2-11 Schematic view of GMI element (a) top view (b) cross sectional view [38].

3 Chapter Three
Multilayer MEMS Reed Sensors

3.1 Introduction

For portable electronics with battery operation, a passive switch is more favorable compared to an active switch. The conventional reed switch is a typical passive switch, which includes a glass package containing two metal reeds. The metal reeds can be actuated to make a contact using an external magnetic field. When the external magnetic field is removed, a spring restores the reed to its original position. This approach is ideal for applications where conserving battery power is critical, as the device does not consume power in the off state [8-10].

For portable electronics applications such as cellular phones, hearing aids and laptops, further miniaturization, higher shock resistance, and better integration of switches are desirable. The micro-electromechanical (MEMS) magnetic switch can meet these requirements. It mimics the operations of the reed switch, but is fabricated using microfabrication technology. Therefore, it can drastically reduce the size of the device, lower the fabrication cost, and improve shock resistance [2-3].

In this chapter, a preliminary design for a nickel-based magnetic reed switch is introduced. The design is fabricated in several dimensions and shapes, ranging in length from 100 to 500 microns and in width from 20 to 80 microns.

Unfortunately, the fabricated micro switches with nickel beams failed during testing. There are two main reasons for this failure. First, as nickel is sensitive to EKC solution, it was not possible to wet release the nickel structures. All the attempts to wet release it failed, as the nickel was etched away before the sacrificial layer (polyamide). Second, the dry release of the nickel beams was adversely affected by the residual polyamide under the beams, which prevented switch electrical contact. Even the mechanically actuated switches failed to show contact resistance.

In order to overcome these issues, we suggested and designed a new fabrication process consisting of a tri-layer of Au-Ni-Au beams. The new beams allowed us to wet release the structure and achieve successful MEMS switches. Using Electro-less plating (ELP) for both nickel and gold layers resulted in only 4 masks for this 7-layer MEMS structure. The low number of masking and lithography steps effectively improves the microfabrication quality.

A review of governing equation in magnetostatic MEMS is first conducted, after which the required FEM equations are presented and solved using the finite element software, COMSOL 4.2. By utilizing COMSOL's built-in modules for magnetostatic physics, the nickel switch is fully simulated

and the resulting magnetic force is determined for numerous system configurations. Next, mask designing steps are reported and a quick review of fabrication process is done, including brief descriptions of each step of the fabrication. Then, the challenges of these switch/sensors are discussed and the tri-layer MEMS Reed sensors are introduced in the same order as the preceding. Finally, an experimental setup for measurement is presented, along with the results and conclusion. Any perceived errors and problems are listed here, as along with further improvements and suggestions to overcome the challenges.

3.1.1 Theory

A physical-level analysis of magnetostatic MEMS requires a self-consistent solution of the coupled mechanical and magnetic equations.. The basic reed switch consists of two ferromagnetic nickel-iron beams encapsulated in glass. The two reeds act as magnetic flux conductors when exposed to an external magnetic field from either a permanent magnet or an electromagnetic coil. Poles of opposite polarity are created at the contact gap, with the contacts closing when the magnetic force exceeds the spring force of the reeds. The contacts open when the external magnetic field is reduced so that the magnetic attractive force between the reeds is less than the restoring spring force of the reeds.

The basic reed switch is a Single Pole Single Throw Normally Open (SPST-NO) switch. By including an additional nonmagnetic contact that is electrically closed with no magnetic field present, a Single Pole Double Throw (SPDT) switch (also known as a changeover switch) can be made. This is a break-before-make switch, in that the closed contact opens before the open contact closes.

Generally, in MEMS magnetic reed switches, the goal is to make contact between the beams by the force generated to maintain magnetic flux continuity. The magnetic flux is confined to the permanent magnet and switch beams due to their high magnetic permeability. As the magnetic flux and magnetic field require continuity, a force will be generated to lower the gap between the two beams and enable contact.

The magnetic field gives rise to a magnetostatic body force which deforms the cantilever beam from its initial position. When the beam deforms, the magnetic field changes, and the resultant magnetostatic force and beam deformations also change. Figure 3-1(b) shows the deformation of the cantilever at any given point in time and the forces acting on it. The magnetostatic force causes the

beams to deform to a state where they are balanced by internal stiffness; at that time, the inertial forces are instantaneous (see Figure 3-1(b)).

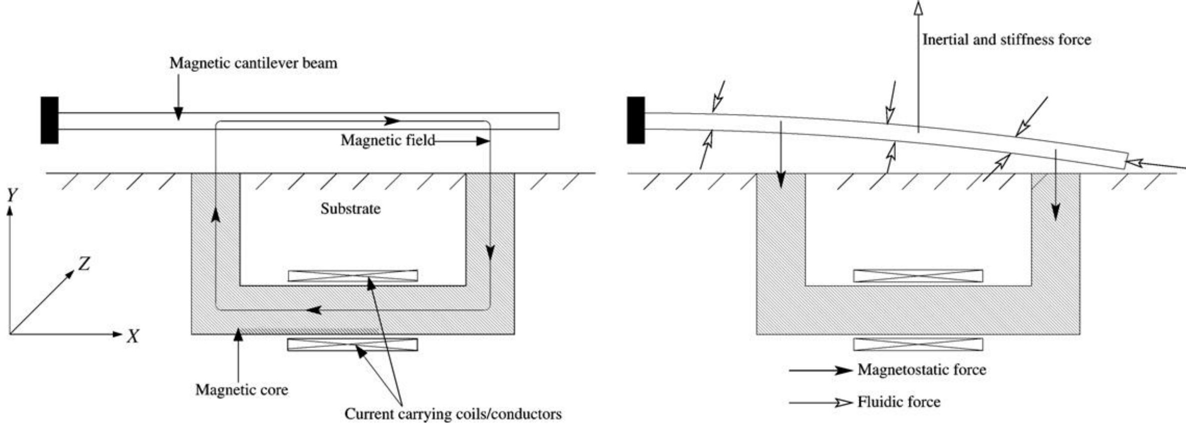

Figure 3-1 Schematic view of undeformed magnetic switch and a deformed one [8].

The mechanical restoring force arises due to the stiffness of the structure and depends on the displacement of the beam/structure at that instant in time, whereas the inertial force depends on beam acceleration. The governing equations for each of the energy domains and their Lagrangian formulations are discussed below. For details on the theory deployed in this thesis, please refer to [8] and Appendix A.

Based on this approach, magnetostatic governing equations are derived from Maxwell's equations. Equations 1 and 2 show the derived magnetostatic equations.

$$\boldsymbol{B} = \begin{Bmatrix} B_X \\ B_Y \end{Bmatrix} = \boldsymbol{F}^{-\boldsymbol{T}} \begin{Bmatrix} \frac{\partial A_z}{\partial Y} \\ -\frac{\partial A_z}{\partial X} \end{Bmatrix} = \begin{bmatrix} 1 + \frac{\partial u}{\partial X} & \frac{\partial u}{\partial Y} \\ \frac{\partial v}{\partial X} & \mathbf{1} + \frac{\partial v}{\partial Y} \end{bmatrix}^{-\boldsymbol{T}} \begin{Bmatrix} \frac{\partial A_z}{\partial Y} \\ -\frac{\partial A_z}{\partial X} \end{Bmatrix} \tag{1}$$

$$\boldsymbol{f_{mag}} = \boldsymbol{M}.\boldsymbol{\nabla_x B} = \boldsymbol{M}.\boldsymbol{F}^{-\boldsymbol{T}}\boldsymbol{\nabla_X B} \tag{2}$$

where A is the magnetic field's potential vector, F is the deformation gradient tensor, and M is the magnetization vector. Equation 2 represents the magnetostatic body force acting on the microstructure in the deformed configuration.

In a mechanical resorting force, one can calculate the spring constant of the beams based on mechanical strength equations and beam dimensions. There are different equations for different kinds of beams. For instance, for a simple cantilever beam, the spring constant is:

$$K = \frac{3EI}{L^3} \quad (3)$$

where E is the Young's modulus of the beam material, L is beam length, and I is the moment of inertia of the corresponding beam. A cantilever beam can be calculated by (31):

$$I = \frac{wt^3}{12} \quad (4)$$

where w is beam width and t is beam thickness. After calculating the spring constant of the beam, the mechanical restoring force can be calculated using Hooks law:

$$F_{mech} = ky \quad (5)$$

Once the magnetic body force f_{mag} is sufficiently high to overcome the F_{mech} value in the y=gap, the switch will be actuated. It should be noted that more complicated beam models can be employed to calculate mechanical forces, but response errors are negligible between various models. It is also important to note that the spring constant equation will change by varying the beam and support shapes. The above-mentioned equations are governing equations for magnetic reed switches/sensors, which will be solved by finite element software. We have employed COMSOL multiphysics to solve these equations and simulate the design. These results are discussed in the next sections.

3.2 Nickel-based Magnetic MEMS Reed Sensors

A magnetic MEMS reed switch/sensor is designed and fabricated on silicon. The reeds are multilayer nickel beams with dimensions of 300*60 microns. Several types of switches with different configurations have been designed and successfully fabricated, and a FEM COMSOL 4.2 simulation is implemented to simulate the switch/sensor. Based on the simulation results, a magnetic body force of 3.75μN is achieved at a 10 mT magnetic field. This force exceeds what is required to actuate the switch. The switches have been tested in the lab under a constant magnetic field.

3.2.1 Modeling and FEM Simulation

In order to conduct a simulation of the magnetic reed switches/sensors, COMSOL Multiphysics 4.2a is employed. Using COMSOL's built-in physics (AC/DC module and structural mechanics), all of

the above equations have been solved. As well, a beneficial new feature of the AC/DC module is magnetostatic force calculation, which makes simulation more straightforward for our case study.

As mentioned in the Introduction, we chose nickel as our beam material. Nickel's permeability is 400, meaning it is a good ferromagnetic material that is less prone to oxidization than iron. Also, nickel is conductive, so the beam itself can make electrical contact.

Because the MEMS switches are fabricated on wafers, the bottom electrode is fixed to the substrate (first-level layer) and cannot have any movement and displacement. Therefore, the only moving part in our design is the upper beam. Using the simulation results, and based on fabrication restrictions, the bottom electrode thickness is chosen to be 3 microns. The resultant thickness of the upper beam is then investigated for 3 microns and 1 micron. Based on the results in step 1, the micron thickness beam has more magnetic body force and also has less mechanical restoring force due to being thinner. The gap in our design is assumed to be 1 micron, but larger gaps have also been studied.

The beam lengths in the simulation portion of our work are assumed to be 100 microns, with a 50-micron overlapping length between the two beams. The gap is assumed to be 1 micron. A permanent magnet with different magnetization vectors has been placed in various positions and distances with respect to the switch. Finally, the magnetic body force calculated in the AC/DC module is coupled to a structural mechanic module, as the load and movement of the beam is investigated.

A brief review of simulation steps, along with the results of each step, is discussed and shown below:

A) Choosing the physics

As our first step, a 2D analysis system was chosen in COMSOL, after which a model navigator window, the AC/DC module, was selected. In the AC/DC module, we used magnetostatic fields with no current. Later on, we will add Plane strain analysis from a structural mechanics module. By selecting stationary analysis as our solving method, we proceed to the design portion in a GUI window.

B) Drawing system in GUI

The second step is drawing the model in the model builder wizard. Objects of the system are sketched as follows:

A large square of 2*2 mm is sketched and its boundary restricted to be magnetically insulated. This large square is assumed to be our working environment with the whole system within it. The material of this object is defined to be air. From henceforth in this report, we will refer to it as the ‘environment’.

A 20*25 μm rectangle is drawn as a permanent magnet within the environment, with a corner (130μm, 50μm) in a Cartesian plane. From this point onward, we will refer to it as a ‘permanent magnet’.

The upper beam is sketched with a 1-micron thickness, a 100-micron length, and a corner of (0,0). The bottom electrode is then sketched with a 3-micron thickness, 100 micron-length, and a corner of (-4μm, 48μm).

The gap in our design is assumed to be 1 micron, but larger gaps have been also studied. Figure 3- 2 shows the modeled structure in GUI.

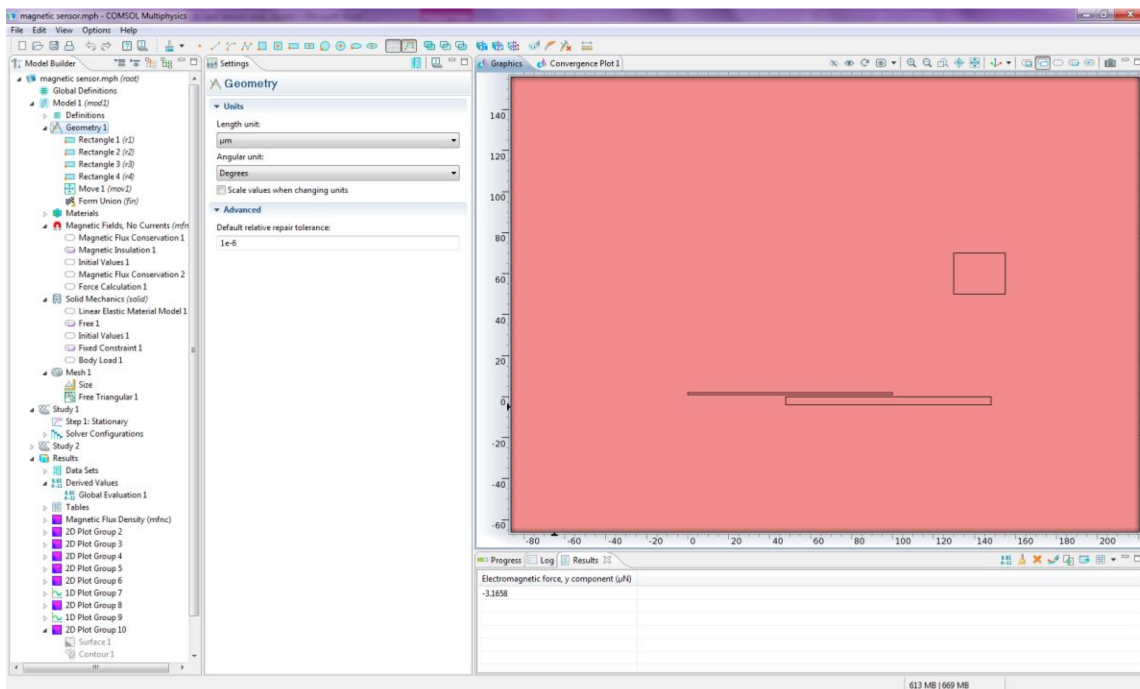

Figure 3-2 Modeled magnetic MEMS switch in COMSOL 4.2 GUI.

C) Subdomain settings

In our subdomain settings, the material properties of each object have been defined and their properties regarding magnetic calculation are clarified as follows.

- Environment is defined as air, with $\mu_r = 1$.
- A permanent magnet is assumed to be magnetized iron with $\mu_r = 4000$. The magnetization vector of a magnet is assumed to be (20000,0) A/m. Other directions and values of magnetization have also been studied.
- Two beams are defined as nickel with $\mu_r = 400$. The Young's modulus of nickel is defined as 180 GPa.

In the environment and two beams, the magnetic field is calculated as $B = \mu_0 \mu_r H$. In the permanent magnet, the magnetized vector is defined by $B = \mu_0 (M + H)$.

D) Boundary settings

All boundaries are assumed to have magnetic continuity except for environment boundaries, which are defined as magnetically insulated.

For mechanical boundaries, a bottom electrode and permanent magnet are fixed in place to preclude any movement of these two objects. The upper beam is fixed at one side as x=0, and the other boundaries are defined as being free to move. The body force generated by the magnetic flux is assumed to apply to the tip of the upper beam.

E) Mesh settings

As we do not have any preferred shape of meshing, we chose the free triangle meshing method. However, due to the small gap and small feature size of beams with respect to the rest of the objects, the meshing is refined for these areas. Thus, we have an increased number of elements in critical parts to obtain more accurate answers from our simulation.

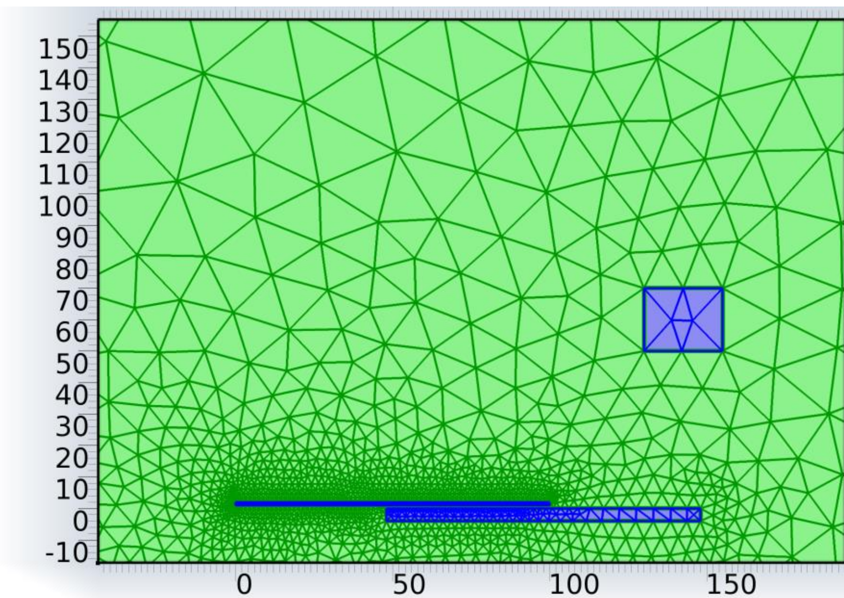

Figure 3-3 Meshing of modeled magnetic MEMS switch.

A) Magnetic force calculation

A recently added feature to COMSOL 4.2a is the magnetostatic force calculation option. This feature will solve the mentioned equations in the theory section for the system and calculate the magnetic body force for each of the desired objects. In our case, an upper beam is selected to ascertain the magnetic body force on it. Note that this body force is a vector, so its sign and components will determine its direction.

In our simulation, we achieve magnetic forces as high as -3 μN at 10mT magnetic field between the two. In our case, using the given dimensions of the upper beam, we need about 0.3 μN of magnetic force to overcome the mechanical restoring force. Thus, the generated body force is sufficiently far to actuate the system.

Case study a)

M= (0, 20000)

Permanent magnet corner= (130, 50) microns

The simulated plot is shown below. Here we can see the magnetic flux density and the contour plot of the magnetic flux in Figures 3-5 and 3-6, respectively.

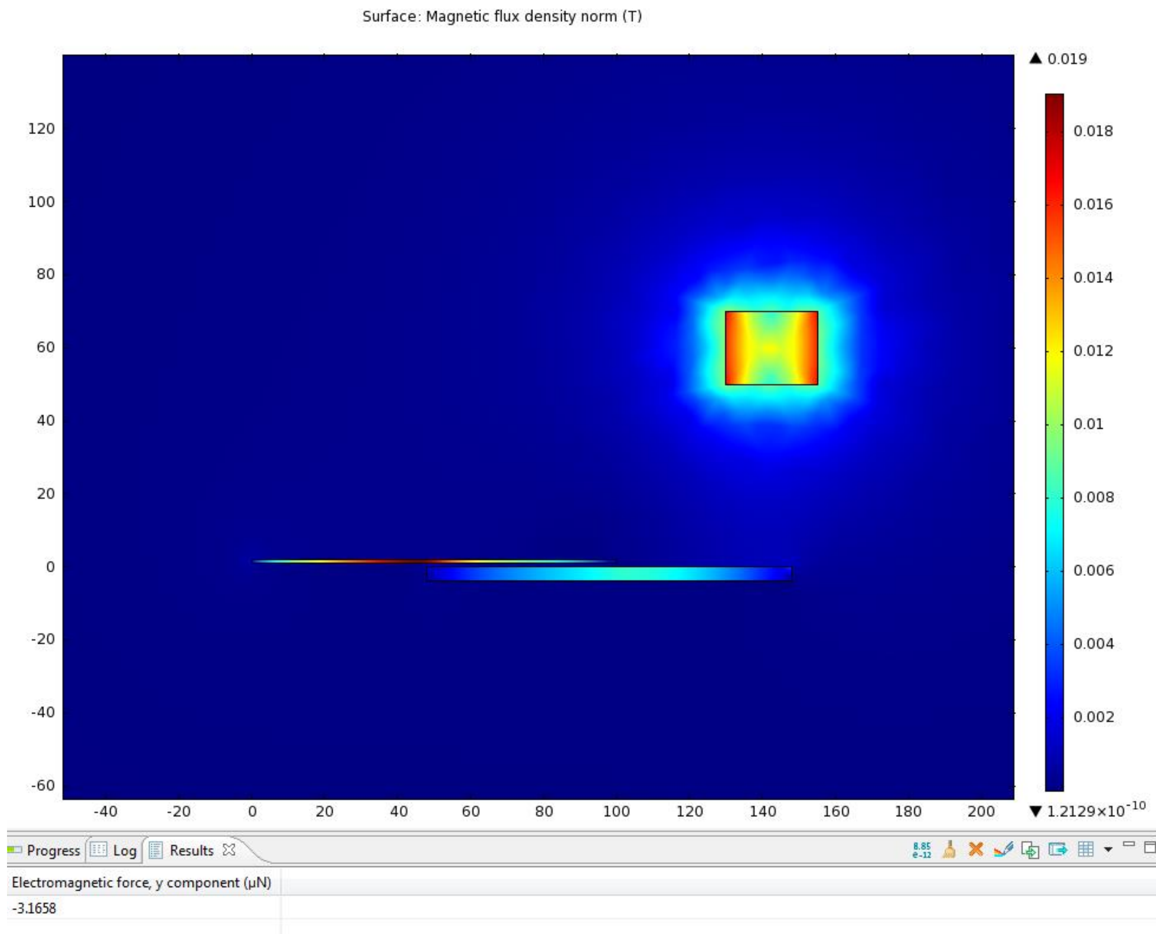

Figure 3-4 Shows the magnetic flux density in Tesla for case a).

As is clear in Figure 3-6, the maximum flux in between and around the magnetic switch is 0.012 T, which is the actuation needed field with this configuration. Moreover, the achieved force here is -3.2 μN, which far exceeds the required force for switch actuation. The shape of magnetic flux contours are shown in Figure 3-5.

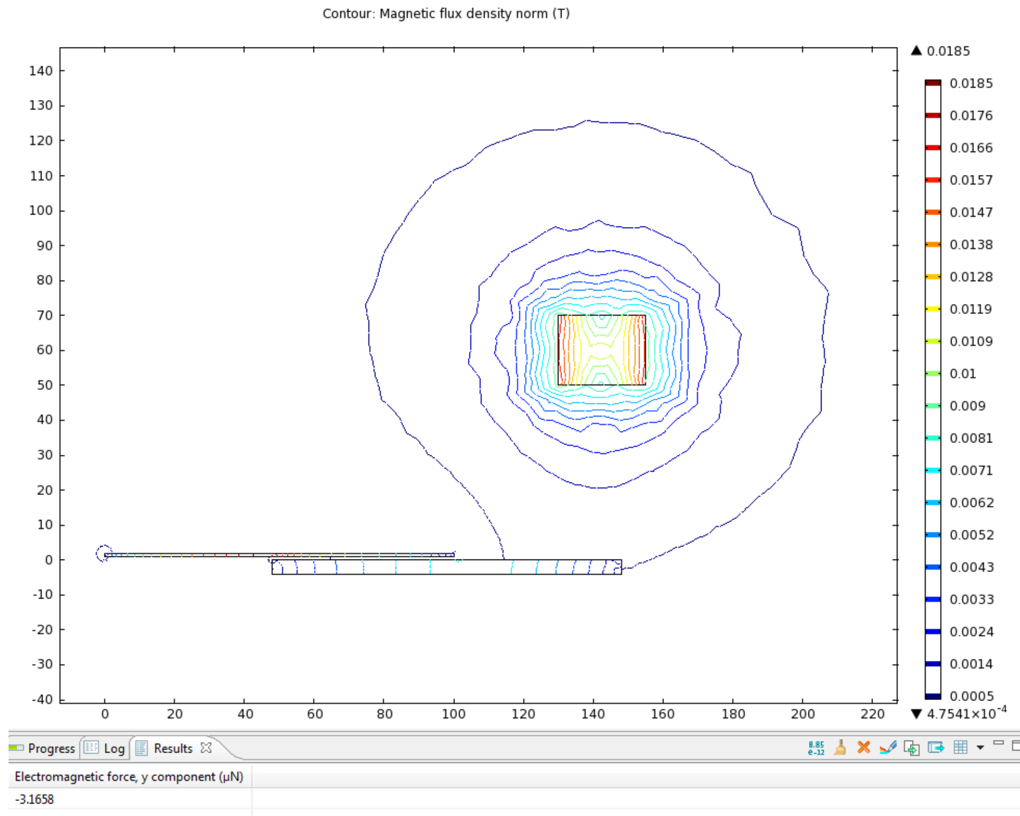

Figure 3-5 Shows magnetic flux density contours for magnetic switches.

As can be seen in the above figure, the magnetic field lines are trying to connect to each other and maintain continuity. This is the reason for the force generation, which will make the flux continuity easier. Figure 3-6 shows the magnetic flux streamline between two beams to better clarify this phenomenon.

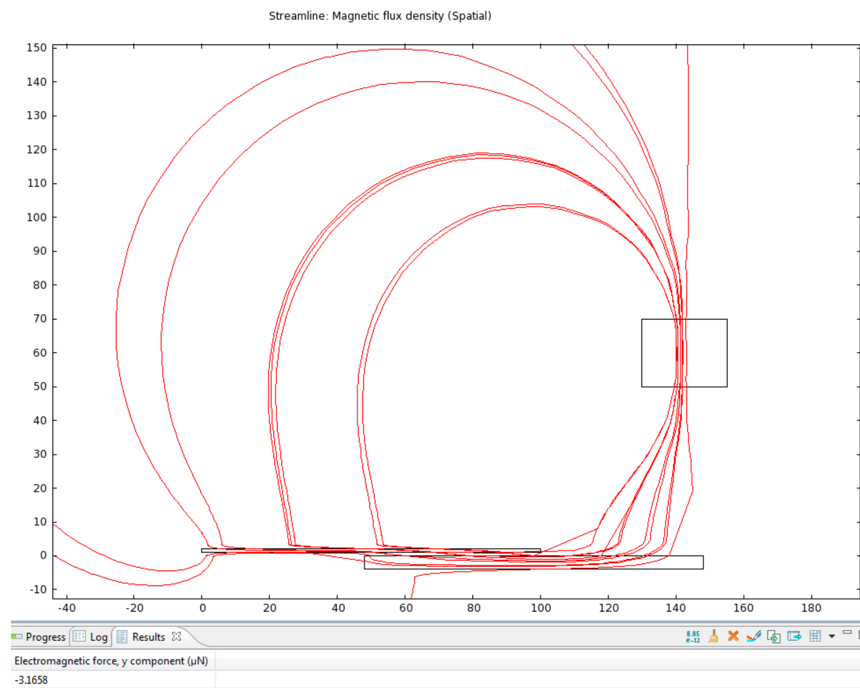

Figure 3-6 Magnetic flux density streamlines between the beams for case a).

Figure 3-7 shows the position of the system in the environment.

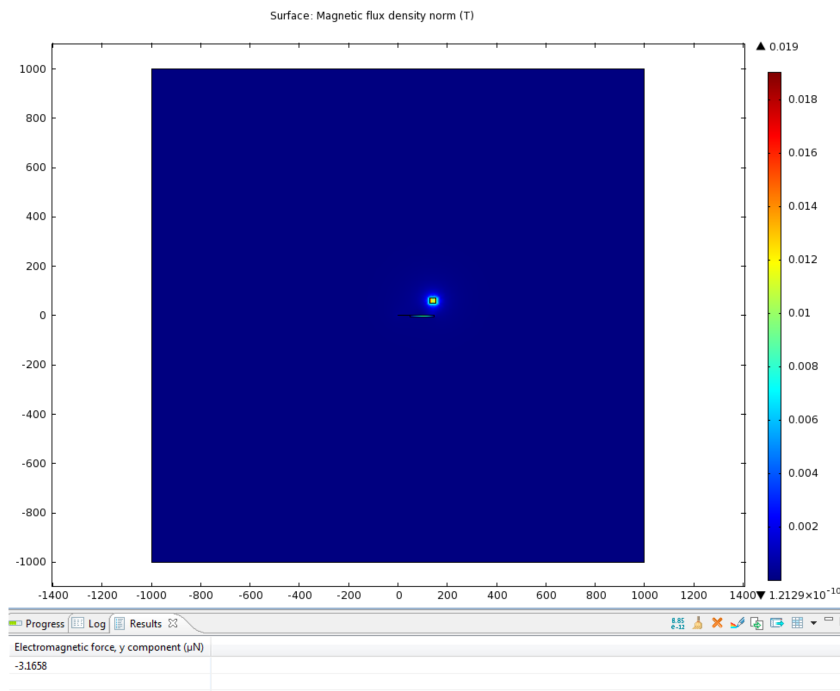

Figure 3-7 Whole magnetic model of the switches in the environment.

Case study b)

M=(20000,0)

Permanent magnet corner=(100,50) microns

In case b), a simulation has again been done. The maximum force was -3.75μN at 10mT. The resultant plots are shown in Figures 3-8 to 3-10.

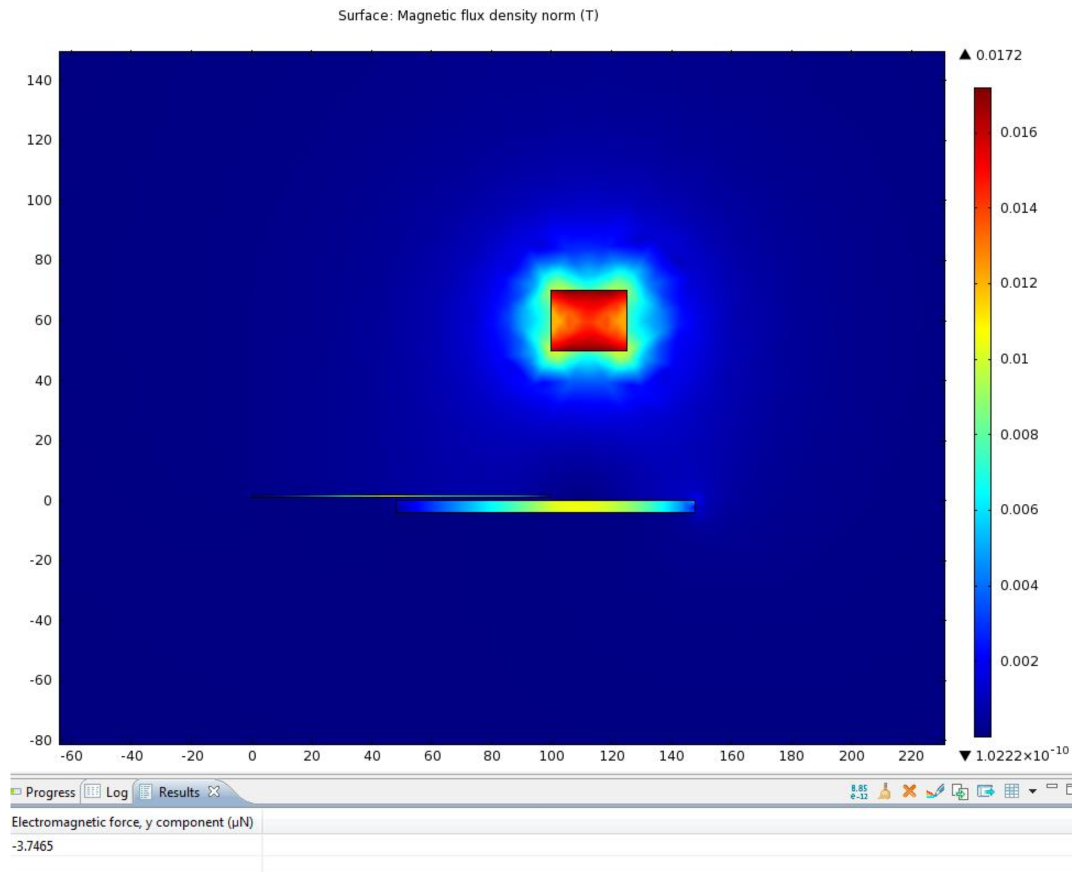

Figure 3-8 Shows the magnetic flux density in Tesla for case b).

As is clear in Figure 3-8, the maximum flux in between and around the magnetic switch is 0.008 T, which is the actuation required for this configuration. Furthermore, the achieved force here is -3.75 μN, which is significantly more than is needed for switch actuation. The shape of the magnetic flux contours are shown in Figure 3-9.

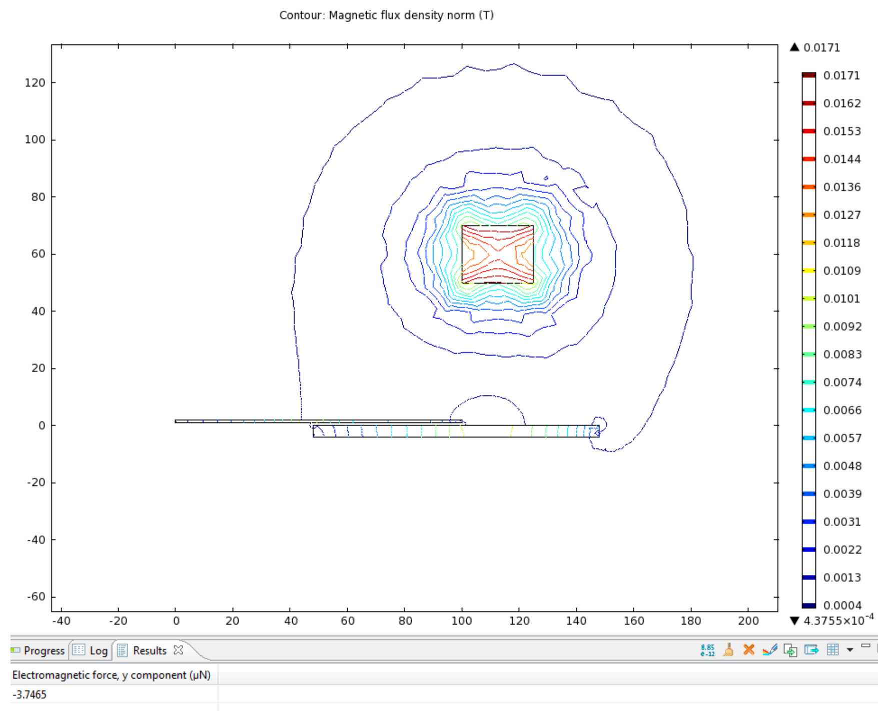

Figure 3-9 Magnetic flux density contours for case b).

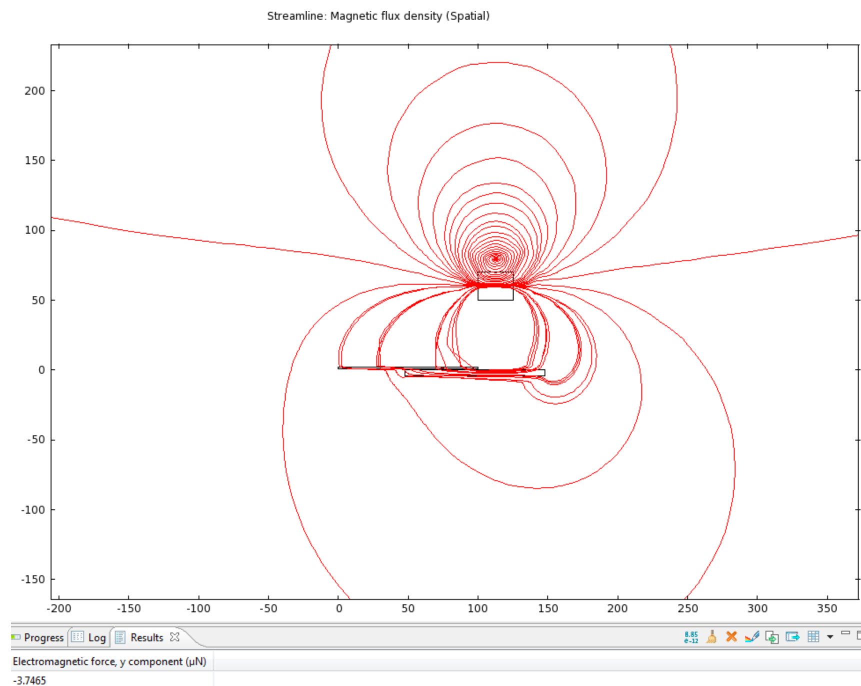

Figure 3-10 Magnetic flux density streamlines between the beams for case b).

In the future, research should focus on investigating the working positions of the permanent magnet around the switches in order to ascertain the graph of actuation position for the switches.

Assuming that we have this body force as the load in the structural mechanic module, we can see the actuation of the switch, as below.

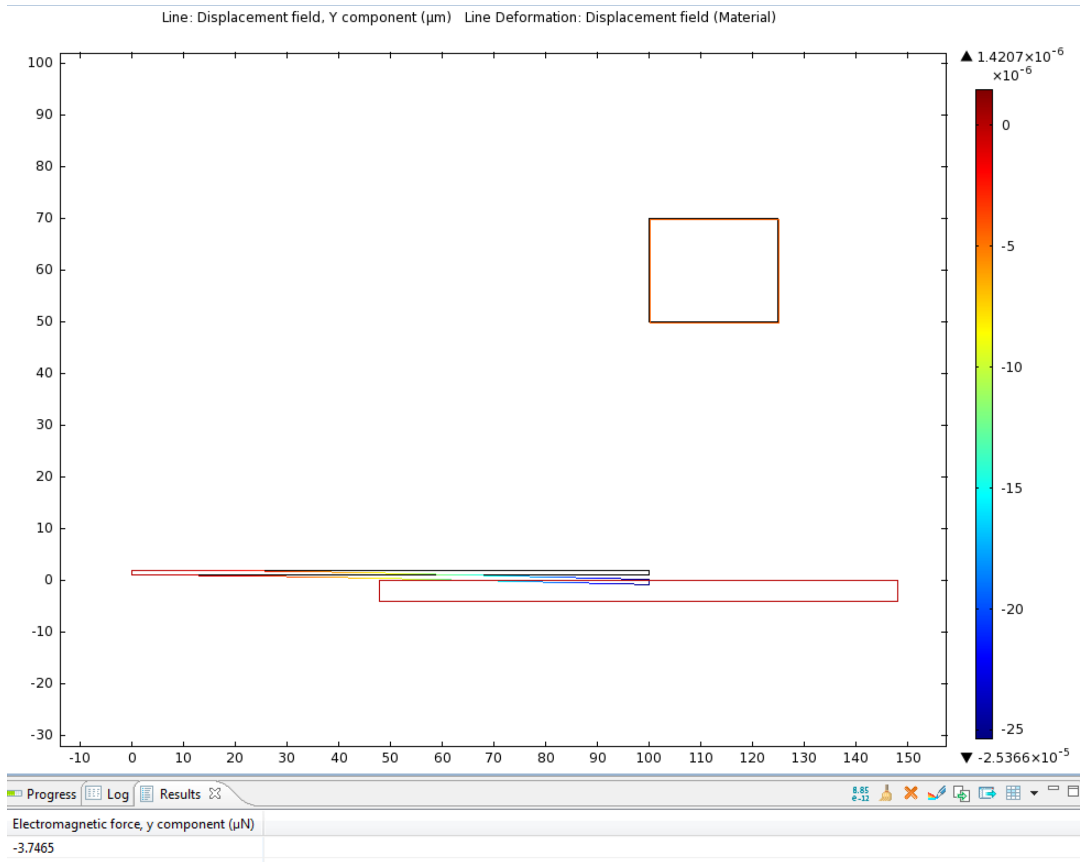

Figure 3-11 Actuation of switch at 10 mT.

As can be seen in the figure's legend, the displacement is expected to be much higher than a 1-micron gap. The upper beam will make contact with the lower one and will not go any further. Hence, the plot has been rescaled to show a correct answer.

3.2.2 Design and Mask-Making

The thickness of the beams is determined according to simulation results. A minimum length of 100 μm has been shown to work well within the designated conditions. Increasing the length will reduce the spring constant, making actuation of the devices easier. In the design step, several types of switches/sensors have been developed, each with three different lengths (500, 400 and 300) μm and

three different widths (40, 60 and 80) µm. Excluding the size differences, the designs can be categorized into five types:

- Switches with simple cantilever beam and simple fixed supports (type 1).
- Switches with minder hinge cantilevers; the support has a minder shape with two connection widths of 15 microns each. Using minder shape supports greatly reduces the spring constant of the beam, which makes actuation easier and less forceful, thus lowering the magnetic field (type 2).
- Switches with simple cantilever beam and simple fixed supports, with a 20-micron width but a wider tip of 60 microns (type 3).
- Two-way arrays of switches with widths of 60 microns, designed in all three lengths. Two arrays are perpendicular to each other and are of equal length. This design will help in sensing the direction of the magnetic field (type 4).
- Four-way arrays of switches. This is a multi-output switch with 4 outputs of various lengths. It can be used to actuate systems that require different amounts of sensitivity to magnetic fields (type 5).

Each layer of the four-layer mask is described below.

- Layer 1 is a light field mask for patterning the bottom electrodes and conductive pads for the test. This layer will be masked with positive photoresist.
- Layer 2 is a light field mask for patterning the anchor. It will be patterned with negative photoresist.
- Layer 3 is a dark field mask for dimples. It is patterned with positive photoresist.
- Layer 4 is also dark field, but it is for patterning upper beams using negative photoresist.

Table 3-1 Lithography mask layers

Mask levels	Field Type	Comments	Photoresist
Mask #1	Light	patterning Au	Positive
Mask #2	Light	patterning PI	negative
Mask #3	Dark	patterning PI	Positive
Mask #4	Dark	patterning Au	negative

Table 3-2 Layer Names, Thicknesses, and Mask Levels

Material	Thickness (µm)	Mask level	Layer description	Comments
Oxide	0.5	-	passivation	insulating layer
Ni	3	1	lower beam	200nm Cr/Au and 3 microns Ni
Polyamide	2	2 and 3	sacrificial layer	2µm Anchor and 1µm Dimple Openings
Ni	1	4	upper beam	150nm Au and 1 micron Ni

Figure 3-12 shows the final 4-layer mask in a single view (note: small features may not be visible). The design rules, which include all the physical limitations and fabrication process limitations that have been considered in the mask design process, are discussed in detail in Appendix B.

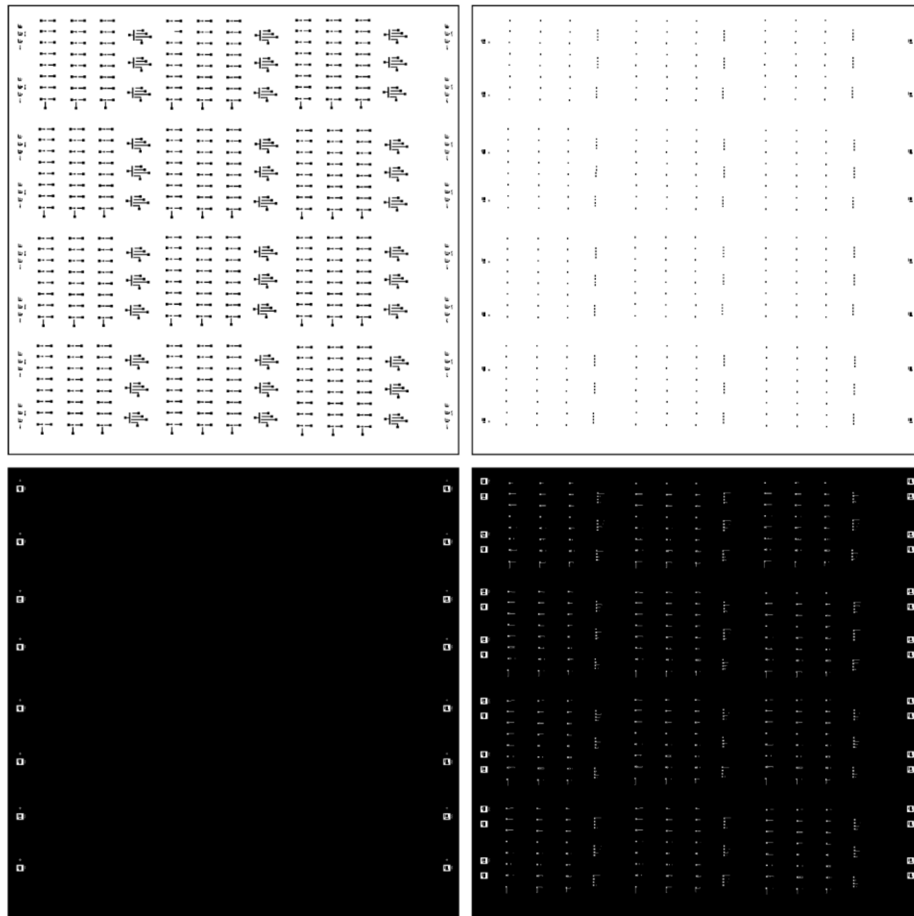

Figure 3-12 Final mask printed on glass.

3.2.3 Fabrication Process

The fabrication is carried out on four 4-inch silicon wafers. Following the RCA cleaning of the wafer, a 0.5 micron of PECVD silicon oxide is deposited on three of the wafers, and a 0.5-micron of PECVD silicon nitride is deposited on the last one. This dielectric deposition has been done to ensure that the substrate is fully insulated.

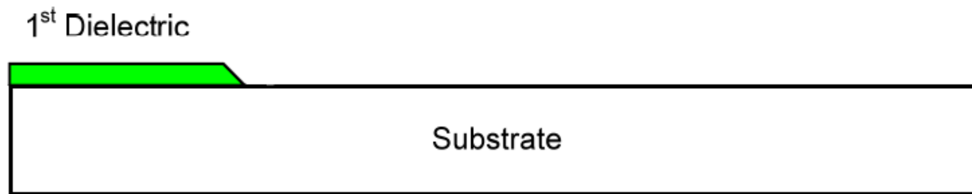

Figure 3-13 The passivation dielectric layer above silicon substrate.

Next, an evaporated 400Å chromium /100nm gold bilayer is deposited as a seed layer for electroless-plating of Ni. A positive PR(AZ3330) is spin-coated on top of this layer, and the first mask layer is patterned on it. The patterned seed layer is then etched using gold and Cr etchants. After 50 sec of gold etchant and 30 sec of Cr etchant, the gold seed layer is fully patterned. The chromium is applied as an adhesion layer for the gold.

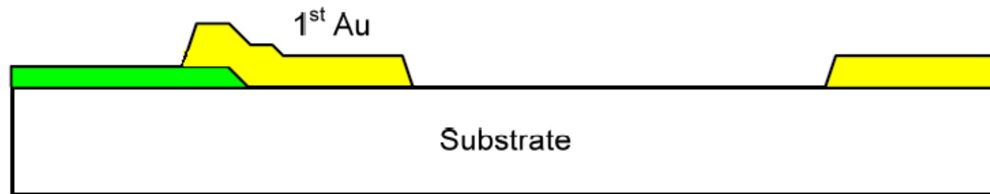

Figure 3-14 Cr/Gold seed layer after patterning.

In the next step, an electroless solution of Ni (Caswell ink) is prepared and heated to 90° C. The wafers are then placed into the solution for nine minutes. The rate of deposition was previously tested and verified to be 0.33µm/min. Note that the wafers are first put into oxygen plasma for about 1 min before being put into the EL solution. The reason for doing this is to create some free electrons in order to initiate the electroless plating; otherwise, the plating will not be initiated.

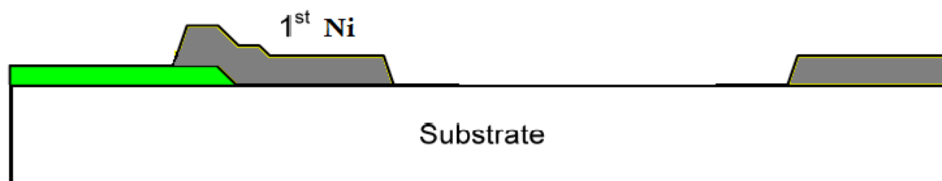

Figure 3-15 Bottom electrode fabricated on top of the substrate.

Spin-coated Polyimide is used as the sacrificial layer for this process. It is initially coated to a thickness of 1.5µm, cured in an oven, and then subjected to 75nm of Au sputtering. Next, the Au is patterned by Mask3 (anchor mask) in order to make a hard mask for the PI etch. After that, patterned

gold is used as a mask for PI, and the anchor is etched using the EKC wet etch of PI to fully clear the anchor holes.

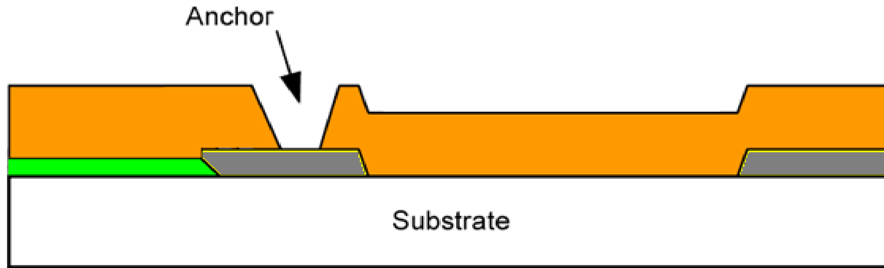

Figure 3-16 Patterned anchor (the gold layer on top of PI is not shown to prevent misunderstanding).

Following the patterning procedure, AZ330 is again used to pattern the anchor dimple mask by removing the gold layer in the gold etchant. The wafers are then placed in RIE to remove dimples with 1-micron thickness. After patterning dimples on the PI, the covering gold layer is removed using a gold etchant. The resultant state is shown in Figure 3-17.

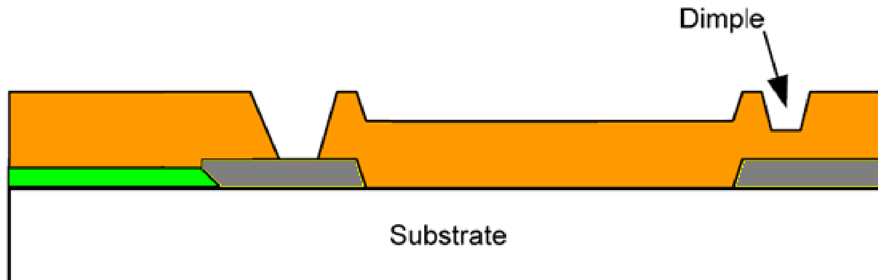

Figure 3-17 Wafer after patterning anchor and dimples on PI.

Afterward, the wafers are sputtered in 50 nm of gold and the final layer is patterned on the gold using NLOF2550. Then the same process that was done for the first EL plating is repeated in order to create upper nickel beams. The final structure, prior to release, is shown in Figure 3-18.

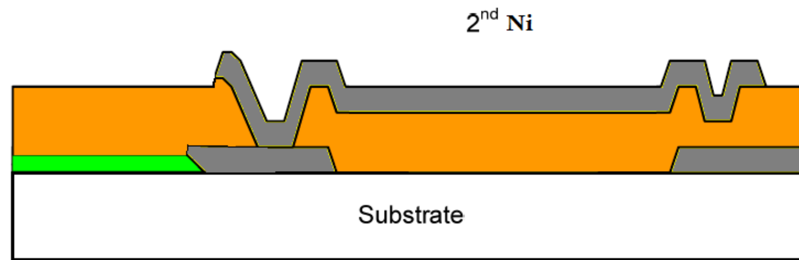

Figure 3-18 Final structure before release.

The wafers are diced into individual dies to do the release. In order to release the devices, a first attempt was made using EKC wet release. Although the speed of the wet release was good and it had less residual stress than the other methods, EKC attacks EL nickel, and almost all of the Ni was etched by the release time. In our next attempt, we used RIE dry release. This method works well, but it is very time-consuming and takes days for RIE release, which makes it unsuitable for our purposes.

The final suggested way was using an oven and annealing the devices at 450 ^{o}C in the air. It was hoped that by increasing the temperature, PI would chemically react with oxygen in the air and thus be removed from the substrate. The devices were successfully released by applying this method, but the high temperature release led to residual stress, which caused some beam deformations.

The optical images of fabricated magnetic switches are shown in Figures 3-19 to 3-24.

Figure 3-19 Optical image of switch type 1 – simple cantilever.

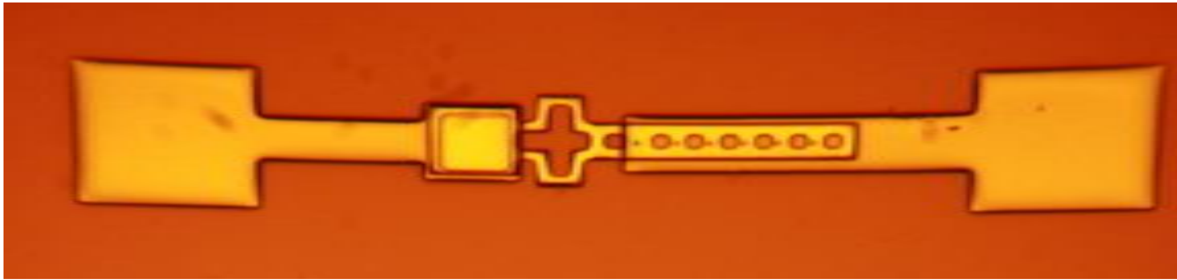

Figure 3-20 Optical image of switch type 2 – minder hinge switches.

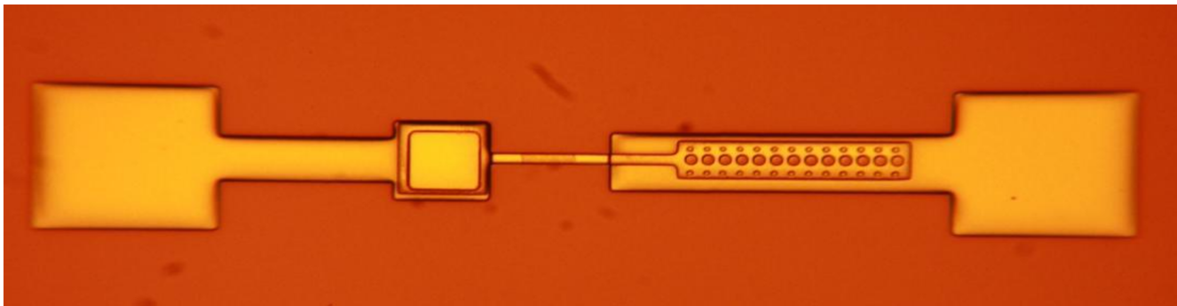

Figure 3-21 Optical image of switch type 3 – narrow cantilever with wider tips.

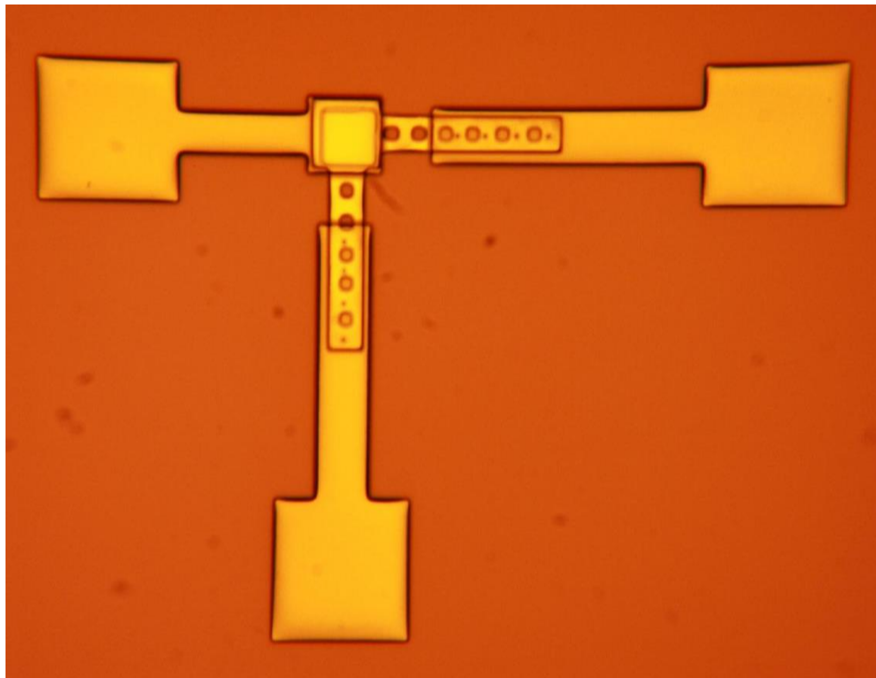

Figure 3-22 Optical image of switch type 4 – two-array switches.

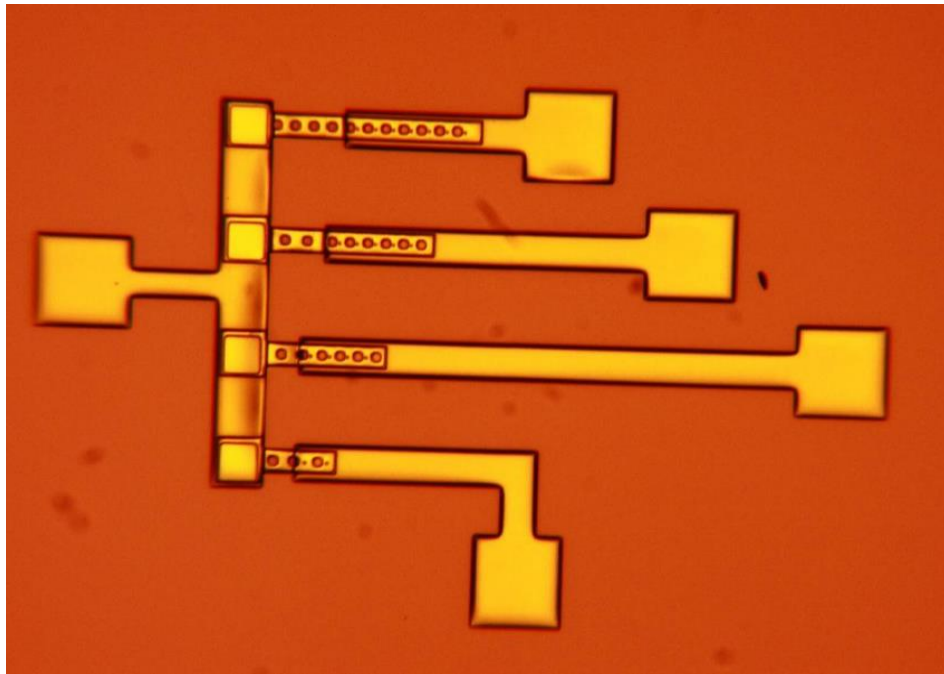

Figure 3-23 Optical image of switch type 4 – four-arrays switches.

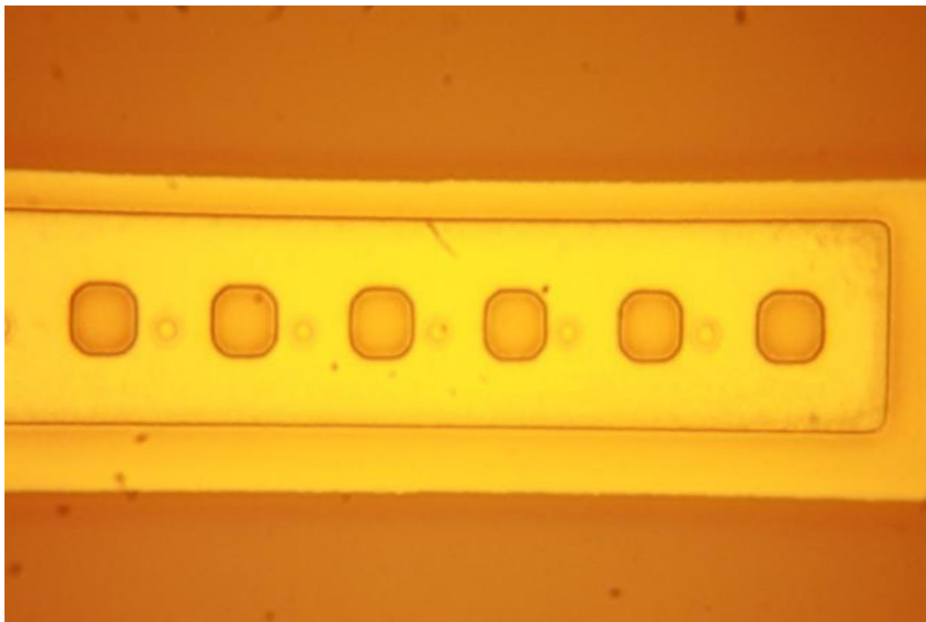

Figure 3-24 Optical image of tip of one cantilever showing the position of the upper beam with respect to the lower one; dimples and release holes are shown here.

Figures 3-25 to 3-29 illustrate some SEM images of fabricated devices. The quality of the fabrication is clear in these figures.

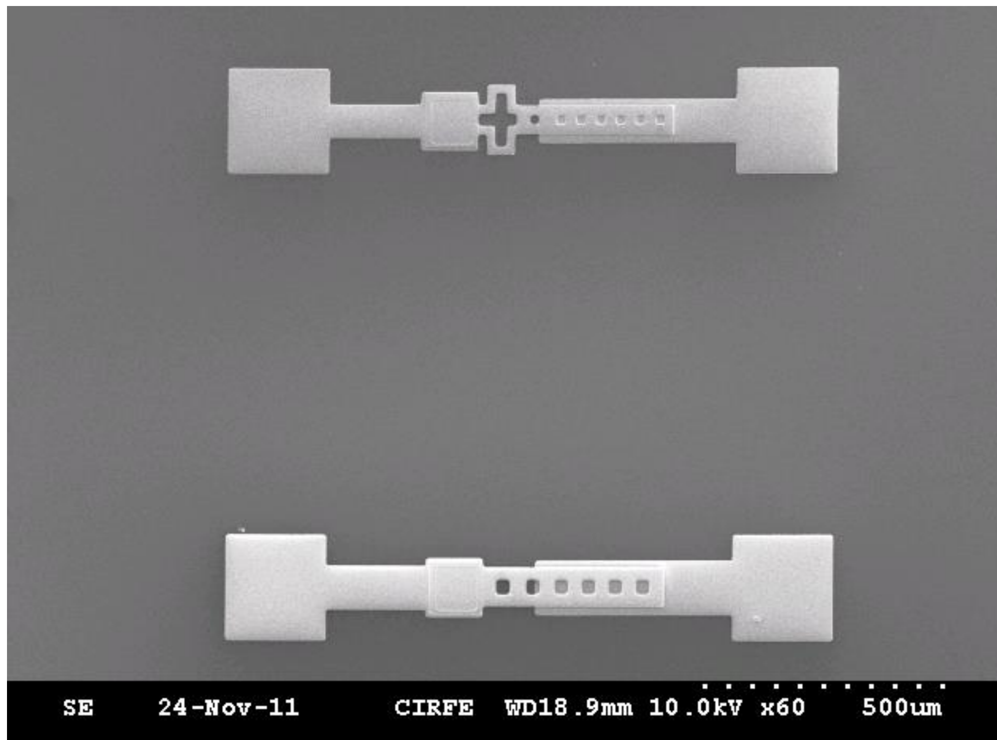

Figure 3-25 Magnetic Reed SW- a) minder shape support SW – width 60um and length 380 um b)SW – width 80um and length 400 um.

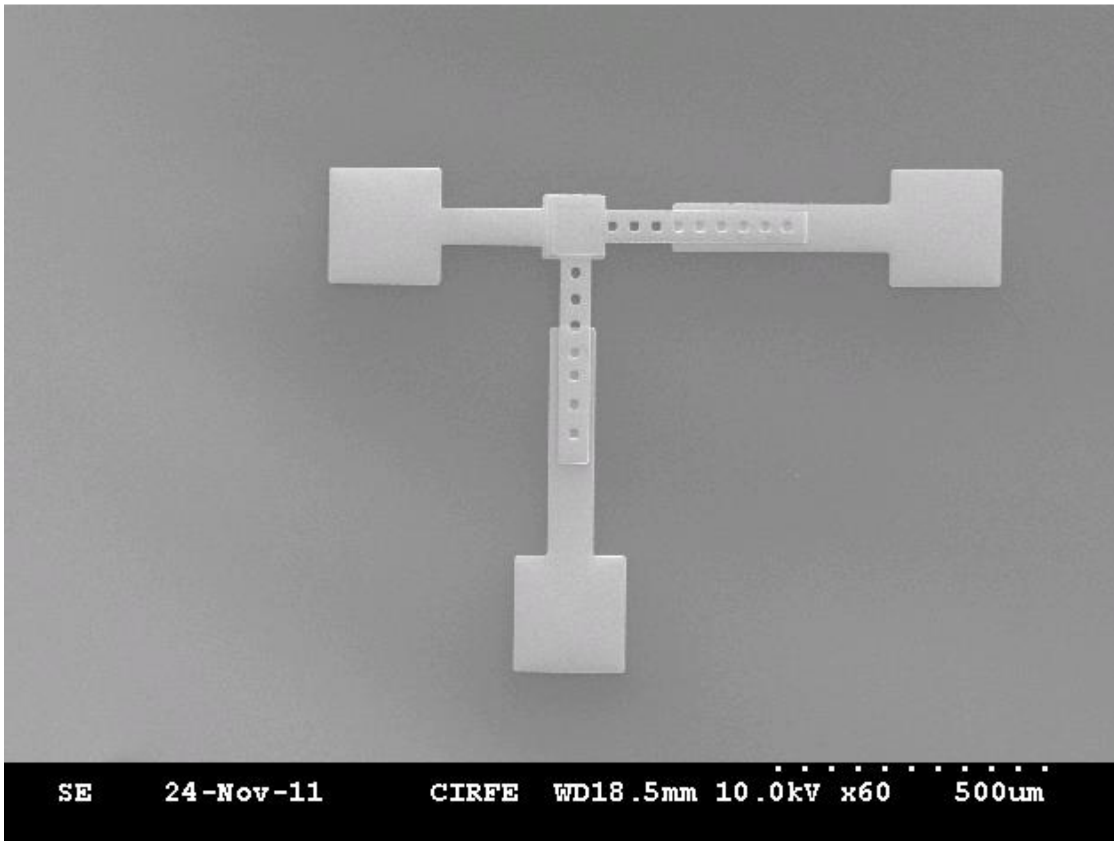

Figure 3-26 An Array of 2 Magnetic Reed SW – width 60um and length 370 um.

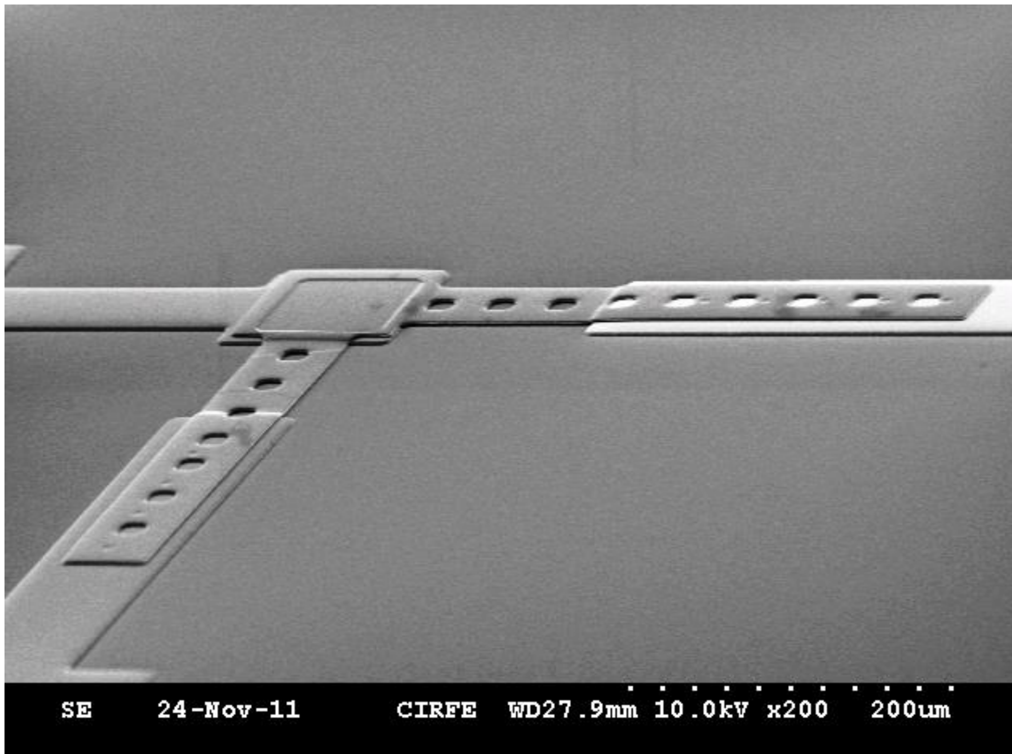

Figure 3-27 An Array of 2 Magnetic Reed SW – width 60um and length 370 um (side view).

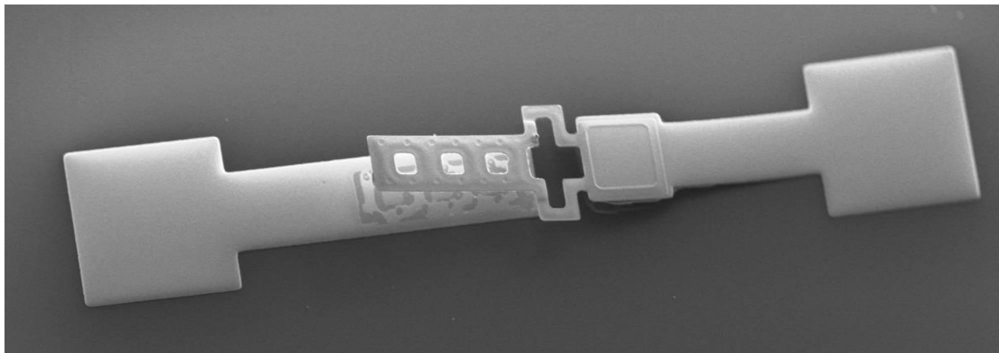

Figure 3-28 Magnetic Reed SW type 2 – width 60um and length 270 um.

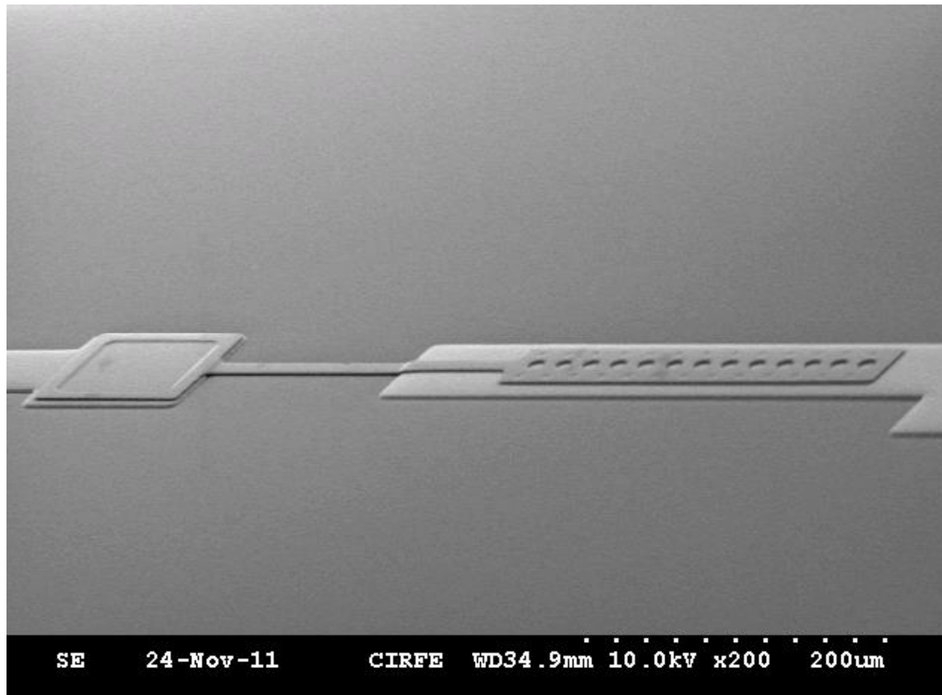

Figure 3-29 Magnetic Reed SW with wide tip type 3 – width (w1: 20um, w2:60um) and length 500um.

3.2.4 Experimental Setup and Measurements

In order to do the measurements, an experimental set up is prepared, which consists of:

- Helmholtz coil
- Custom-made stage
- DC Probes
- Microscope
- Permanent magnets of various field strength

A custom-built stage, fabricated in the machine shop, takes the measurements. The stage stands at the middle height of the coil, and its opening can be controlled in order to accept various dies of devices. The entire stage is made of aluminum, which will not affect the magnetic field in our measurements. A photo of the fabrication setup is shown in Figure 3-30.

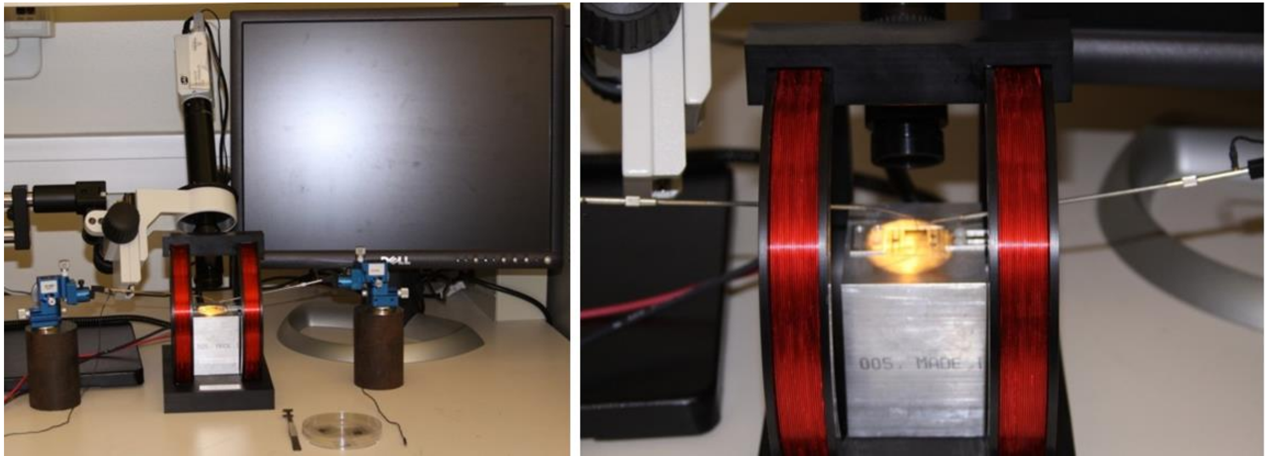

Figure 3-30 Photo of measurement setup and stage.

As shown above, a high magnification microscope is employed in this setup. The microscope has a small lens, so it can be placed directly above the sample. The picture is shown in the monitor connected to the microscope. In this study, measurements are done simply to test if the switches are actuated or not. In order to test this, a multimeter is used to measure the contact resistance of the line. In an unactuated switch, the resistance should be infinite and the multimeter should not show us anything. However, as soon as the switch is actuated and contact occurs, the multimeter should show some resistance, which is related to the contact resistance of the switch.

In the first set of fabricated switches, no results occurred using this method. Even the upper beam was actuated mechanically by a microprobe, and no contact resistance was observed. The problem is caused by the imperfect release of the device. Most likely, some photoresist remains underneath the upper beam, which will isolate the upper beam from the lower one. In order to solve this problem, a new fabrication process is attempted, as discussed section 3.3.

3.3 Tri-layer Magnetic MEMS Reed Sensors

In order to overcome the fabrication problems of Ni-based MEMS sensors, we use a tri-layer of Au/Ni/Au magnetic MEMS reed switch/sensors, designed and fabricated on silicon. The reeds are multilayer nickel beams covered with gold, with dimensions of 300*60 microns. Several types of switches with different configurations are designed and successfully fabricated. A 2D and 3D FEM COMSOL 4.2 simulation is implemented to simulate the switch/sensor. Based on simulation results, a magnetic body force of 5 μN is achieved in a 10 mT magnetic field. This force is more than is

required to actuate the switch. The switches are tested in the lab under a constant magnetic field, and the test results discussed at the end of this section.

3.3.1 Modeling and FEM Simulation

COMSOL Multiphysics 4.2 is employed to simulate the tri-layer MEMS sensors. Using COMSOL built-in physics (AC/DC module and structural mechanics) the magnetic physics is coupled to te mechanical force and displacement.

As in the previous section, the MEMS switches are fabricated on wafers. The bottom electrode is fixed to the substrate (first-level layer) and cannot have any movement and displacement. Therefore, the only moving part in our design is the upper beam. Using the simulation results, and based on fabrication restrictions, we chose the bottom electrode thickness to be 4 microns. The resultant thickness of the upper beam is investigated for 3 microns and 1.2 micron. Based on the results in step 1, the micron thickness beam shows more magnetic body force and has less mechanical restoring force due to being thinner. The gap in our design is assumed to be 1 micron, but larger gaps have also been studied. In order to maximize the actuation force and also reduce the effect of gold on the mechanical performance of switches, the gold thickness was chosen to be 100 nm in thickness.

The beam lengths in the simulation portion of our work are assumed to be 100 microns, with a 50-micron overlapping length between the two beams. The gap is assumed to be 1 micron. A permanent magnet with different magnetization vectors has been placed in various positions and distances with respect to the switch. Finally, the magnetic body force calculated in the AC/DC module is coupled to a structural mechanic module, and the beam's load and movement are investigated.

3.3.1.1 2D FEM simulation

A brief review of simulation steps, along with the results of each step, is discussed and shown below:

A) Choosing the physics

As our first step, we chose a 2D analysis system in COMSOL, and then selected the AC/DC module as a model navigator window. In the AC/DC module, we used magnetostatic fields with no current,

but later on added Plane strain analysis from a structural mechanics module. By selecting stationary analysis as our solving method, we can proceed to the design portion in a GUI window.

B) Drawing system in GUI

The second step is drawing the model in the model builder wizard. Objects of the system are sketched as follows:

A large square of 2*2 mm is sketched and its boundary restricted to be magnetically insulated. This large square is assumed to be our working environment with the whole system within it. The material of this object is defined as air. From this point onward, we will refer to it as the 'environment'.

A 20*25 μm rectangle is drawn as a permanent magnet within the environment, with a corner of (130μm, 50μm) in a Cartesian plane. From this point onward, we will refer to it as the 'permanent magnet'.

The upper beam is sketched with a 1-micron thickness, a 100-micron length, and a corner of (0,0). The bottom electrode is then sketched with a 3-micron thickness, a 100 micron-length, and a corner of (-4μm, 48μm).

The gap in our design is assumed to be 1 micron, but larger gaps have been also studied. Figure 3-31 a-c shows the modeled structure in GUI for the case of without packaging, with glass packaging, and gold beams with nickel tips with packaging.

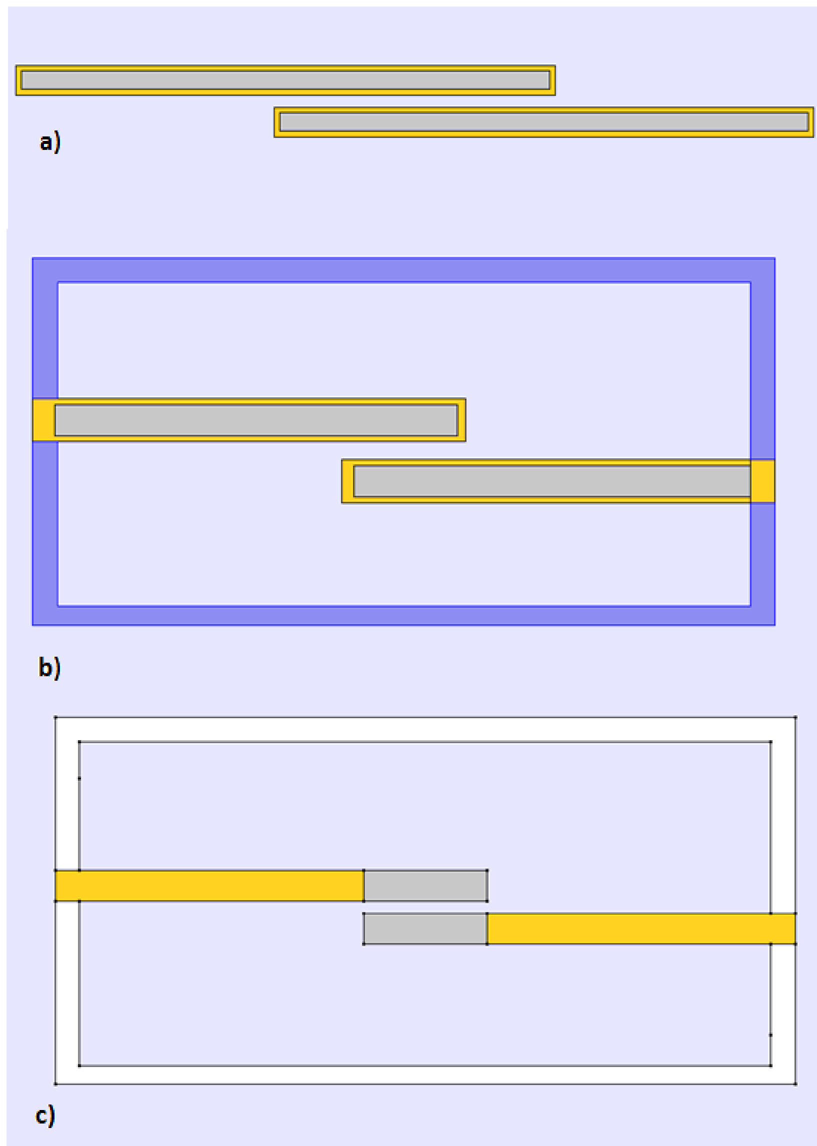

Figure 3-31- The COMSOL geometry 2D sketch of MEMS read switches, for a a)tri-layer without packaging, b) tri-layer with glass packaging and c) nickel tip gold beams with the packaging

By implementing the simulations in these conditions, we see that glass packaging and gold cover do not have much of an effect on device performance. The reason for this is that the H field passes through all non-magnetic material and does not see them in the way. Hence, they cannot have any effect on the H field interaction with a magnetic material.

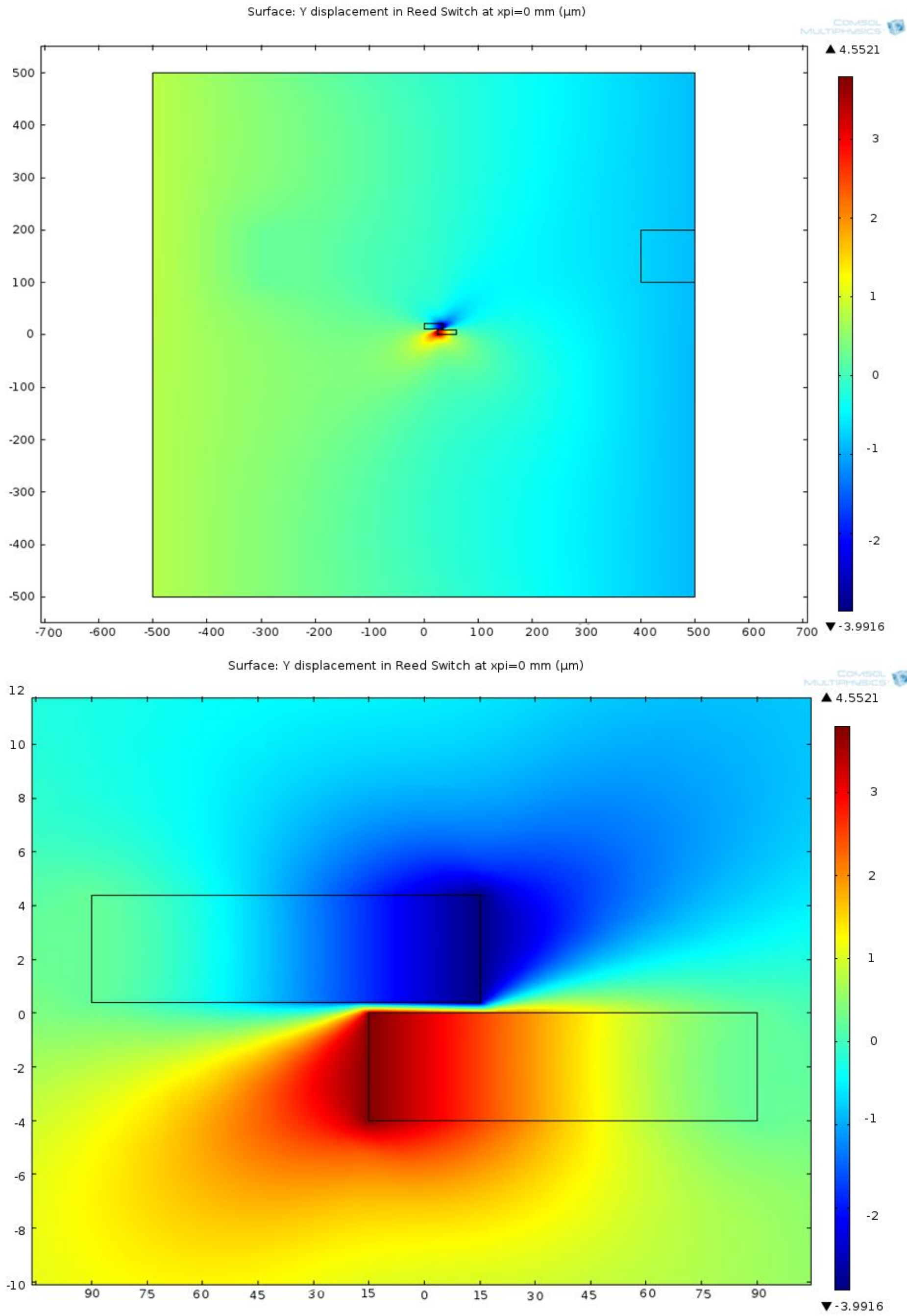

Figure 3-32 the 2D COMSOL simulation for a tri-layer MEMS without packaging, this graph illustrates the vertical displacement of sensors beams in actuated condition (10 mT magnetic field). As shown above, the upper beam is experiencing a 4 um downward displacement which is 4 times greater than our 1 um designed gap.

As shown in Figure 3-35, the tri-layer MEMS sensor shows promising behavior in the desired magnetic field. The packaged sensors are discussed in greater detail in order to fully study the case in a real environment. In the study, the actuator permanent magnet is swept in the X, Y and Z directions. The performance map of the device is concluded and sketched using the results of this step. The schematic geometry of the full model sensor with packaging is shown in Figure 3-34 b. Figures 3-36 to 3-37 show the coupled simulation of the full model sensors.

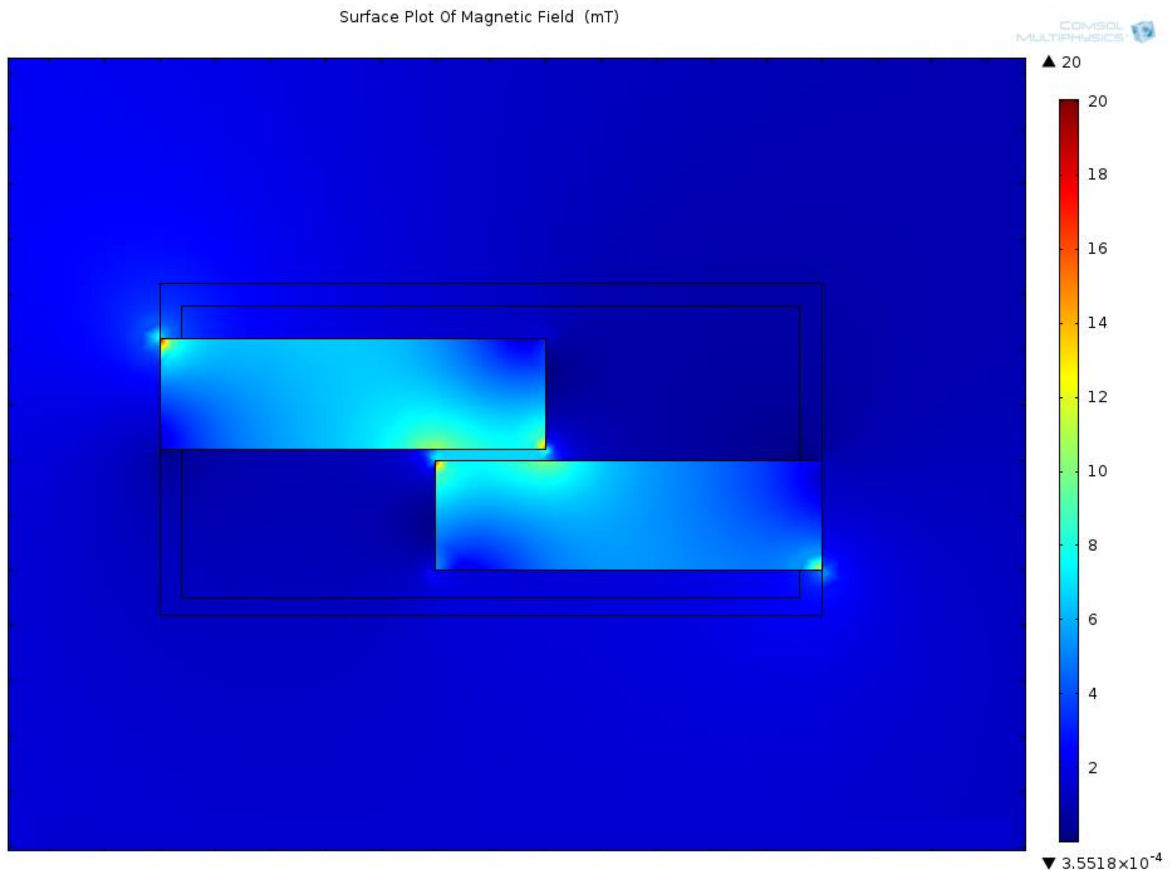

Figure 3-33 Surface plot of magnetic field on Tri-layer MEMS Reed switch with packaging, as shown above, the sensing magnetic field for the actuation is 9-11 mT.

As shown in Figure 3-36 the sensing magnetic field for the sensor actuation is around 10 mT. The surface plot of upper beam displacement and magnified projected out of place displacement of both beams are illustrated in Figures 3-37 and 3-28, respectively.

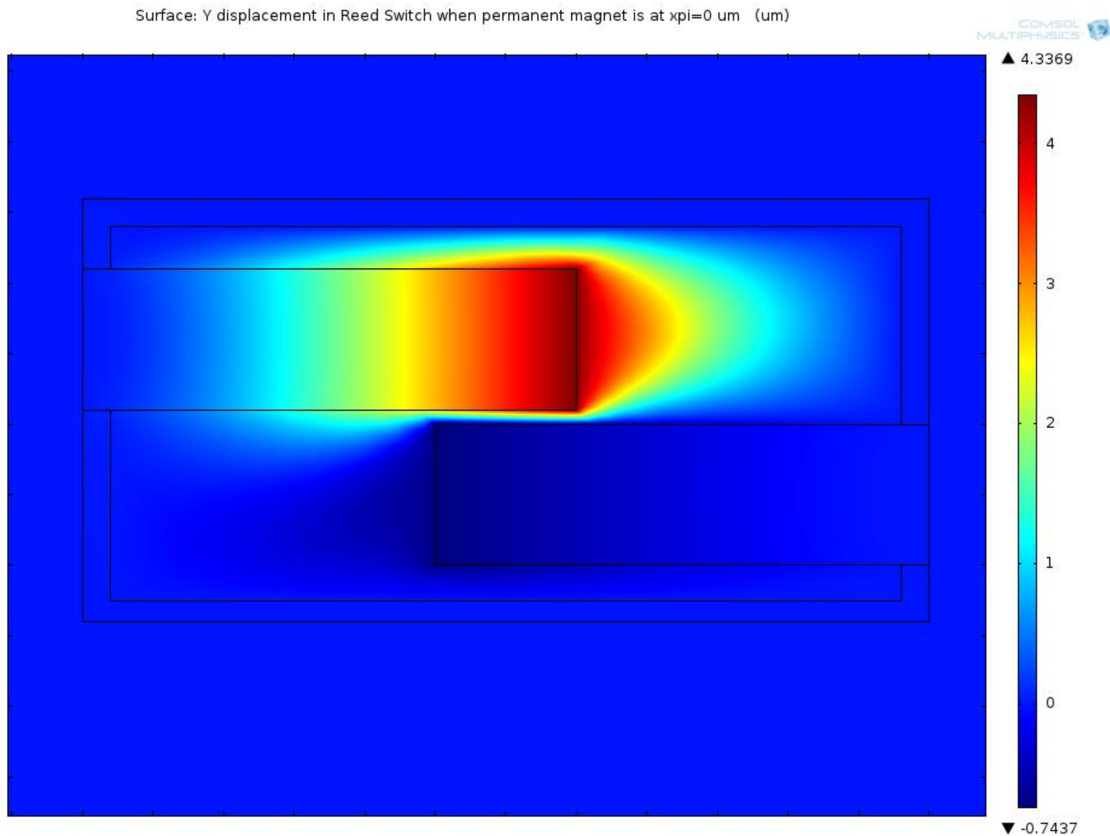

Figure 3-34 the surface plot of upper beam vertical displacement.

The values in Figure 3-37 show the absolute displacement, disregarding the movement direction. Figure 3-38 shows a full displacement model with displacement direction. In Figure 3-38, the blue displacement corresponds to the upper beam, and the red one corresponds to the bottom electrode. Under real experimental conditions, the bottom electrode is fixed to the substrate and the upper beam is the only moving element in the sensor/switch. It should be noted that in all of the simulations, the glass packaging and beam supports are considered as fixed constraints.

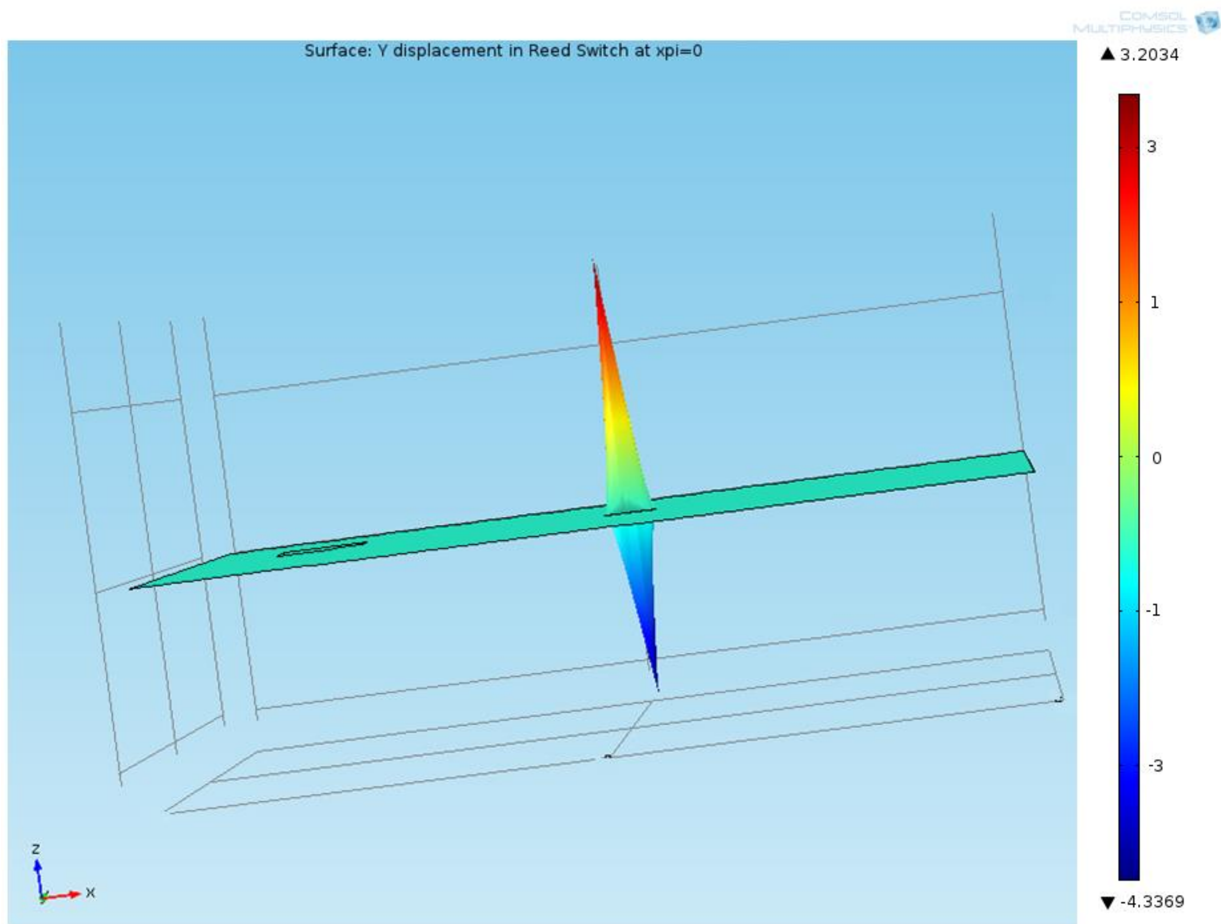

Figure 3-35 magnified projected out of place displacement of both beams. The blue color is corresponded to upper beam with the downward movement whereas the red on is corresponded to the upward movement of the bottom electrode

3.3.1.2 3D simulation of the MEMS Sensors

To finalize the full model simulation a 3D simulation is implemented on the same sensor with the same dimensions and materials. The results are shown below.

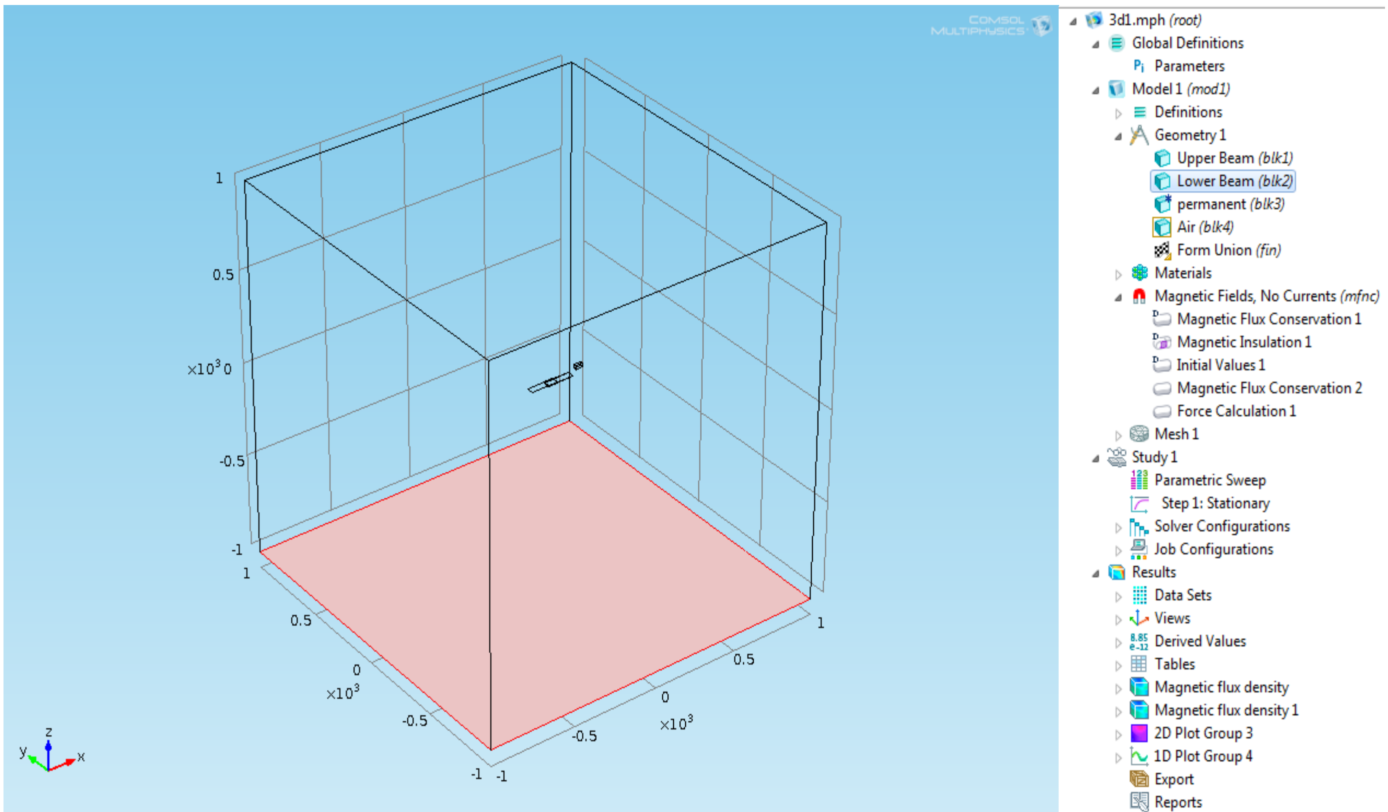

Figure 3-36 Simulation setup and 3D geometric design of MEMS read sensors.

In the simulation, the magnetostatic physic from AC/DC module is coupled to mechanical body force calculations. Thus, the total generated force on the upper beam can be tracked while the permanent magnet is sweeping in different direction. To get a 2D surface plot of the simulations, slicers are added in a post-processing module. The general solution of the simulation is presented in Figure 3-37. Figure 3-38 shows the generated force on the upper beam when moving the permanent magnet in the X direction.

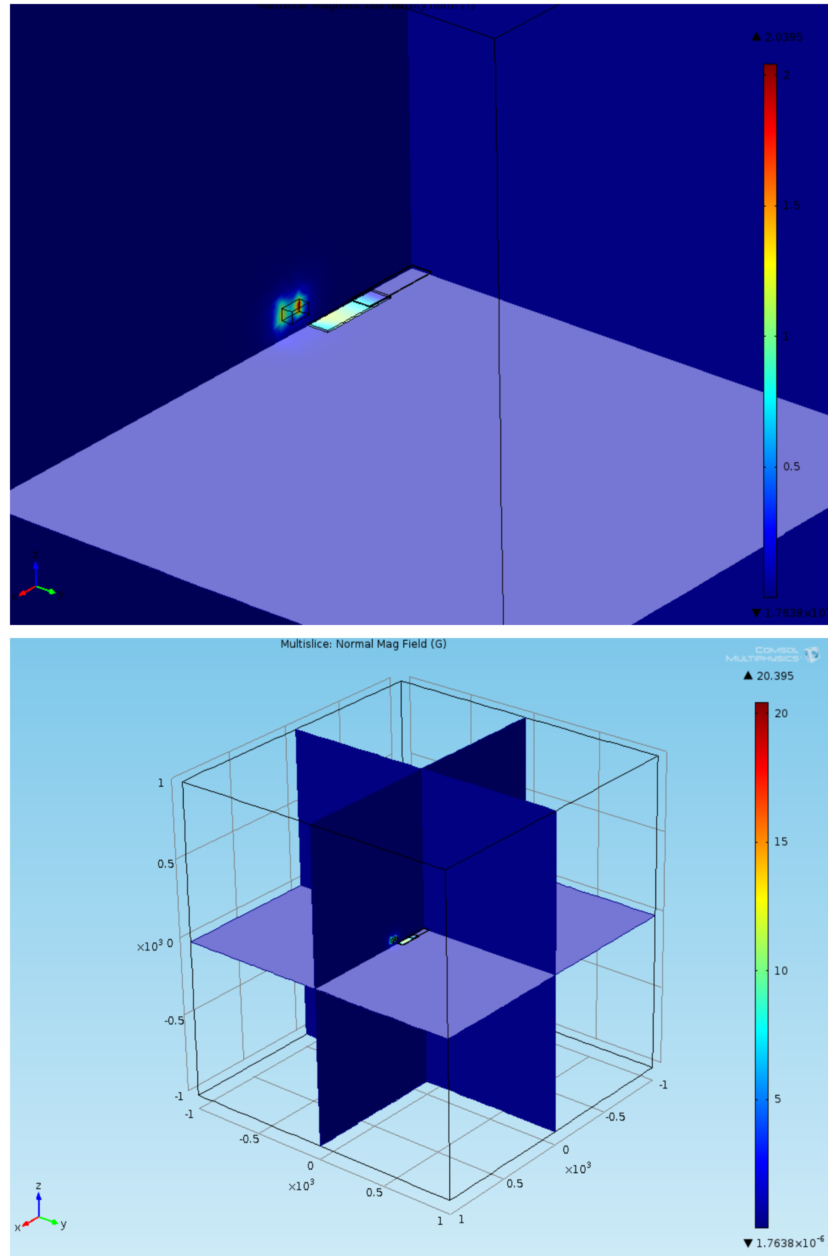

Figure 3-37 Magnetic field distribution over sensor in an actuation step.

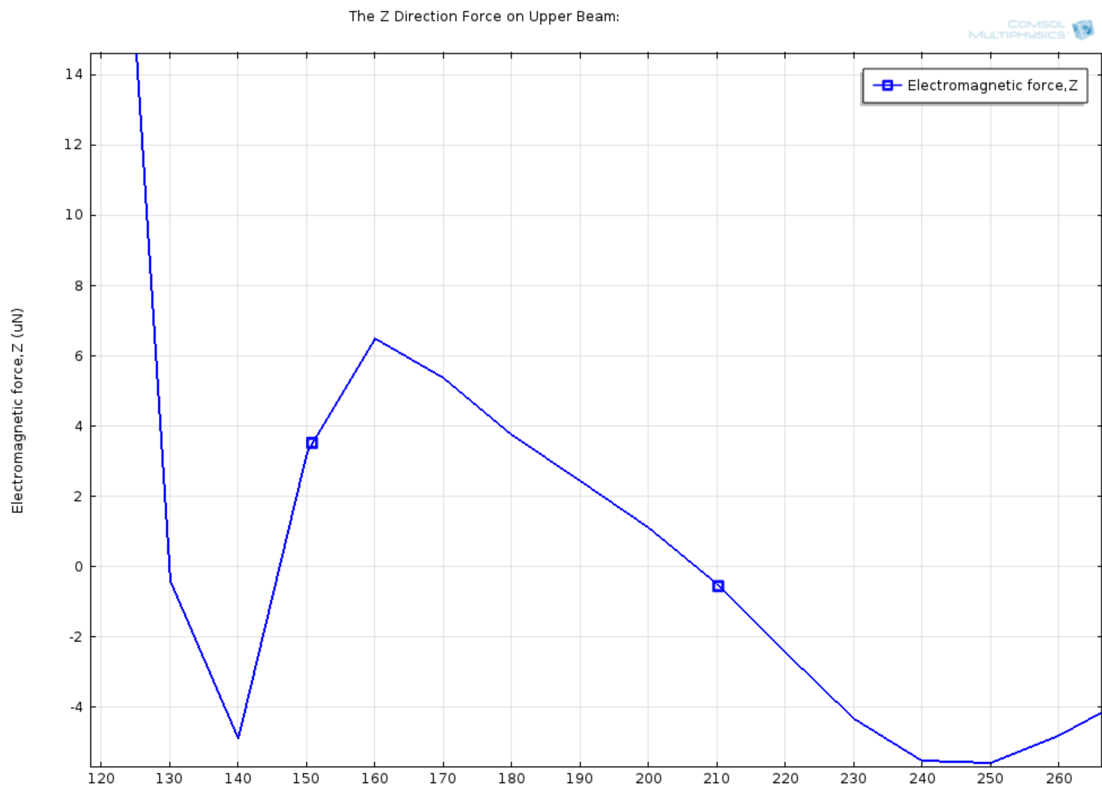

Figure 3-38 Generated force eon the upper beam. In the positions with negative value the actuation will happen. In this figure x axis represents x direction and the unit is micro meter.

3.3.1.3 Performance Map of Sensors

The working map of the sensors is achieved by moving the permanent magnet in X, Y, and Z directions. The generated forces are tracked in different positions and the one conducting to an actuation is picked. A summary of these results is presented in Figure 3-42. Note that this figure illustrates the general trend, and that the values will change based on the magnetic field of the permanent magnet and the size of the sensor beams. In Figure 3-39, the state in which the generated magnetic force is higher (with consideration of a safety factor) than the required mechanical force to actuate the switch is the CLOSED position. This region will always demonstrate the actuated sensor/switch condition. In the same figure, OPEN is the unactuated state of the switch, which contains regions with small generated magnetic force that cannot actuate the switch. Finally, HOLD is the distance range in which the generated magnetic force is in the same order as the required mechanical force. The sensor/switch in this region maintains the state of its previous region. Therefore, when sweeping from a CLOSED state to this region, the sensor/switch will maintain the

CLOSED condition, whereas it will maintain an OPEN condition in the opposite moving direction. The size of these regions will change according to sensor dimensions and external magnet intensity, but the performance trend will remain the same.

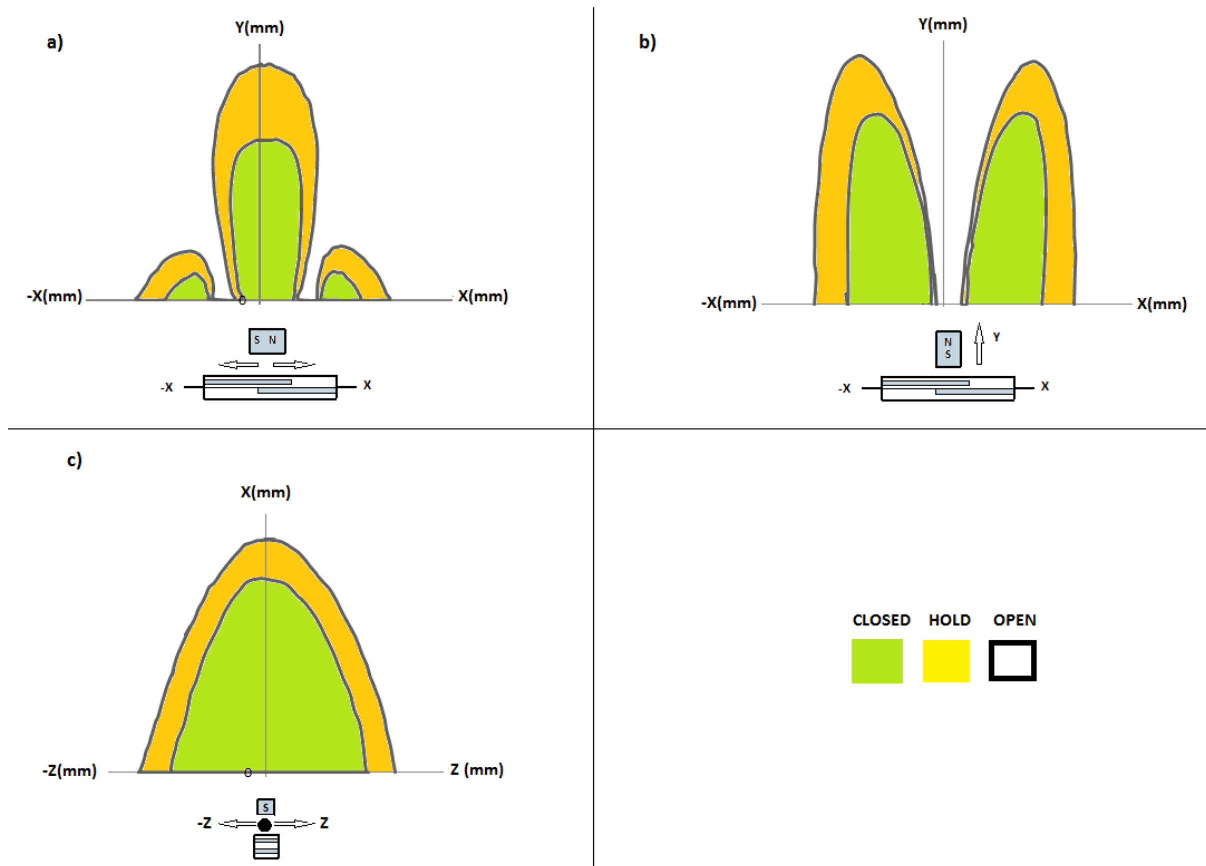

Figure 3-39 Working map of the MEMS Reed sensors, a) when the poles of permanent magnet are in line with longitude direction of the sensor and its moving in that direction, b) when the pole of permanent magnet are perpendicular to the longitude direction of sensors and c) when the permanent magnet is in line with the sensor but it's moving out of the plane far from sensor.

3.3.2 Design Rules and Fabrication Process

The same design rules as section 3.2.2 are applied here to design the samples. In order to reduce the fabrication complexity and increase the quality of the lithography and masking, a non-cyanide

Electroless plating (ELP) of gold is employed here. The ELP layer forms over the top of the copper and nickel. As the base layer here is nickel, ELP gold was successfully used to cover the nickel layers. Using ELP reduces the masking and lithography steps. Hence, in the 7-layer microfabrication of this work, only 4 masks are used, as reported in section 3.2.2.

The fabrication is carried out on three 4-inch silicon wafers. After the RCA cleaning of the wafer, a 0.5 micron of PECVD silicon oxide is deposited on three of the wafers (step a). This dielectric deposition has been done to ensure that the substrate is fully insulated. As the fabrication steps are similar to section 3.2.3, all steps are summarized in Figure 3-43, and the extra steps are discussed.

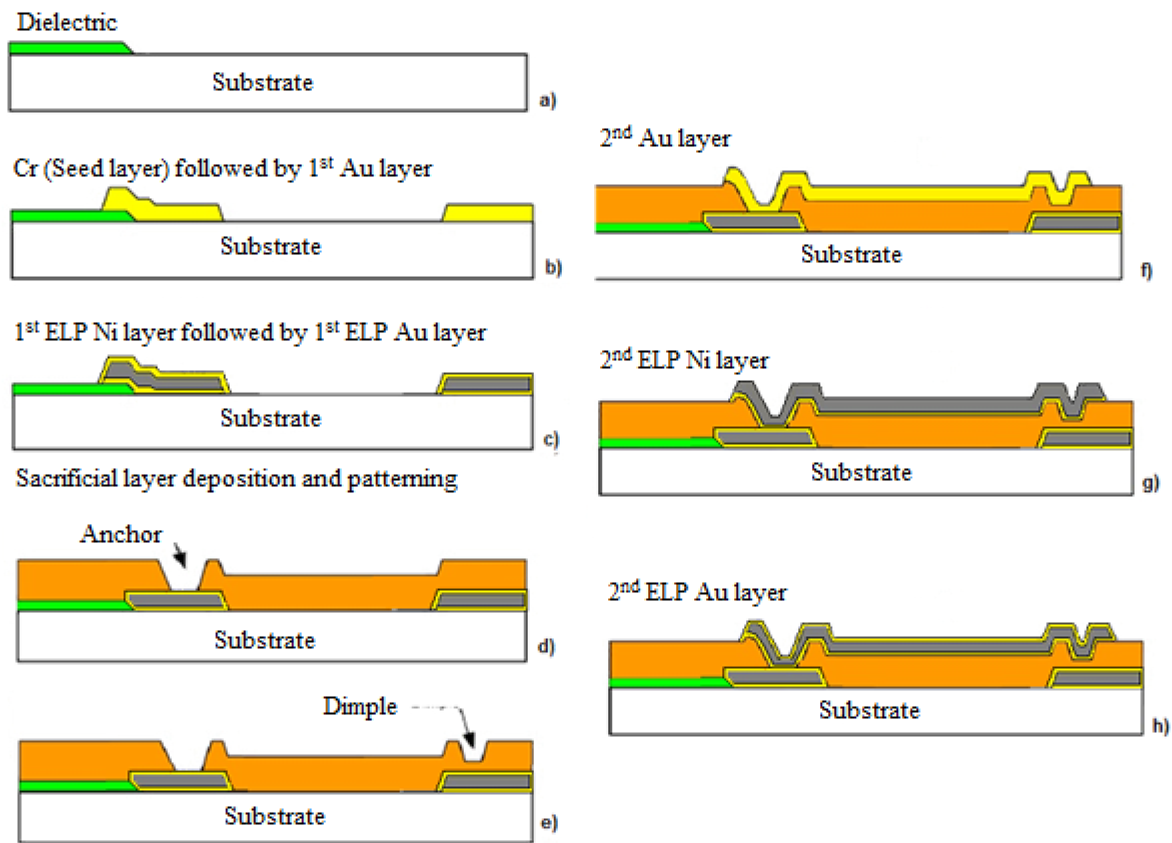

Figure 3-40 Fabrication steps of trilayer MEMS Reed switches

As shown in Figure 3-43, following Step A, a seed layer of Cr (50 nm)/Au (100nm) is deposited on the substrate. The Cr layer serves as an adhesive between the gold and the oxide (step b). In Step B, the first masks are patterned on the substrate using positive photoresist, after which the extra Cr/Au is wet-etched. Next, in Step C, 3 micro meters of nickel are electroless plated on top of the gold. Similar to section 3.2.3, the gold layers had to be agitated with oxygen plasma RIE before plating. The

substrate is then dipped into a gold ELP solution to form 100 nm of gold on top of the nickel. Afterwards, polyimide is spin-coated as the sacrificial layer and cured in the oven at 330°C for 2 hours. After curing the polyamide, mask 2 (anchors) is patterned, followed by dry etching of the PI layer in RIE. Similarly, mask 3 (dimples) is dry etched in RIE. Finally, the upper beam is fabricated on top using the same steps as the bottom electrode. The only difference is that, after deposition of the gold seed layer, the final mask (mask 4) is patterned on it. Detailed fabrication steps with parameters are reported in Appendix C. The wafers are diced into individual die to ensure their release. EKC wet release is used to release the devices. As the nickel layers are covered by gold so they will not be damaged by EKC. After 15 minutes of release in EKC at 60°C, the dice are moved and dipped 3 times in IPA, each time for 15 minutes. At the end of third IPA dipping the dice are moved to the Co2 critical dryer to prevent stiction. Figures 3-44 to 3-46 show the optical microscopic images of various devices made in this stage.

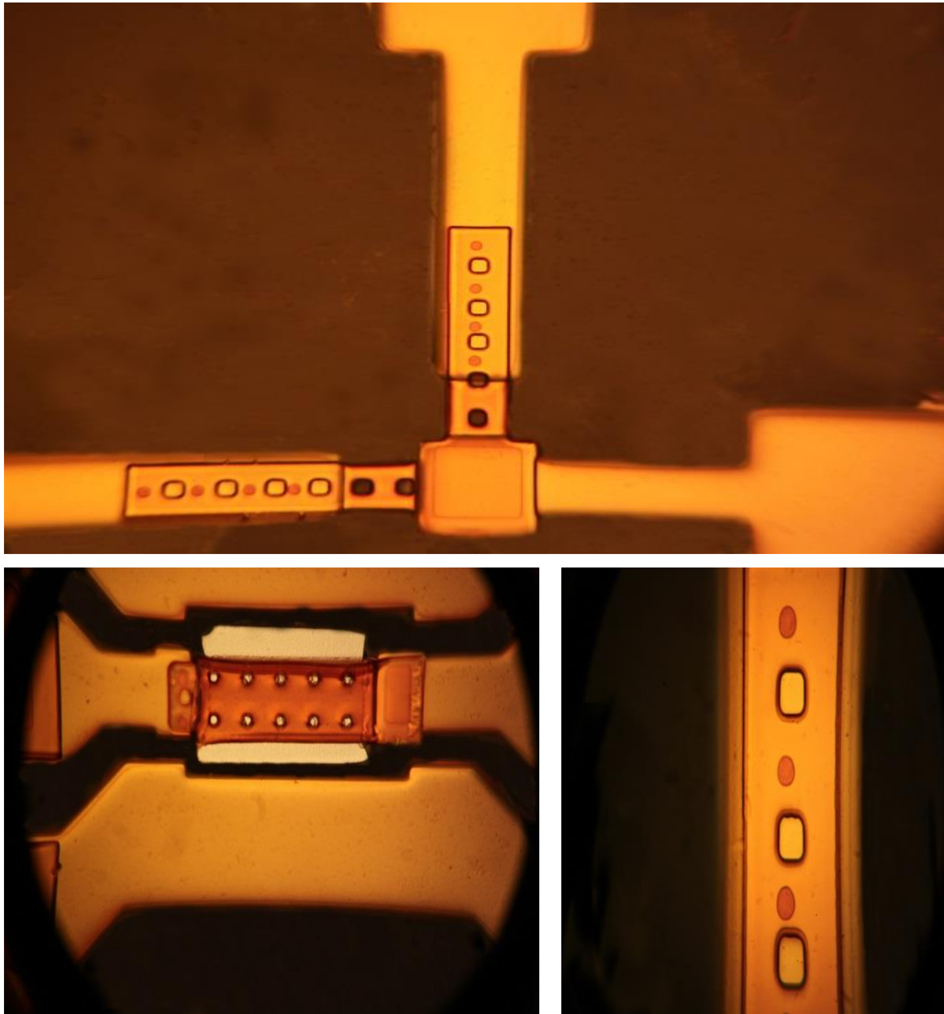

Figure 3-41 Optical microscopic image of trilayer MEMS Reed sensors a)

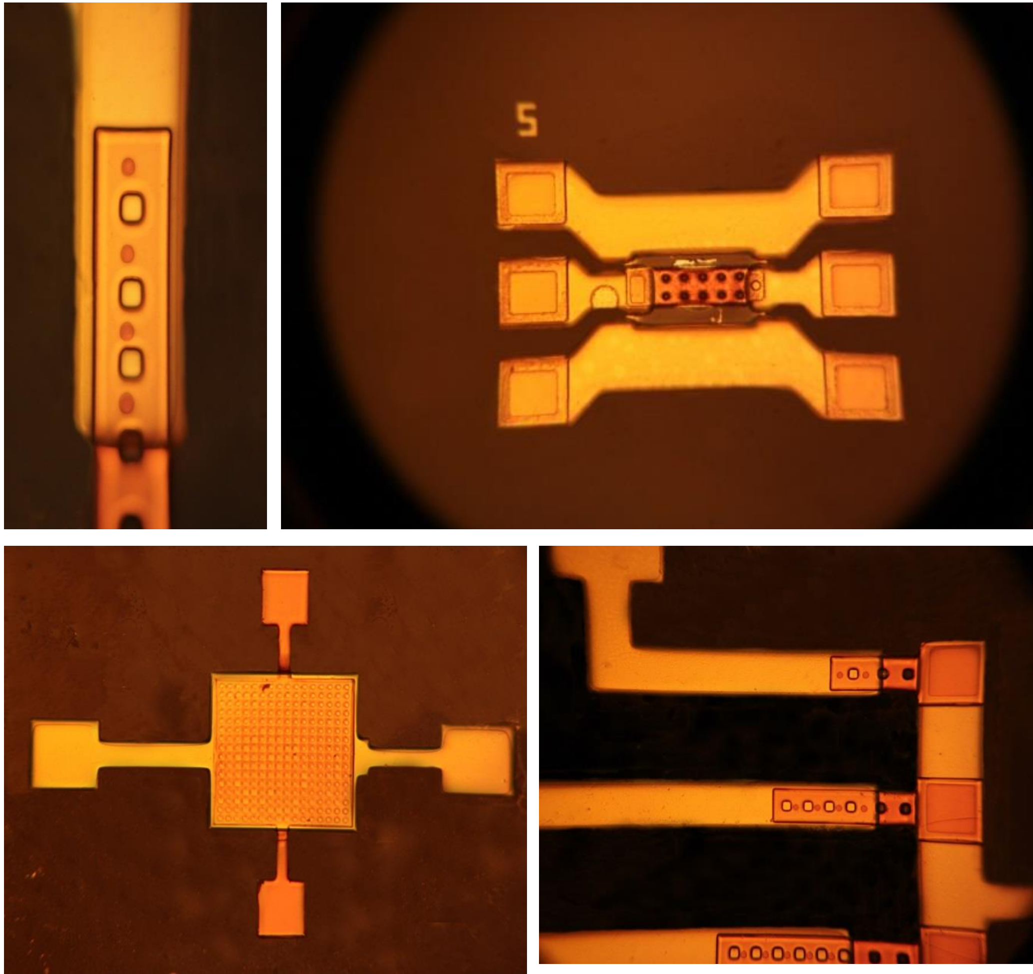

Figure 3-42 Optical microscopic image of trilayer MEMS Reed sensors b)

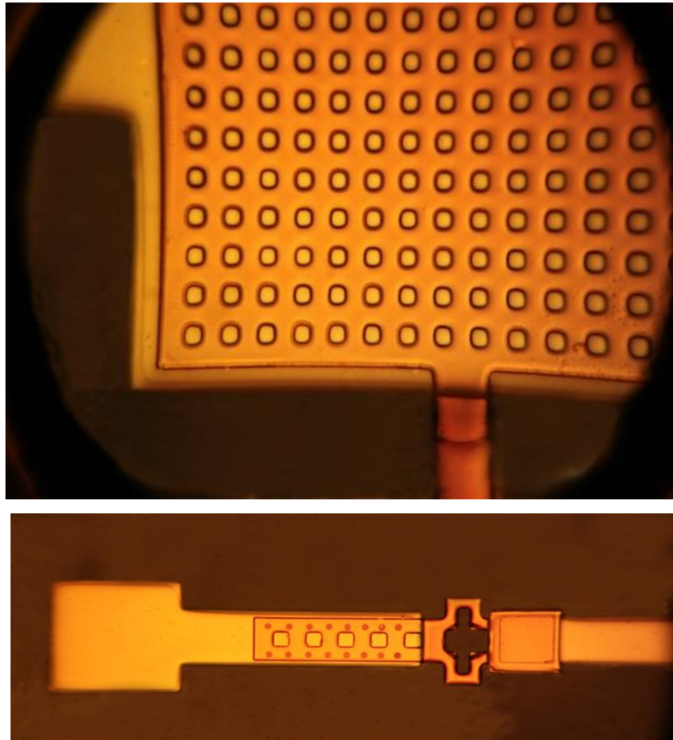

Figure 3-43 Optical microscopic image of trilayer MEMS Reed sensors c)

3.3.3 Test and Experiment

In order to do the measurements, an experimental set up is prepared, which consists of:

- Helmholtz coil
- Custom-made stage
- DC Probes
- Microscope
- Permanent magnets of various field strength

A custom-built stage, fabricated in the machine shop, will do the measurements. The stage will stand at the middle height of the coil, and its opening can be controlled in order to accept various dies of devices. The entire stage is made of aluminum, which will not affect the magnetic field in our measurements. As shown in Figure 3-33, a high magnification microscope is employed in this setup.

The microscope has a small lens, so it can be placed directly above the sample. The picture will be shown in the monitor connected to the microscope. In this study, measurements are done simply to test if the switches are actuated or not. In order to test this, a multimeter is used to measure the contact resistance of the line. In an unactuated switch, the resistance should be infinite and the multimeter should not show us anything. However, as soon as the switch is actuated and contact occurs, the multimeter will show some resistance, which is related to the contact resistance of the switch. The multimeter shows an open circuit in ‘off’ mode, but while we have 10 mT of magnetic field, a contact resistance of 20 ohm is measured. Figure 3-47 illustrates a schematic summary of this measurement.

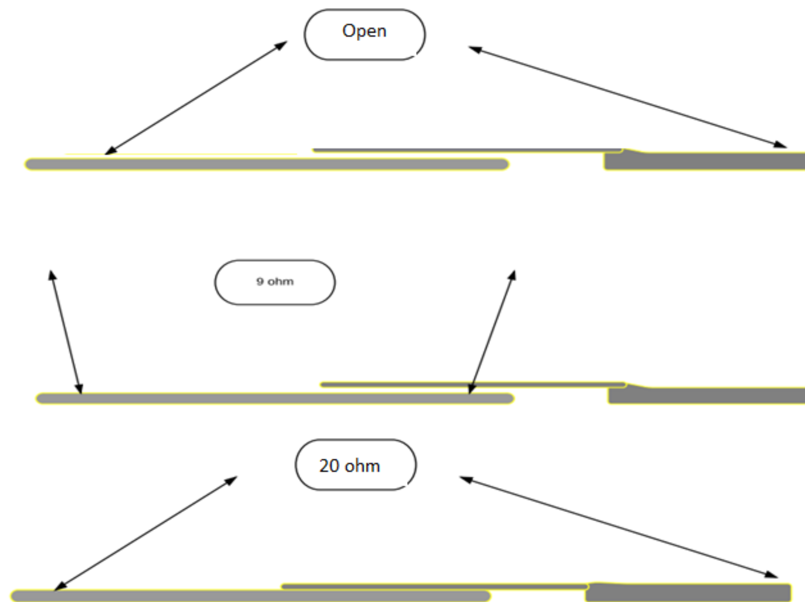

Figure 3-44 Summary of MEMS reed sensor actuation test

4 Chapter Four
Giant Magneto-Impedance Thin film Magnetic Sensors

4.1 Introduction

Magnetic sensors play an essential role in modern technology. They are widely used in nearly all engineering and industrial sectors, such as high-density magnetic recording, navigation, military and security, target detection and tracking, antitheft systems, nondestructive testing, magnetic marking and labelling, geomagnetic measurements, space research, measurements of magnetic fields onboard spacecraft and biomagnetic measurements in the human body [16–20].

A magnetic sensor directly converts the magnetic field into a voltage or resistance with, at most, a dc current supply, and the field sensitivity of a magnetic sensor plays a key role in determining its operating regime and potential applications. For instance, SQUID gradiometers with a high sensitivity of 10^{-10}–10^{-4} Oe have been used for measuring field gradients or differences due to permanent dipole magnets in major applications of brain function mapping and magnetic anomaly detection. Induction, fluxgate and GMR sensors with a medium sensitivity of 10^{-6}–10^{2} Oe have been used for measuring perturbations in the magnitudes and/or direction of Earth's field due to induced or permanent dipoles in major applications of magnetic compasses, munitions fuzing and mineral prospecting. Hall-Effect sensors with a low sensitivity of 1–10^{6} Oe have been used for applications of non-contact switching, magnetic memory readout and current measurements. In addition to the sensitivity requirement, other factors affecting the practical uses of magnetic sensors include processing cost and power consumption. When comparing the processing costs and power consumption of existing magnetic sensors, the GMR sensor shows the lowest cost and power consumption. However, the field sensitivity of the GMR sensor is rather low (~1%/Oe).

Recently, the development of high-performance magnetic sensors has benefited from the discovery of a new magnetic phenomenon – the giant magnetoimpedance (GMI) (i.e., a large change in the ac impedance of a magnetic conductor with an ac current when subjected to an applied dc magnetic field), in metal-based amorphous alloys [21[,[22]. It has been demonstrated that magnetic sensors based upon the giant magnetoimpedance (GMI) effect offer several advantages over conventional magnetic sensors. The decisive factor is the ultra-high sensitivity of GMI sensors. When compared with a GMR sensor that has a sensitivity of ~1%/Oe, the field sensitivity of a typical GMI sensor can reach a value as high as 500%/Oe [17],[20]. Though the development of GMI sensors is still at an

early stage, it is likely that their low prices and high flexibility will warrant wide-ranging application in the near future.

Historically, GMI has attracted particular interest in the scientific community only since Panina and Mohri for the first time announced their discovery of the so-called GMI effect in Co-based amorphous wires in 1994 [15],[19]. In actual ferromagnetic materials, the maximum value of the GMI effect experimentally obtained to date is much smaller than the theoretically predicted value [18]. Consequently, research in this field has focused mainly on special thermal treatments and/or on the development of new materials for properties improvement [15],[24-34]. In order to design and produce novel GMI sensors, a thorough understanding of the GMI phenomena and the properties of GMI materials, with an emphasis on how a magnetic sensor utilising the GMI effect can be best designed for technological applications, is indispensable. The next section aims to provide a comprehensive analysis on the theory, design and fabrication of GMI Thin film magnetic sensor and its potential applications.

4.2 Theory

Based on the frequency (f) of the driving ac, the giant magnetoimpedance can generally be classified into the following frequency regimes:

(i) Low-frequency regime (up to a few kHz), where the changes in voltage at the sample's ends are mainly due to the so-called magnetoinductive effect [21]. The skin effect is very weak in this case. The change in the impedance of the sample upon application of the applied field (Hdc) results mainly from the contribution of inductance (L), which is proportional to the circumferential permeability (l/) for a cylindrical magnetic conductor (i.e., a magnetic wire) or the transverse permeability (lT) for a planar magnetic film (i.e., a magnetic ribbon) [21],[30].

(ii) Intermediate frequency regime (between _100 kHz and a few MHz), where GMI originates mainly from the variation of the skin depth due to strong changes of the effective magnetic permeability caused by the applied dc magnetic field. It is noted here that, depending on sample geometry, the GMI profile can reach its peak in the intermediate frequency range (e.g., 100 kHz to 10 MHz), as a consequence of the contribution of the permeability from both domain wall motion and magnetization rotation to GMI. Reduction in GMI at higher frequencies is related to the domain walls becoming strongly damped by eddy currents and only magnetization rotation contributes to GMI.

(iii) High-frequency regime (several MHz up to GHz), where the origin of GMI is believed to be related to the gyromagnetic effect and ferromagnetic relaxation. The maxima in GMI profiles are

shifted towards higher fields, where the samples are already saturated magnetically [21],[29],[34]. Strong changes in skin depth are caused by the same mechanism as in the ferromagnetic resonance.

There are theoretical various models of GMI representing each of the above-mentioned frequency ranges. In this research, we employed and modified one famous and one generic model.

The advantageous features of the MI effect in a multilayer film can be illustrated by considering the simplified three-layer structure shown in Fig. 4-1. A film of a width b (y-axis) and a length l (z-axis) is composed of an inner conductive lead (M) of a thickness $2d_1$ and two outer ferromagnetic layers (F) of a thickness d_2. An AC current $I = I_0 \exp(-j\omega t)$, flowing in the length direction mainly along the conductive lead if its conductivity (σ_1), is much larger than the conductivity of the ferromagnetic layers (σ_2). The F-layers are assumed to have a transverse in-plane magnetic anisotropy. A DC magnetic field H_{ex} is applied parallel with the current. For H_{ex}smaller than the anisotropy field H_K, a transverse stripe exists as the main structure, as shown in Fig. 4-1b. Magnetic anisotropy is the dependence of the magnetic properties on the direction of the applied field with respect to the crystal lattice. It turns out that depending on the orientation of the field with respect to the crystal lattice one would need a lower or higher magnetic field to reach the saturation magnetization. The effect of this anisotropy field is studied further in chapter 5.

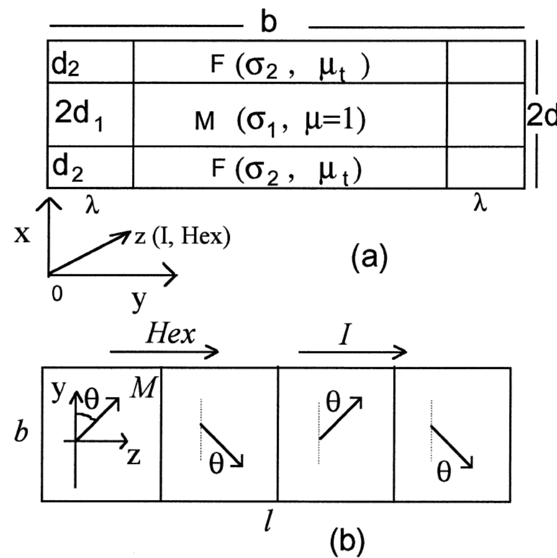

Figure 4-1 Schematic drawing of multilayer MI element, a) cross sectional view b)top view [37].

First, we consider a case where the film width, b, is sufficiently large and the edge effect can be neglected [14], which is valid if $b \gg 2\lambda, \lambda^2 = d_1 d_2 \mu_t, \mu_t$ is the transverse permeability. Within this

approximation, all of the variables depend on the thickness in the film (x) only. The permeability tensor, $\hat{\mu}$, averaged over domains, has a quasi-diagonal form with $\mu_{yz} = \mu_{zy} = 0$. Maxwell's equation can be satisfied by considering the electric field (e_z), and the magnetic field (h_x, h_y) with the condition for the magnetic induction $b_x = 0$, and the boundary condition $h_y(\pm d) = \pm\frac{2\pi I}{cb}$ ($d = d_1 + d_2$). The impedance can be written in a general analytical form as:

$$Z = Rf(x_1, x_2)(\xi x_1 + x_2),$$

$$f(x_1, x_2) = \frac{\coth x_1 \coth x_2 + \xi}{\coth x_1 + \xi \coth x_2} \qquad x_1 = \frac{(j-1)d_1}{2\delta_1}, \quad x_2 = \frac{(j-1)d_2}{\delta_2}, \tag{33}$$

$$\xi^2 = \frac{\sigma_1 \mu_t}{\sigma_2}, \quad {\delta_1}^2 = \frac{c^2}{2\pi\omega\sigma_1}, \quad {\delta_2}^2 = \frac{c^2}{2\pi\omega\sigma_2\mu_t}.$$

Here, R is the DC resistance and will be defined by (34) $\mu_t = \mu_{yy} + {\mu_{yx}}^2/\mu_{xx}$ [31]:

$$R = \frac{l}{2b(d_1\sigma_1 + d_2\sigma_2)} \tag{34}$$

C is the velocity of light (Gaussian units are used). A low frequency ($x_1, x_2 \ll 1$) expansion of Equation (33) together with the condition $d_1\sigma_1 \gg d_2\sigma_2$ yields a simple form for the impedance:

$$Z = R_m\left(1 - 2j\mu_t\frac{d_2 d_1}{{\delta_1}^2}\right), \qquad R_m = \frac{l}{2bd_1\sigma_1}. \tag{35}$$

In this approximation, the contribution of the magnetic layers to the sandwich impedance is described by the external inductance with respect to the inner layer. For the sandwich of a submicron thickness, this is a reasonable approach for frequencies up to several gigahertzes. It may be compared with MI in a single magnetic layer in which a large magnetic response of Z is possible only in the case of a strong skin effect ($x_2 \gg 1$), when $Z \propto {}^{1}/_{\sigma_2} \propto \sqrt{\omega\mu_t}$.

On the other hand, the MI effect in a sandwich film can be very large even at relatively low frequencies when the skin effect is not essential, having a linear dependence on μ_t.

According to rotational magnetization model [32], μ_t will define as:

$$\mu_t = 1 + \left(\frac{4\pi M_s}{H_k \cos 2\Phi + H_{ext} \sin 2\Phi}\right) \sin^2 \Phi$$
$$\sin \Phi = \begin{cases} \frac{H_{ext}}{H_k}, & H_{ext} \leq H_k \\ 1, & H_{ext} > H_k \end{cases} \quad (36)$$

At moderate frequencies ($\omega < \omega_K = \gamma H_K$, γ is the gyromagnetic constant), the field dependence of $\mu_t$has a maximum at $H_{ex} = H_K$.

For a frequency of 10 MHz, taking $d_1 = d_2 = 0.5$ µm and $\sigma_1 = 2 \times 10^{18}\ s^{-1}$ (conductivity of copper), the parameter $\frac{d_1}{\delta_1} = \frac{d_2}{\delta_1} = 0.045$.

A typical low frequency change in μ_t(having a rotational mechanism) under application of $H_{ex} \cong H_K = 10$ Oe is from1 to 10^3. Thus, according to Equation (35), the impedance varies over 400%.

The MI characteristics are found in Equation (33), where the transverse permeability μ_t is considered to be due to the magnetization rotation only, assuming that the wall motion is already strongly damped. The tensor of the rotational permeability is obtained from the linearized Landau–Lifshitz equation [20]. Figure 4-2 shows the MI ratio for $H_{ex} = H_K$ defined as $\frac{\Delta Z}{Z} = \frac{|Z(H)-Z(0)|}{|Z(0)|}$ as a function of reduced frequency $v = {}^{\omega}/_{\omega_\delta}$ ($\omega_\delta = \frac{c^2}{2\pi d^2 \sigma_2 \mu_k}$ $\mu_k = \frac{4\pi M_s}{H_K}$), for various values of the structure parameter d_1/d in (a) and the conductivity ratio σ_1/σ_2 in (b) (calculations for $d_1 =$ 0.5 µm,0.15 µm, and 0.05 µm; $d_2 = 0.01 d_1 - 100\ d_1$

Min b $= 20\lambda$, Max $d_2 = \frac{d_1 \sigma_1}{50 \sigma_2}$).

Figure 4-2a is related to CoSiB/Cu/CoSiB sputtered films. In the case of two identical magnetic layers ($d_1 = 0$), a large MI is seen at frequencies of a strong skin effect $v \cong 1$ (about 60 MHz for d = 1 µm.) with the maximal value of 67% at $v \cong 2.7$. For the same total thickness, 2d, utilization of a Cu-layer considerably improves the MI performance: the impedance changes of more than 50% are

seen for frequencies of an order of magnitude smaller ($v \cong 0.1$), and the maximum of $\frac{\Delta Z}{Z}$ is several times larger. For $\frac{d_1}{d} = 0.3$ and $v = 0.28$, the impedance change reaches a maximum of 470%.

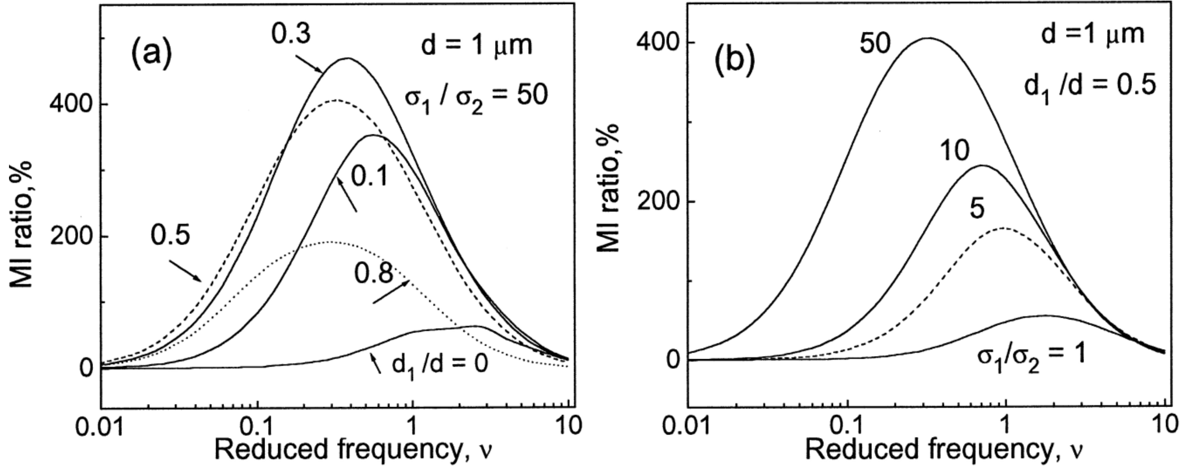

Figure 4-2 Plots of the MI ratio vs. reduced frequency $v = \omega/\omega_\delta$ for a number of parameters d_1/d in (a) and σ_1/σ_2 in (b).Typical parameters used for calculation are:$4\pi M_s = 6000$ G, $H_K = 9$ Oe, $\sigma_2 = 4.5 \times 10^{16}\ s^{-1}$. To avoid the divergence of μ_t at $H_{ex} = H_K$ and $\omega = 0$, a small anisotropy deviation in 5° from y-axis is introduced, the spin relaxation constant is taken to be 0.2. These magnetic parameters are used for all of the calculations [32].

The plots of $\frac{\Delta Z}{Z}$ for various conductivity ratios, shown in Figure 4-2a, demonstrate that the maximum value of $\frac{\Delta Z}{Z}$ increases considerably even for σ_1 just several times higher than σ_2, but a giant MI effect occurring at low frequencies $v \leq 0.1$ requires $\sigma_1/\sigma_2 > 10$.

If the film thickness is further decreased ($< 0.1\ um$), the MI ratio considerably drops to about 15-20%, since the MI effect even for a sandwich structure shifts to higher frequencies where the sensitivity to the field of the rotational permeability decreases. Figure 4-3 shows the theoretical field dependencies of $\frac{\Delta Z}{Z}$ for d=0.1um, with a reduced frequency as a parameter. They exhibit a maximum for H_{ex} of the order of H_K, reflecting the field behavior of the transverse permeability. For a frequency v=0.16 (about 300 MHz), the largest for this case, MI ratio of 14.3%, is obtained at $H_{ex} = 1.3H_K$.

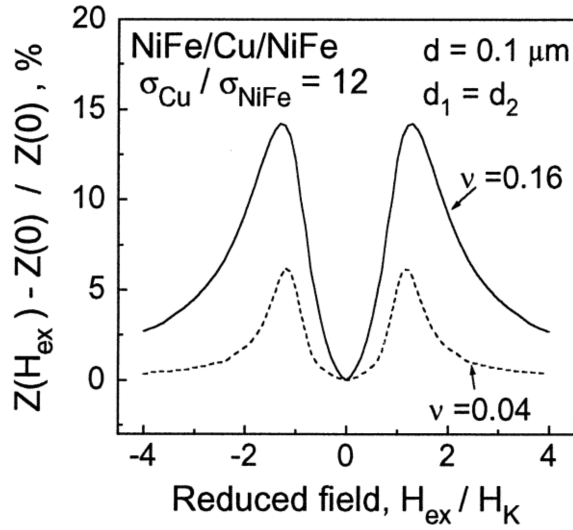

Figure 4-3 The MI ratio as a function of H_{ex} for two frequencies v=0.04 and v=0.16, d=0.1um, $\sigma_2 = 1.7 \times 10^{17} s^{-1}$and $\frac{\sigma_1}{\sigma_2} = 12$(related to NiFe/Cu/NiFe) [32].

4.2.1.1 Dependency to width of the strip (b)

Figure 4-4 shows the plots of the MI ratio vs. frequency with the film width as a parameter, while its thickness is fixed at d=0.5 um and $\frac{d_1}{d} = 0.5$. The calculation corresponds to CoFeSiB/Cu/CoFeSiB films[32]. For a sandwich 100um wide, the result is very close to that obtained from the exact solution Equation (33) for an infinite film. With decreasing b, the MI ratio drops and its maximum shifts to higher frequencies. At frequency v=1 (around 250MHz), $\frac{\Delta Z}{Z}$ of a 100um-wide film has a maximum of 360%, whereas a 10um-wide film shows only 75%. For these dimensions and frequencies, and $H_{ex} \cong H_K$, the characteristic parameter λ is estimated to be about 3um. Hence, b=10um is comparable to 2λ. In general, the AC demagnetizing effect in the multilayer structures essentially reduces the MI ratio if the film width but does not satisfy the condition of b ≫ 2λ.[32]

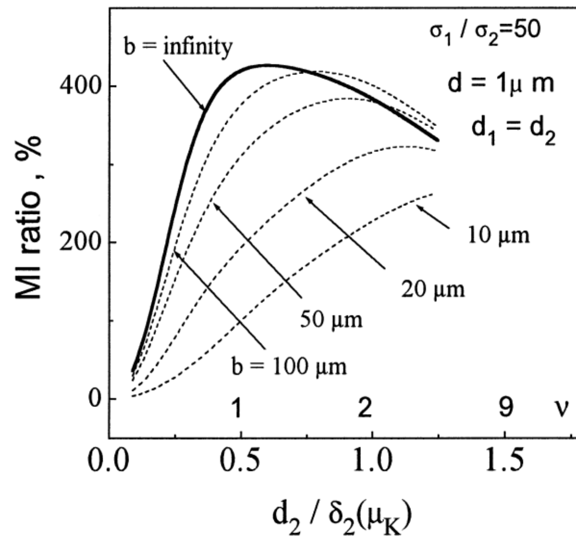

Figure 4-4 Plots of the MI ratio vs. frequency with the film width as a parameter: d=0.5 um and d_1=d_2. The calculation is related to CoFeSiB/Cu/CoFeSiB films [37].

Based on the theoretical model, a simulation has been done to design samples with pick impedance change at 10 Gausses. According to the simulation, two types of samples were designed, as follows:

- Meander type structures

1 mm × 0.5 mm dimensions

Metal trace width: 10, 20, 50, and 100 μm

CoSiB overlap over the metal trace: 10, 20, and 30 μm

- Straight wire test structures

10 mm length

Metal trace width: 10, 20, 50, 100, and 200 μm

CoSiB overlap over the metal trace: 10, 20, 50, 100, 200, 400, and 1400 μm

Simulation results for 1 mm x 0.5 mm resistors:

0.6 um Ag thickness, 200 um line pitch, R = 0.1 ohm, delta(Z) = 90% f = 10MHz.

60 nm Ag thickness, 40 um line pitch, R = 200 ohm, delta(Z) = 1% at f = 10MHz.

It should be noted that changing Ag to Au will have the same results and will even improve the MI ratio.

4.3 COMSOL FEM Simulation

In 2002, Dong [46] presented an analytical model for the permeability change in Giant magneto-impedance metallic glass materials over a frequency and external magnetic field. This analytical model is derived from the Launda-Liftshitz equation. In order to set up the COMSOL simulation, we used the permeability equations to calculate the real and imaginary permeability factors. The results are shown in Figure 4-5 and Figure 4-6.

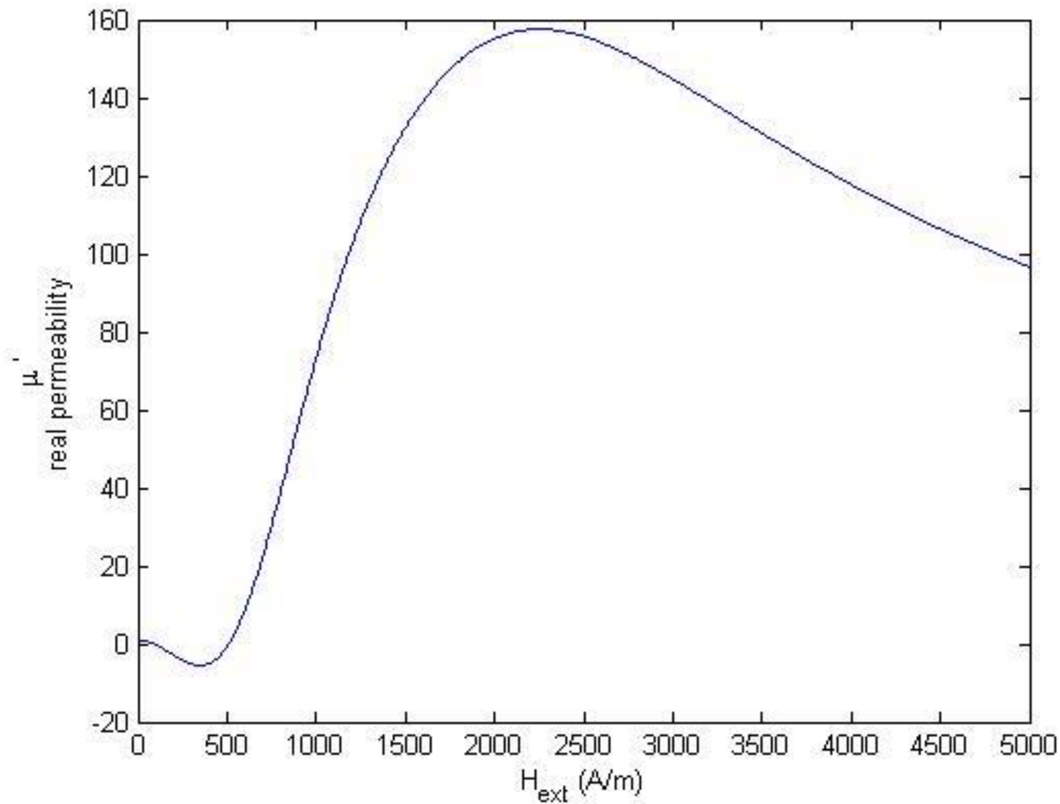

Figure 4-5- The calculated dependence of μ'; the real part of effective permeability, on applied external magnetostatic field H_{ext}

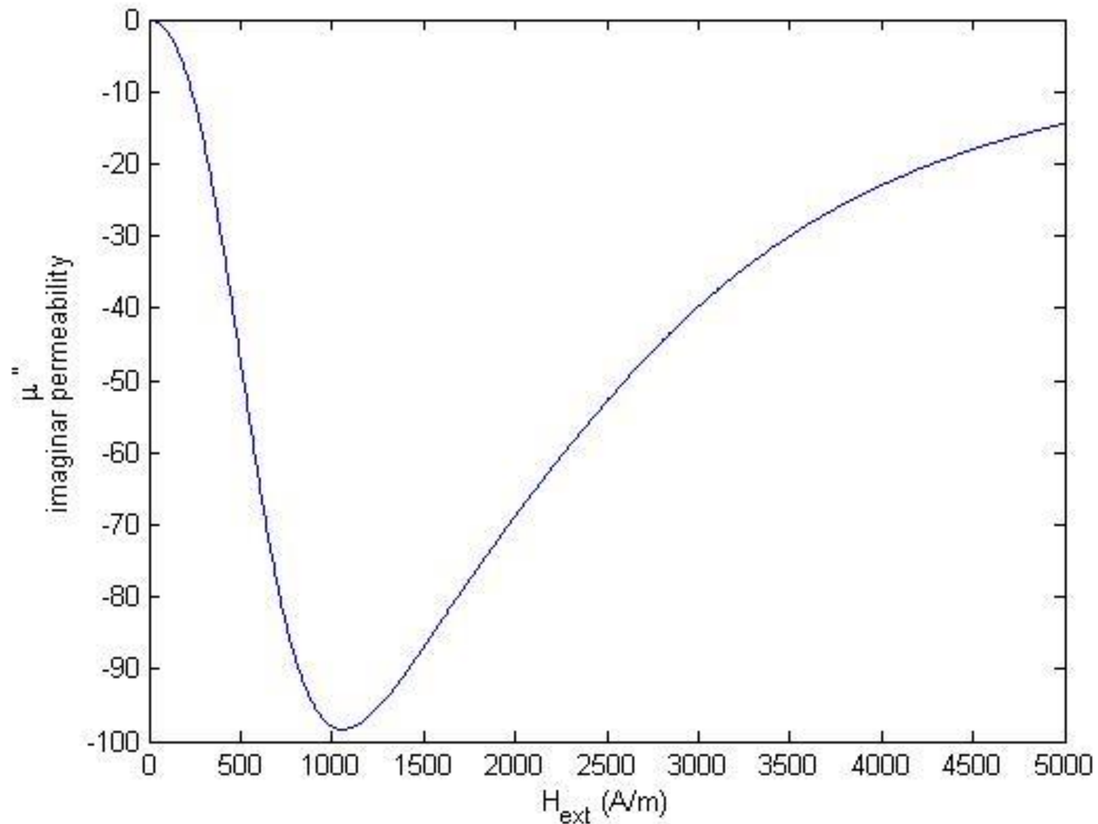

Figure 4-6 The calculated dependence of μ”; the imaginary part of effective permeability, on H_{ext}

After calculating these two variables in MATLAB, the data of these two graphs was fed to COMSOL to solve the GMI equations. In the COMSOL simulation, an AC/DC module is employed with the magnetic and electrical field activated. In order to make it easier for simulation, the meander-shaped devices were assumed to be linear and their total length projected in a linear multilayer GMI structure. A frequency range of 200 kHz to 40 MHz is simulated in this work. In the simulation setup, the AC current is passing the conductive layer (Au) from the upper and lower planes, while the other boundaries are set to insulation. The simulation results are illustrated in the following figures. Figure 4-7 shows the circumferential magnetic flux of the sensor at 1 MHz. This magnetic flux is a result of the current density inside the device.

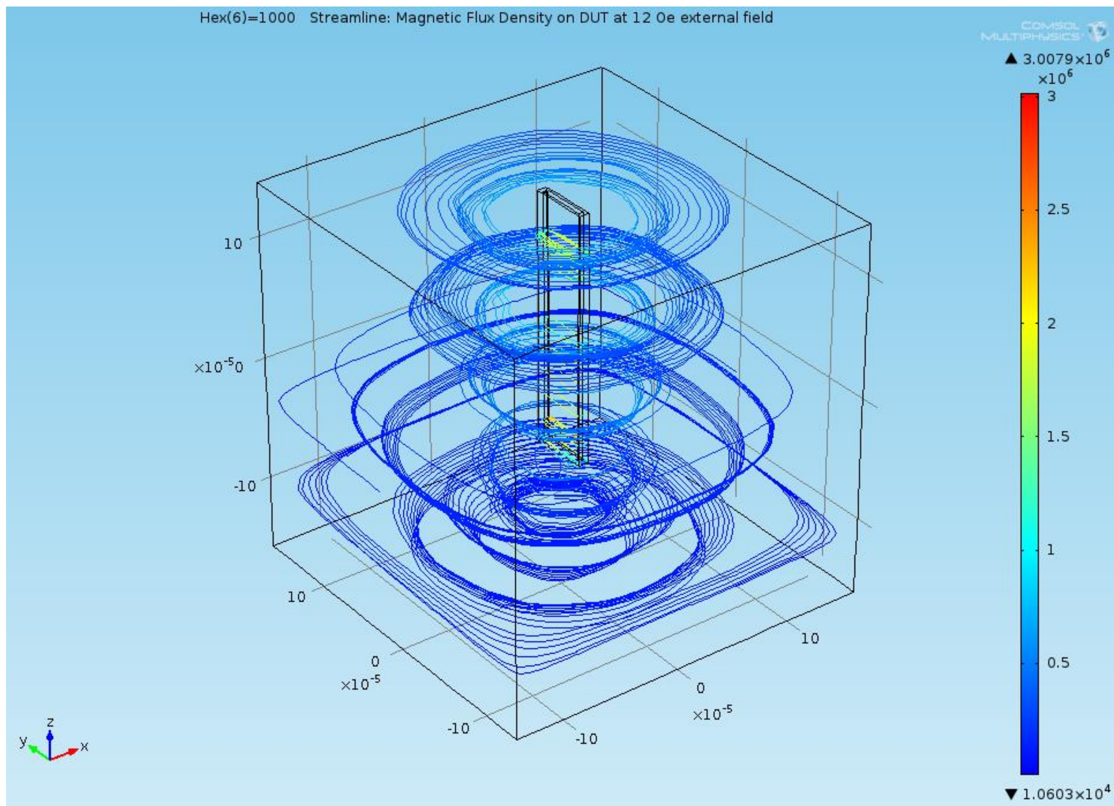

Figure 4-7 Circumferential magnetic flux of the sensor at 1 MHz

In order to see the current density inside the device and study its distribution, the current density on a cross session area is plotted in Figure 4-8. The figure reveals the skin effect in this structure. It is obvious that the current tends to pass through the edges of the cross section area. Another interesting point in this graph is the leakage of the current from the conductive material to the magnetic one. This leakage and accumulation of portion of the current on the edges of the magnetic layer causes the increase in the impedance in higher magnetic fields and frequencies. This leakage is the cause of MI phenomena in multilayer structures.

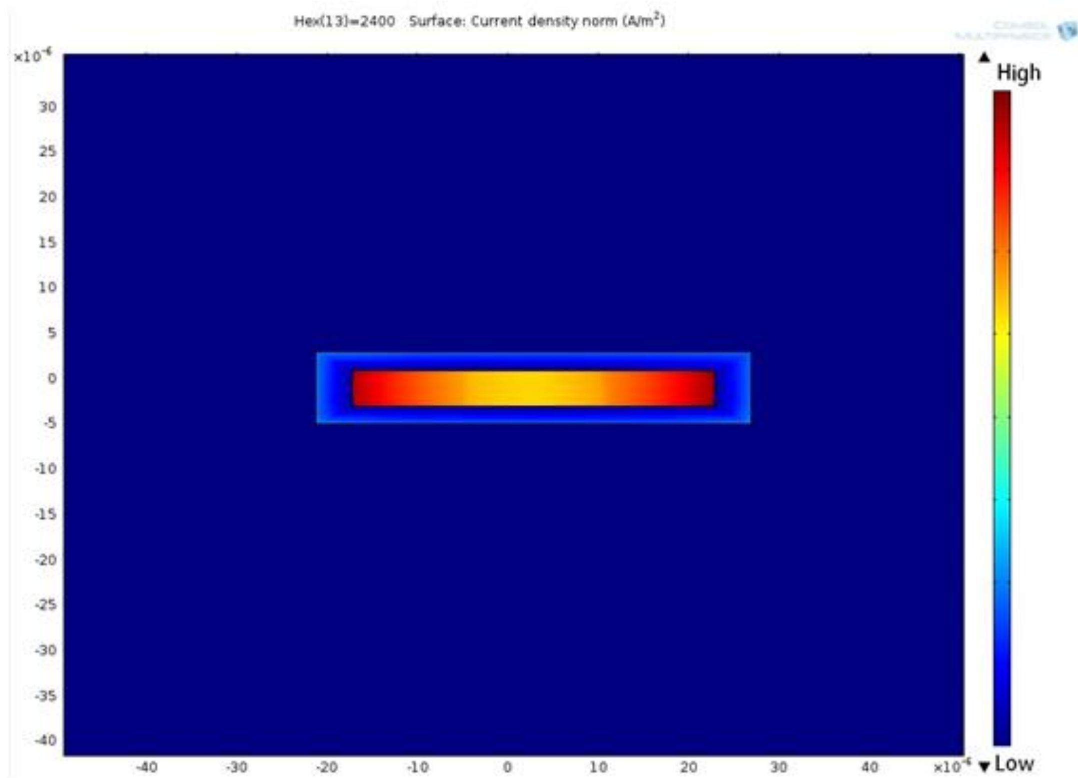

Figure 4-8 Current density distribution along the cross section under the external field of 2400 A/m

Figures 4-9 to 4-14 show the calculated impedance for different frequencies.

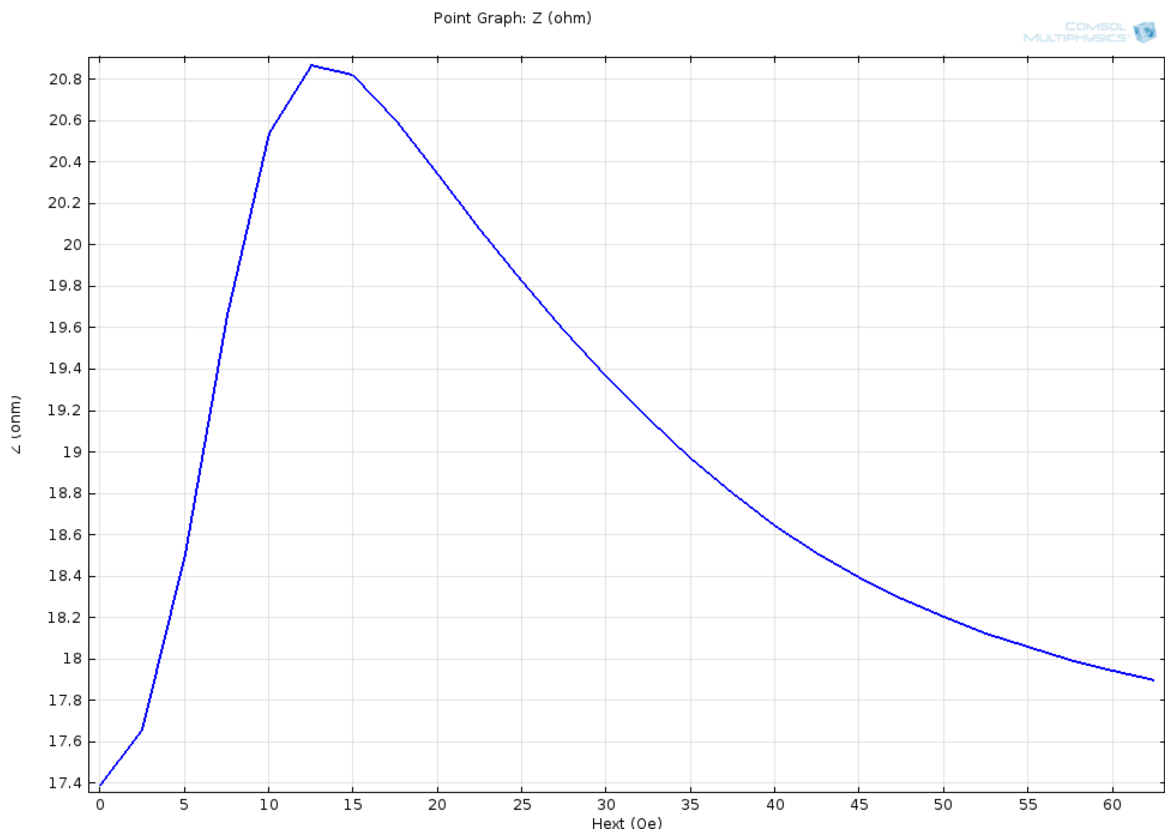

Figure 4-9 Simulation results for impedance of the GMI sensor at 200 kHz

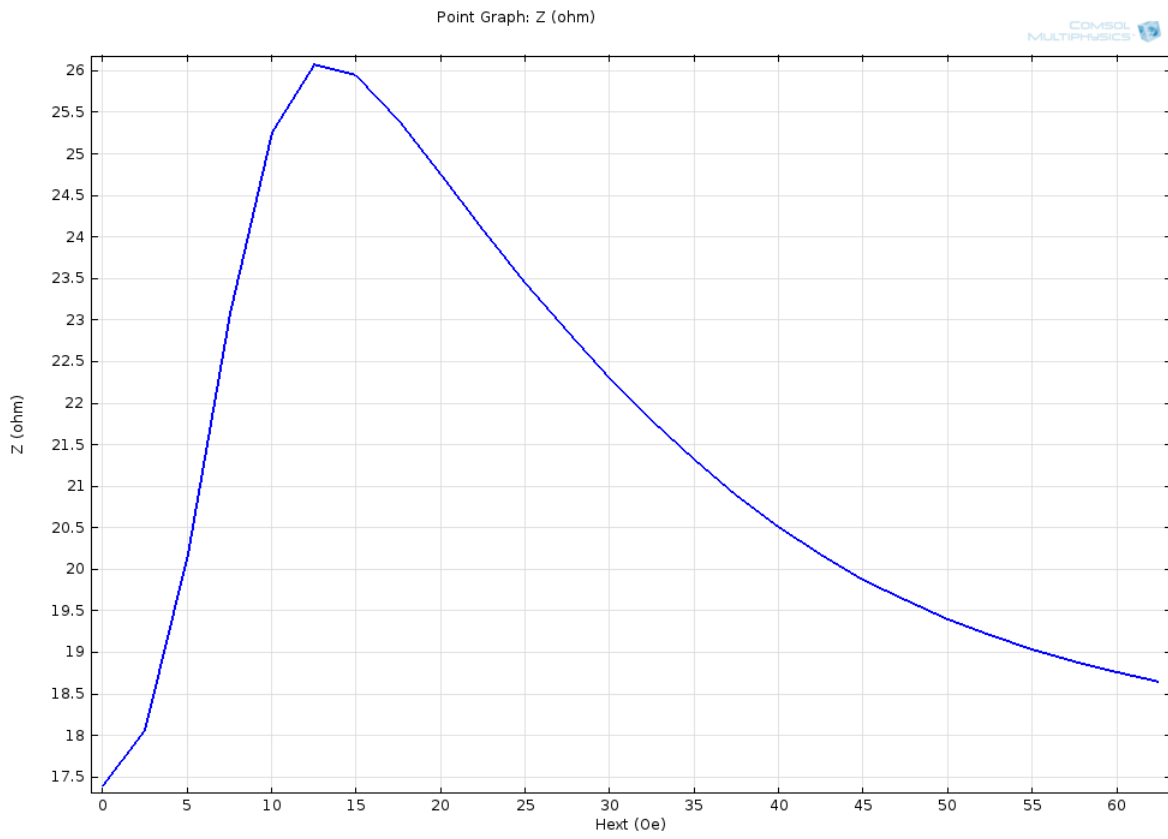

Figure 4-10 Simulation results for impedance of the GMI sensor at 500 kHz

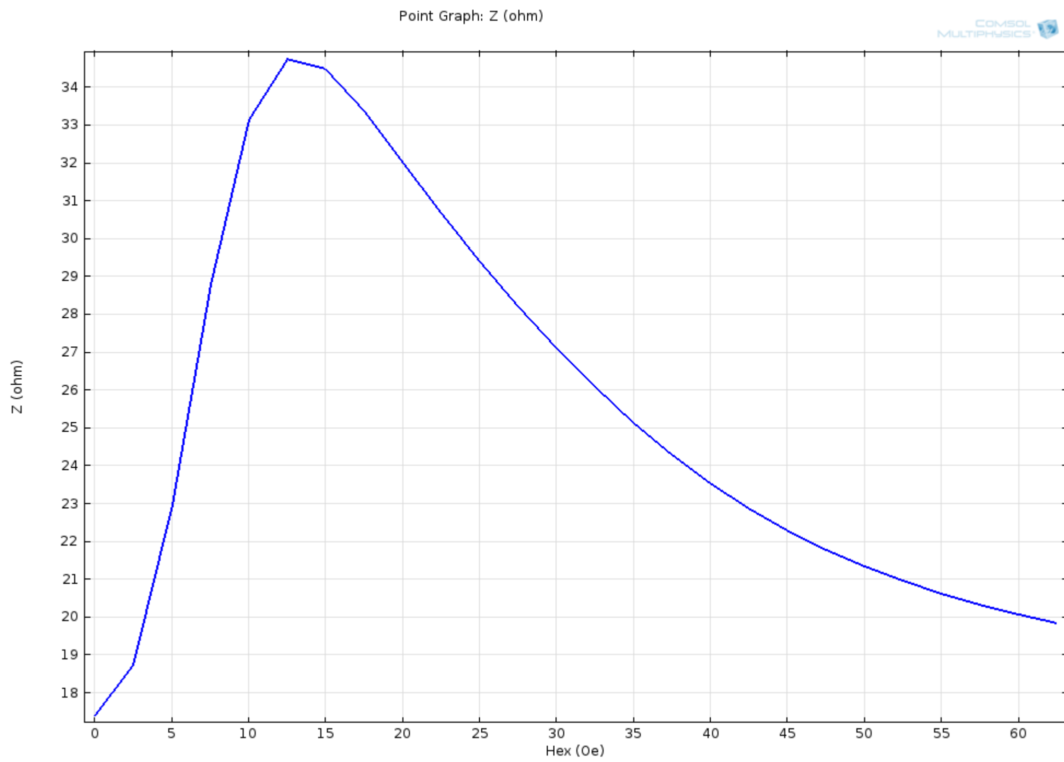

Figure 4-11 Simulation results for impedance of the GMI sensor at 1 MHz

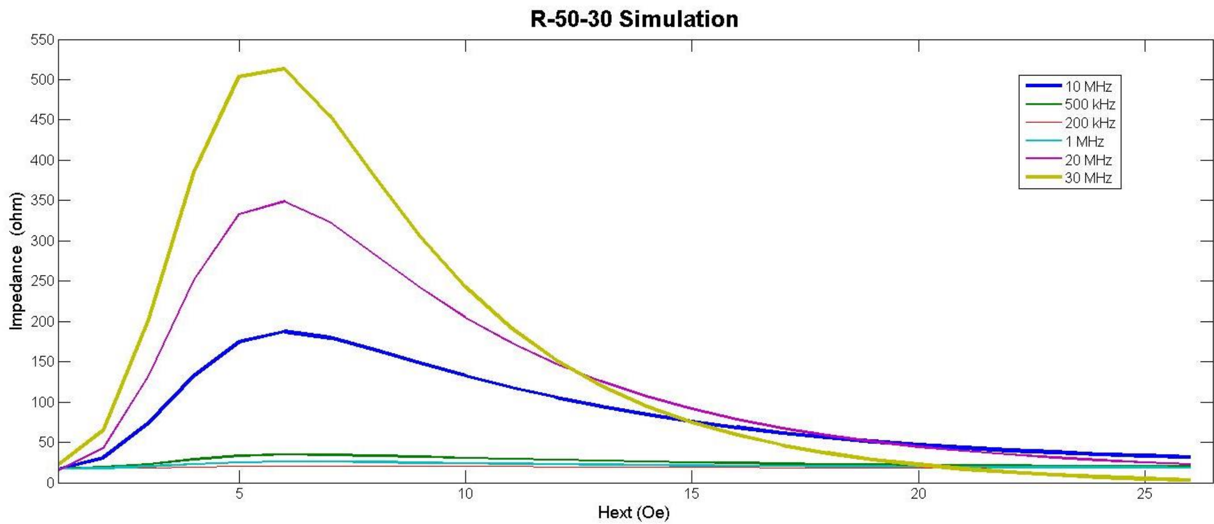

Figure 4-12 The impedance of sample for different ac frequencies under various external magnetic fields.

4.3.1 Study the effect of thickness

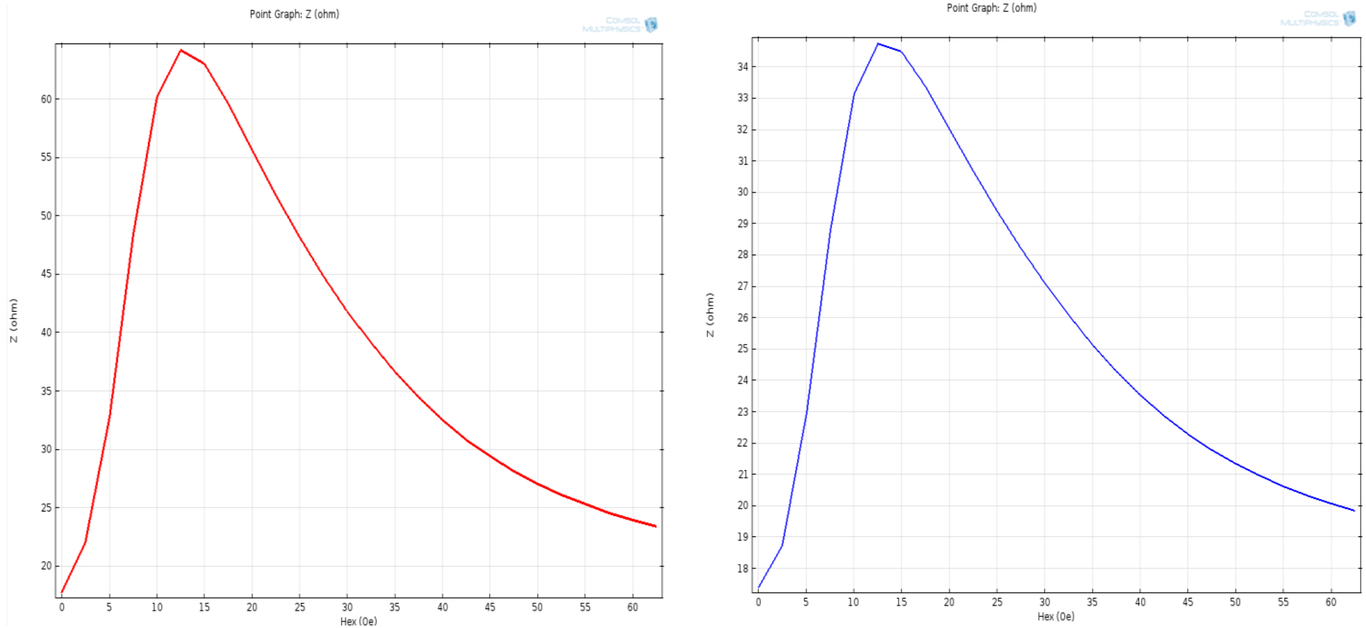

Figure 4-13 Left) impedance of R-50-30 GMI sensor with 2 um thickness at 1 MHz, Right) impedance of R-50-30 GMI sensor with 1 um thickness at 1 MHz,

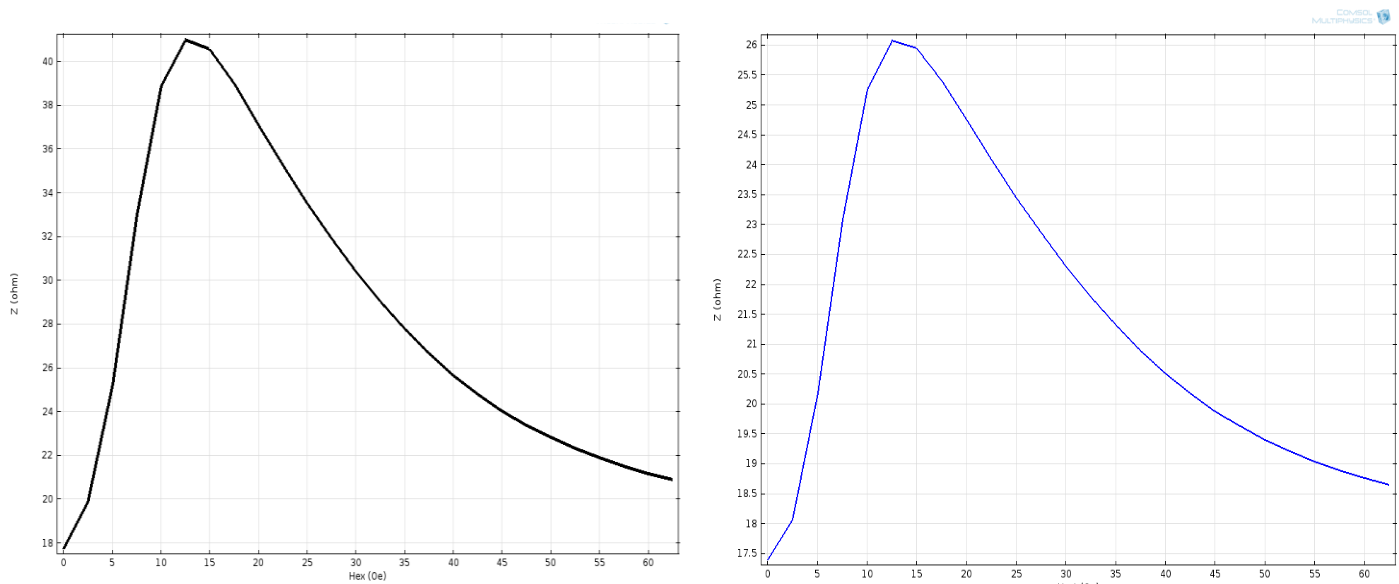

Figure 4-14 Left) impedance of GMI sensor with 2 um thickness at 500 kHz, Right) impedance of GMI sensor with 1 um thickness at 500 kHz,

Increasing the length has a significant effect on increasing the MI ratio. However, increasing or decreasing the width does not have any effect, as long as the overlap remains constant.

4.4 Fabrication Process

4.4.1.1 Material Research

The GMI layer used in this research is CoSiB, and the deposition of this material was done using a sputtering process. As fabrication of this material is new to CIRFE and UWATERLOO, a characterization process was done to develop the fabrication process. The characterization process is reported below:

Deposition rate determined for 2 recipes

- DC Sputtering Recipe #1: 1.67 Å/s
- Pressure = 1.5 mTorr (15 SCCM Ar flow)
- Power = 300 W

- DC Sputtering Recipe #2: 3.1 Å/s
- Pressure = 1.5 mTorr (15 SCCM Ar flow)
- Power = 600 W

Adhesion properties

- No adhesion layer is required
- The samples survived the adhesive tape test on both glass and Si wafers

Etching process developed

- Less than 1 um undercut
- Features as small as 10 um can be fabricated
- Etchant: Ni Etchant Type I Transene + BHF dip

Etchant selectivity is very poor

- Etch rate in gold etchant: > 12 nm/s
- Etch rate in Cr (CR14) etchant: > 12 nm/s

Electrical resistivity determined: 18.7 μΩ.m

4.4.1.2 Fabrication Process

The fabrication sequence is illustrated in Figure 4-15:

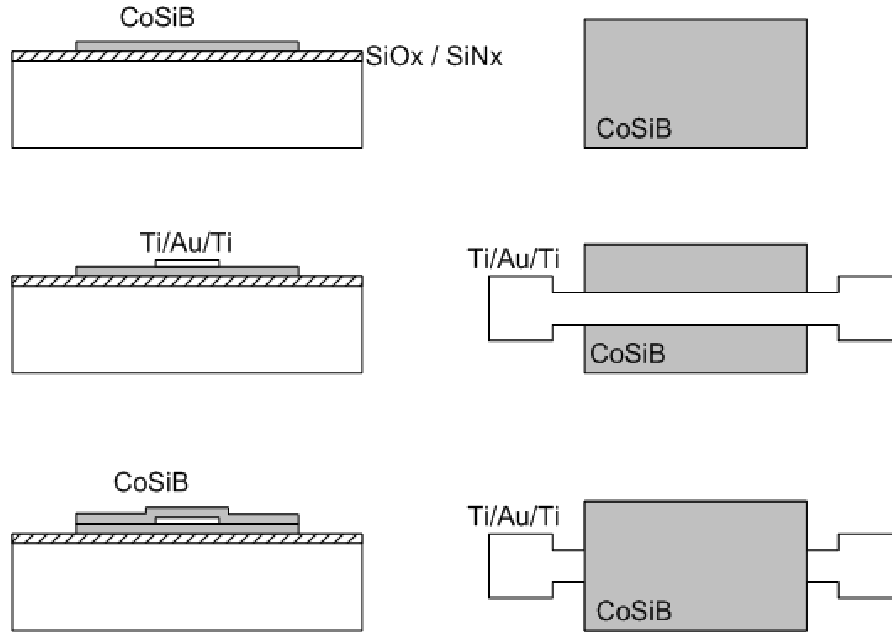

Figure 4-15 Fabrication process sequence of GMI samples.

GMI thin film magnetic sensors were fabricated on 3-inch glass wafers. At the outset of the fabrication process, the wafers were placed for RCA cleaning, after which the deposition of CoSiB using the intelvac deposition system was done. The deposition is performed as a DC sputtering in 1.5mTorr (15 SCCM Ar flow) pressure and with 600W of power. The measured deposition rate was 3.1 Å/s. In the next step, the deposited CoSiB layer was patterned using positive photoresist; unwanted parts were etched away using a Ni etchant. The accuracy of the patterning step yielded a 10-um feature size. Following the characterization of the wafers in this step, 2um of undercut was observed, as shown in Figure 4-16.

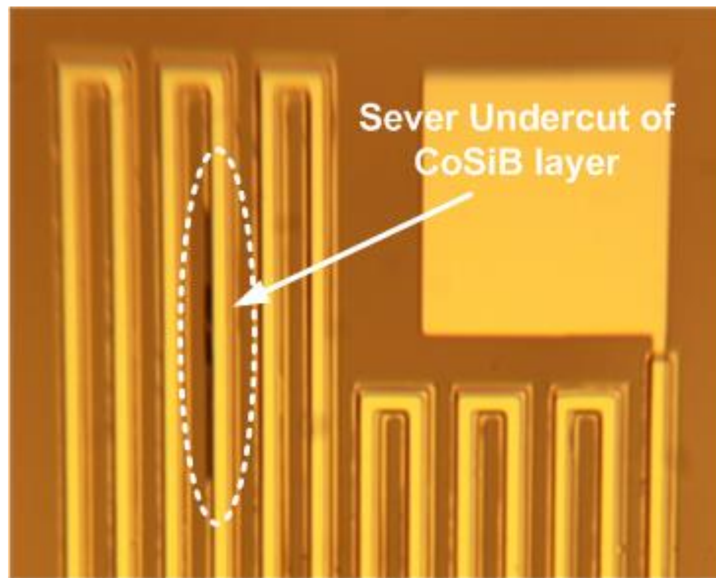

Figure 4-16 Undercut of CoSiB sample.

A thin film adhesive layer like Ti needs to be deposited on top of the wafers. This layer is also needed to save the CoSiB layer from etching by an Au etchant; otherwise, the wet-etching of the layer will be unsuccessful, as the CoSiB layer is attacked by Au etchants at rates faster than Au. A thicker Ti barrier/stiction layer is required that will undermine the potential performance of the device. Therefore, in this step, a Ti/Au/Ti metal layer is deposited and patterned. Afterwards, Gold resistivity, measured by the Van der Pauw method and with a sheet resistance equal to 92 mΩ. Ti/Au/Ti, is patterned, using the lift-off process. It should be noted that the kwik strip solution mildly but negligibly attacked the CoSiB layer.

Optical images of fabricated GMI samples are shown in Figures 4-17 and 4-18. In Figure 4-17, the two different types of samples are illustrated. These devices have the following design rules:

- Meander type structures
  - 1 mm × 0.5 mm dimensions
  - Metal trace width: 10, 20, 50, and 100 μm
  - CoSiB overlap over the metal trace: 10, 20, and 30 μm
- Straight wire test structures
  - 10 mm lenght
  - Metal trace width: 10, 20, 50, 100, and 200 μm

- CoSiB overlap over the metal trace: 10, 20, 50, 100, 200, 400, and 1400 μm

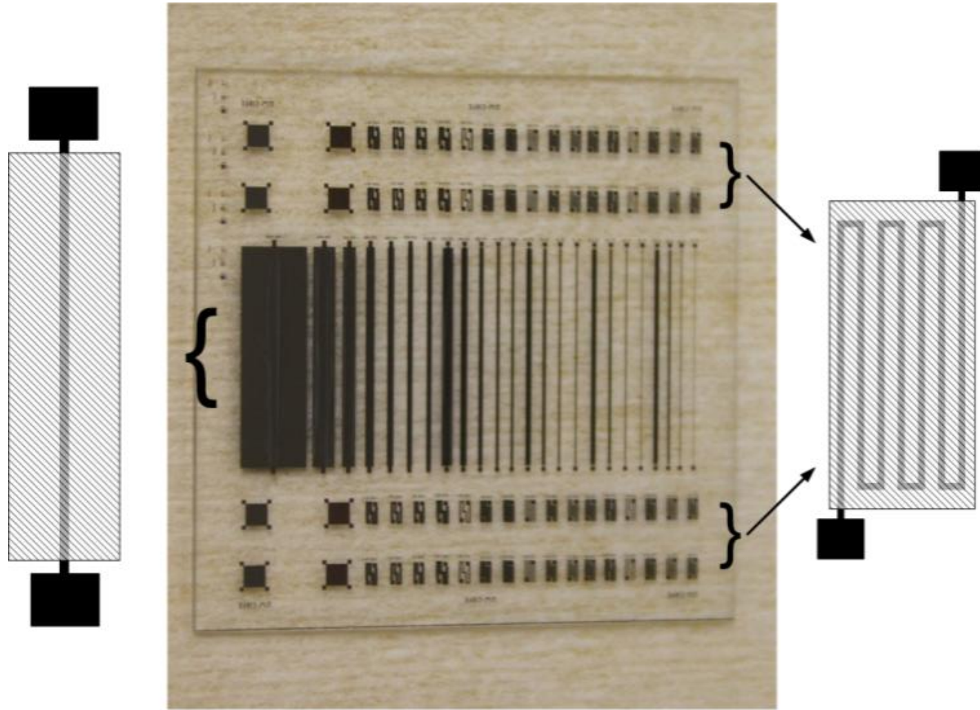

Figure 4-17 A view of one batch of fabricated sensors. Two categories of devices are shown in this figure.

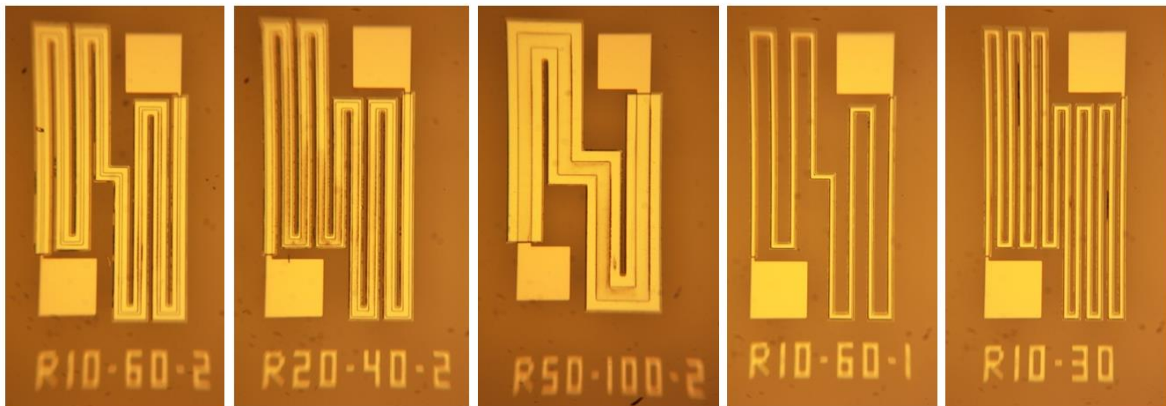

Figure 4-18 Various types of minder shape GMI sensors.

4.4.2 Test Setup and Measurement

The devices are tested using a custom-made experimental setup. An external magnetic field is exerted, employing a Helmholtz coil. The custom-made setup is fabricated with aluminum which, because it is not a magnetic material, will not affect the magnetic flux streams of coil. The other instruments employed as setup components are 4 DC probes with micro-positioners and an optical microscope. Figure 4-19 shows the setup components.

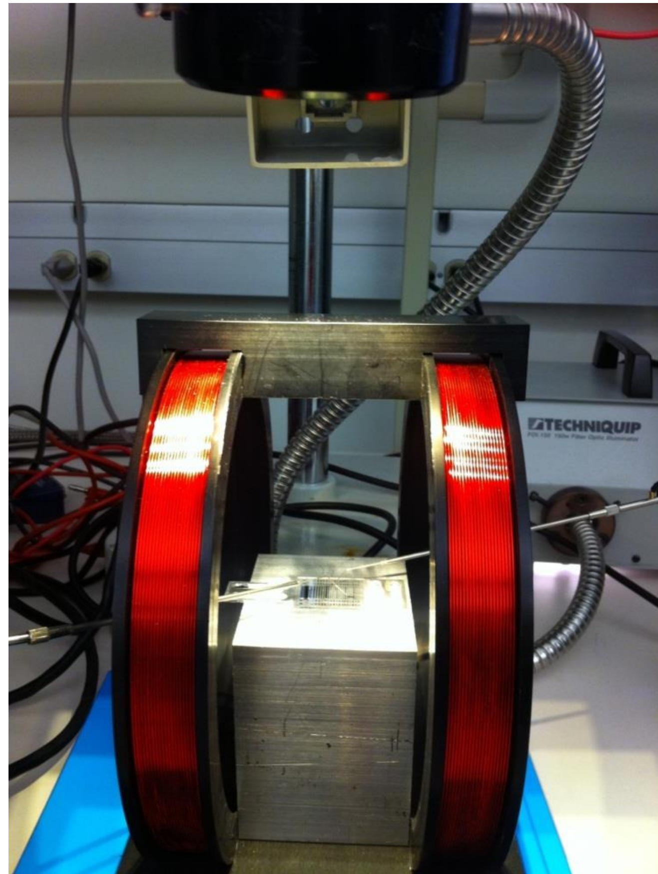

Figure 4-19 DC probes and measuring the variation of impedance under magnetic field in GMI samples.

The impedance is measured with two different methods and systems and the results are compared at the end. The first method is a 4 point probe measurement using oscilloscope and second one is using an advance precision impedance analyzer from Agilent.

4.4.2.1 Impedance measurement with Oscilloscope

The impedance measurement setup includes a function generator, an oscilloscope, and one known resistor in the order of DUTs (device under test) resistance. Figures 4-20 and 4-21 illustrate a schematic of the measurement setup and a picture of the measurement setup, respectively.

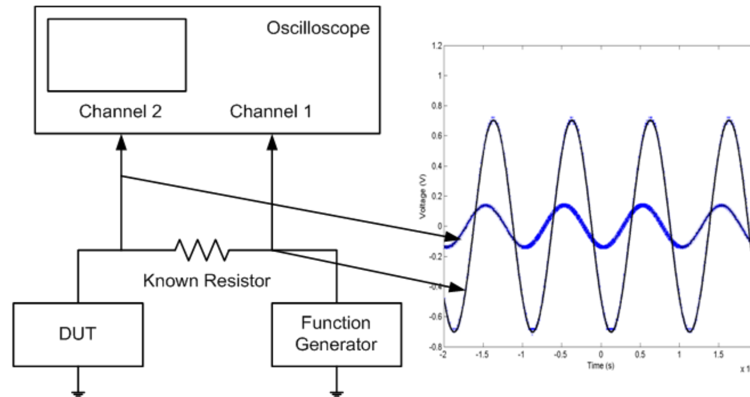

Figure 4-20 Schematic of measurement setup.

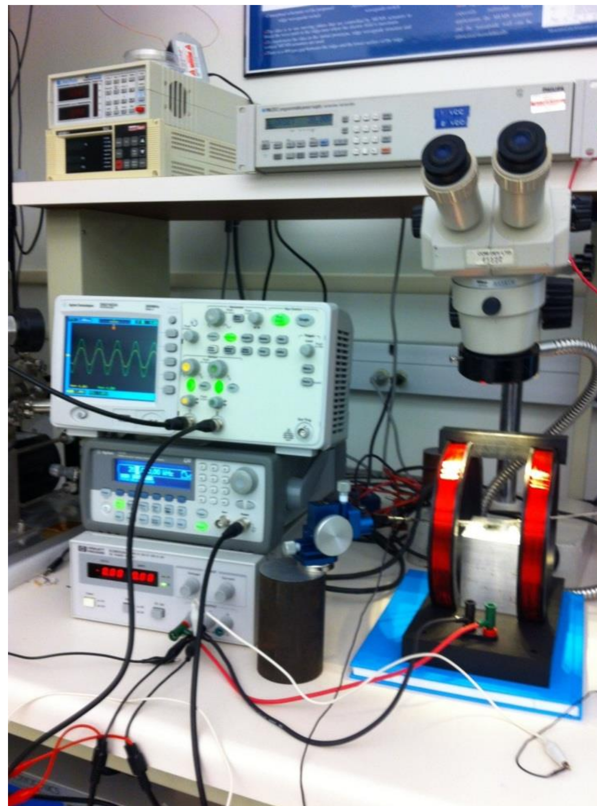

Figure 4-21 The measurement setup.

To measure the impedance of the system, a known resistor is connected in series with the DUT, and the voltage drop over the sample and the resistor is measured. (Note that the DUT and resistor currents can be calculated from the voltage drop over the resistor.) The DUT impedance is subsequently calculated from the device's voltage and current. Using this setup, V_{DUT} and V_R are captured and then processed in MATLAB to calculate the impedance and phase of the signal. The impedance of DUT is calculated using Equation (37):

$$Z_{DUT} = R\frac{V_{DUT}}{(V_1 - V_{DUT})} \tag{37}$$

4.4.2.1.1 Experimental results

Some of the samples were tested under the magnetic field and various frequencies. The results are shown in Figures 4-12 to 4-14.

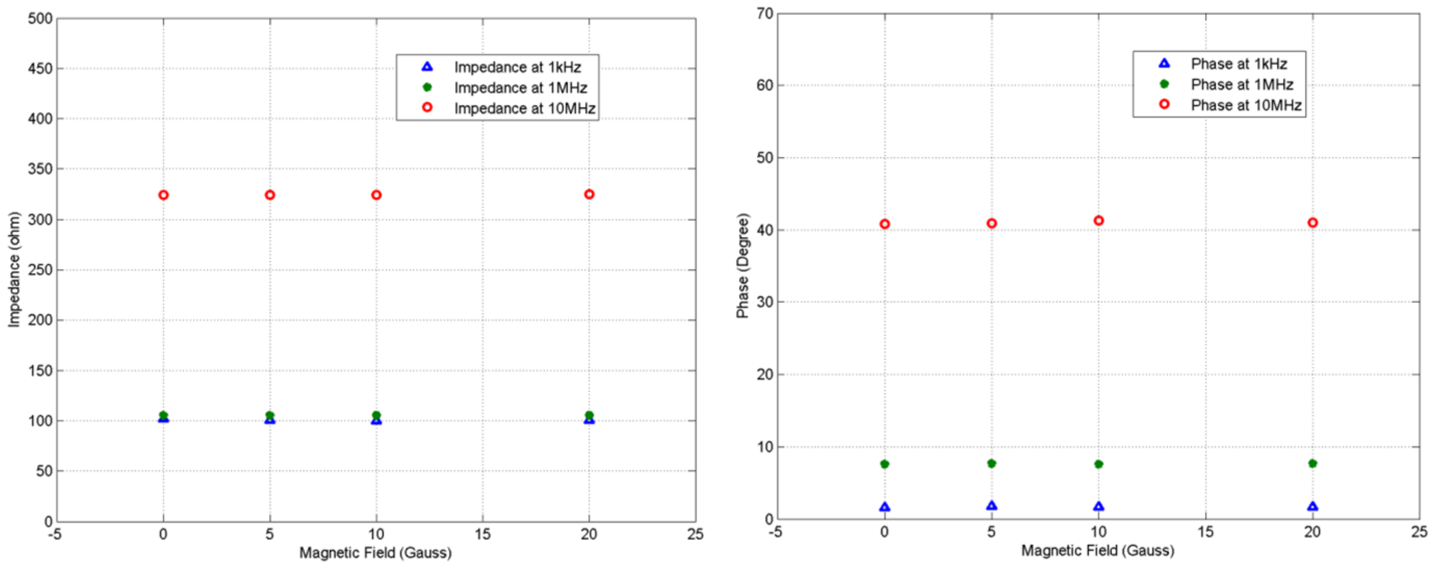

Figure 4-22 Impedance magnitude and phase of Device R10-40-1.

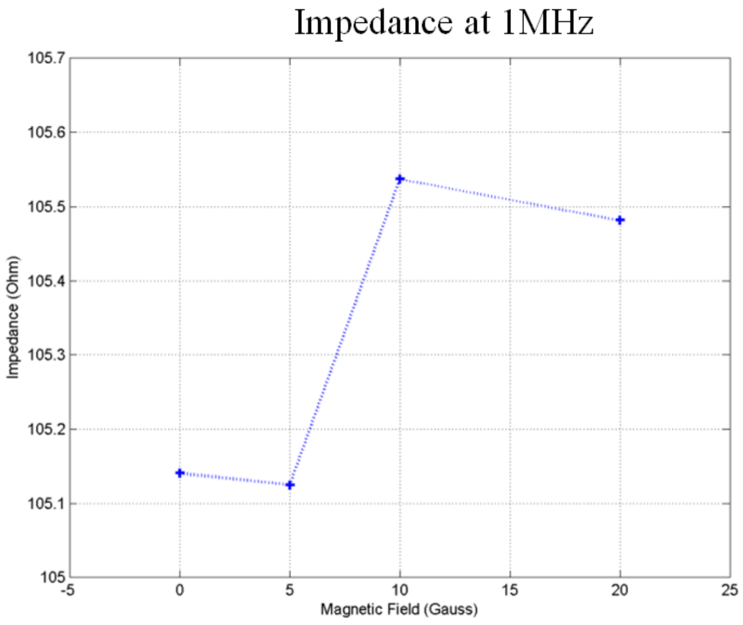

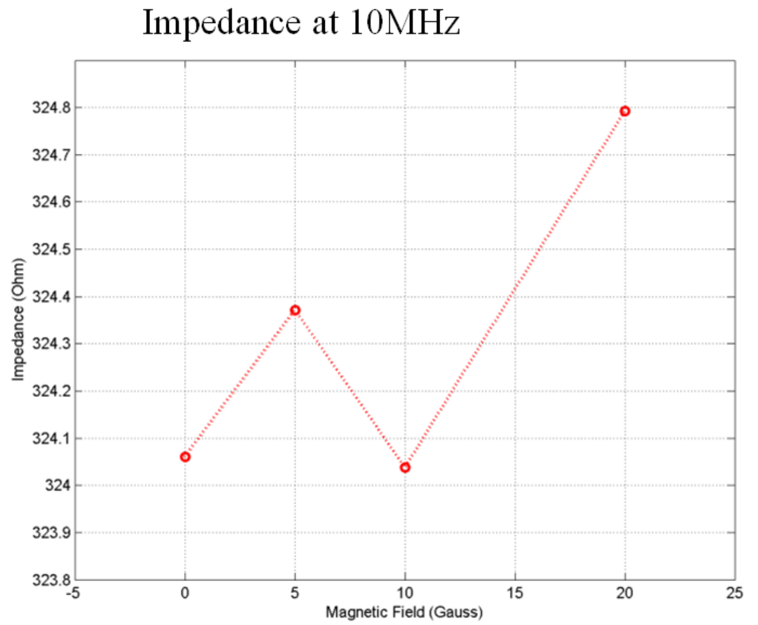

Figure 4-23 Impedance magnitude of Device R10-40-1 at1 and 10 MHz.

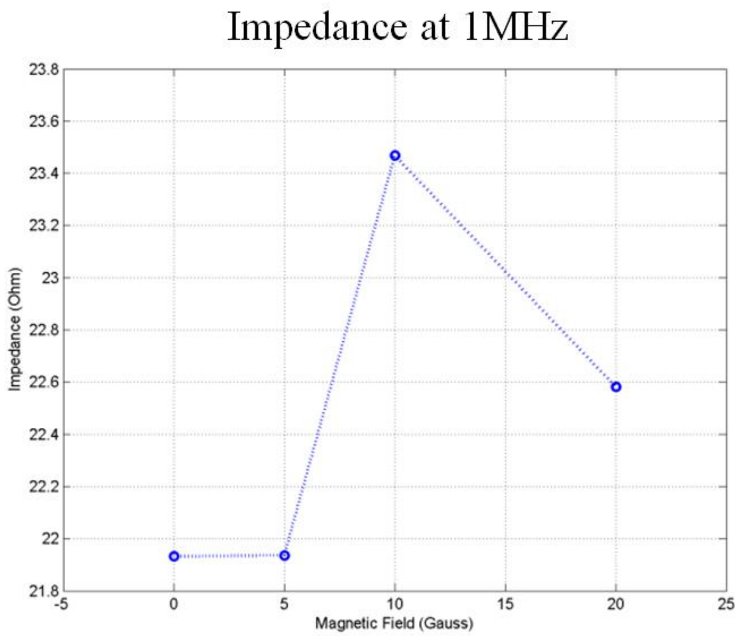

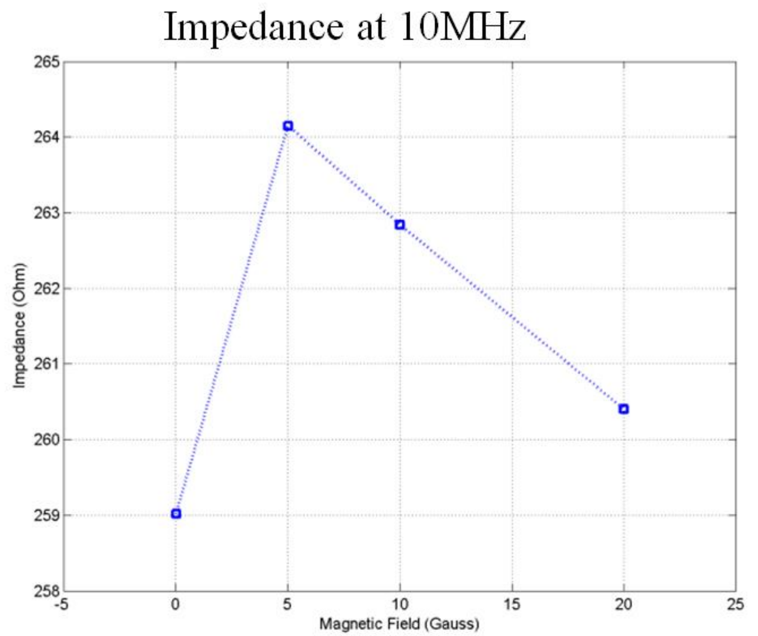

Figure 4-24 Impedance magnitude of Device 50-30 at1 and 10 MHz.

4.4.2.1.2 Discussion and Conclusion

- The measured impedance and phase of the devices increases with signal frequency due to enhanced inductance of the line.
- At f = 1 kHz, the impedance of the devices does not increase with applied magnetic field.
- When the impedance and phase are calibrated (using short and open measurements), the same trend is observed in impedance magnitude but not in the phase.
- The measured / calibrated impedance of the device at 10MHz is not valid, as after the calibration, negative impedance is achieved for the phase. This is due to the parasitic inductors of the measurement setup having higher impedances values compared to the device.

I- Slight increase of the impedance magnitude is observed at the 5-10 G external magnetic field

- The impedance change is less than 1% for R10-40-1 design at 1 MHz.
- The impedance change is less than 5% for R5030 design at 1 MHz.
- The impedance measurement may not be valid at 10 MHz due to measurement setup parasitics.

II. To find an alternative way to magnetize GMI material, we started some preliminary tests. Our preliminary test with ferromagnetic materials showed that we can make them like a permanent magnet by annealing them under magnetic field. Thus, we studied the effect of thermal and magento thermal treatment on our fabricated samples, the results of which are reported in Chapter 5. As a result of the characterization study, we ended up performing a magneto-thermal treatment on our samples. The treatment parameters time, temperature and magnetic field all have a corresponding effect on the device performance. During high temperature annealing, the magnetic domains in ferromagnetic material were expected to lose their walls and fall in line with the external exerted magnetic field. A schematic of the magnetization the occurred in the annealing step is shown in Fig 4-25. One of the main challenges here would be protecting the thin films from becoming oxidized in the hot temperatures. This challenge has been overcome by performing the annealing in nitrogen ambient. An Energy-dispersive X-ray spectroscopy (EDX) confirms the negligible oxidation after the process. Applying this process will reduce the cost and workload of the fabrication process.

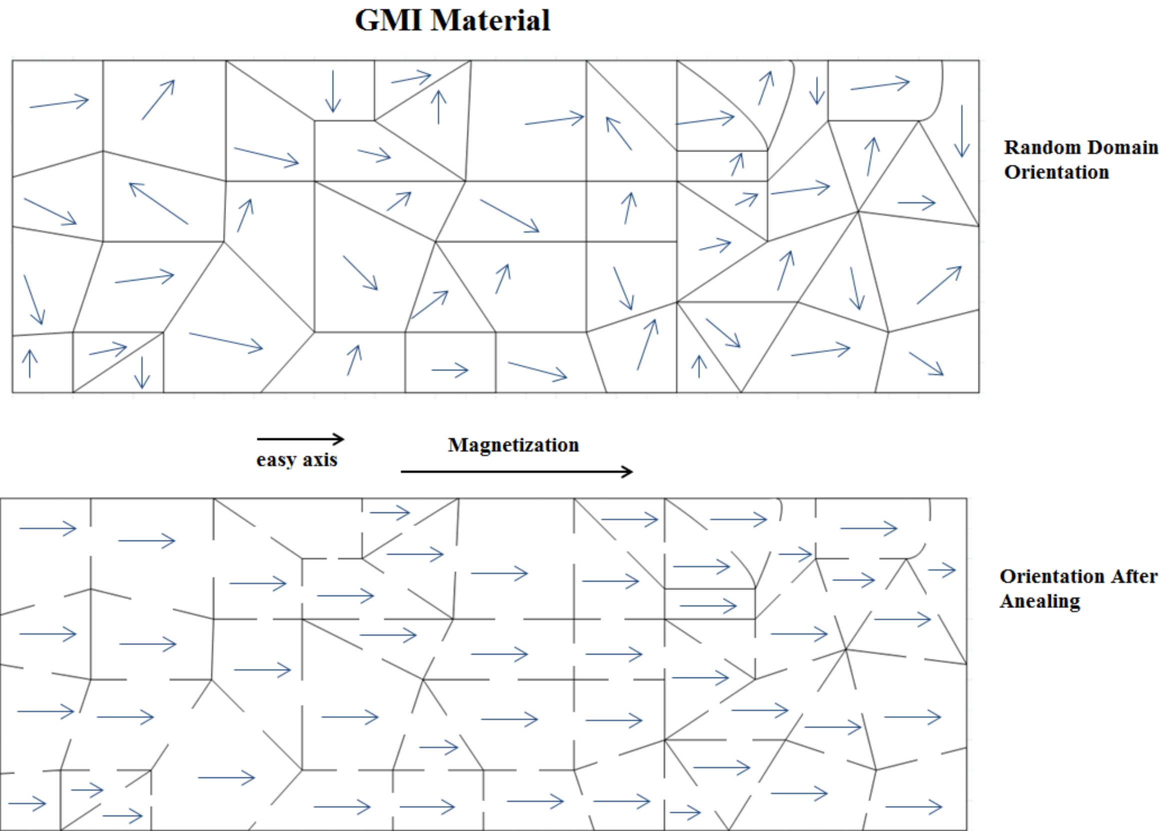

Figure 4-25 Schematic of magnetization process in magneto-thermal annealing step

The fabricated set of sensors was first annealed in a nitrogen environment furnace at 300 °C for three hours, with two 1000-G high temperature permanent magnets located under the samples. By performing the same measurement in these samples, and as reported in Figures 4-24 and 4-26, there is a marked improvement in the change of impedance. The preliminary measured results after annealing are illustrated in Figure 4-26. Here, it can be seen that the GMI R-50-30 samples at 200 kHz and 500 KHz measurement frequencies exhibit increased impedance magnitudes of 36% and 45%, respectively; in contrast, R-40-10 shows increases of only 17% and 21% at these frequencies. These data show promising improvements from the measured data before the post-processing step.

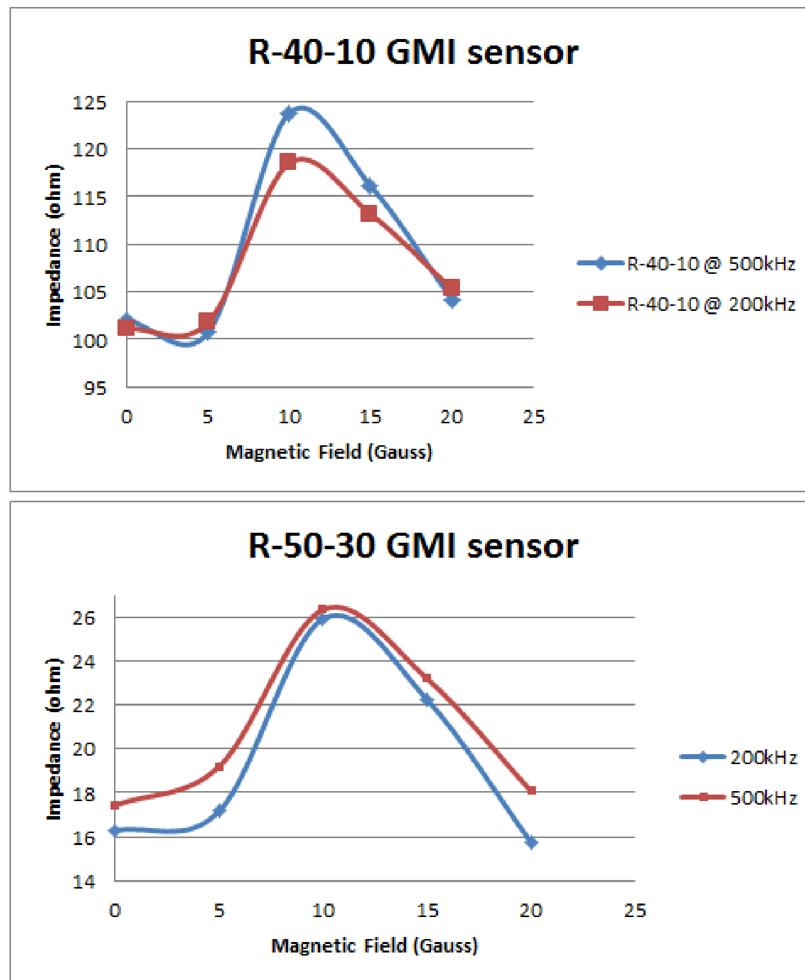

Figure 4-26 Measured impedance of two different GMI devices with different dimensions. As expected, the sensor demonstrates a substantial increase in impedance at higher excitation frequencies.

We propose developing the annealing process and optimizing its parameters for GMI magnetic sensors. The detailed study on this optimization and characterization can be found in the next chapter. The intended function of these sensors is to enable or disable a logic circuit.

The fabricated device will be mounted on a Wheatstone bridge. Exposure to a magnetic field of 10 G will cause the sensor impedance to change and the Wheatstone bridge to assume an unbalanced position. As a result of this instability, an On/Off circuit will be activated. The Wheatstone bridge and the DUT in its system are shown in Fig. 4-27. To achieve better sensing accuracy, the circuit can be

designed as unstable by default. Thus, by inserting a magnetic field when the sensor is sensing the desired amount of field, its impedance will increase and the bridge will achieve a stable condition, which will cause the current G to become zero. The reported results show a satisfying range of impedance change for the Wheatstone bridge's proper performance.

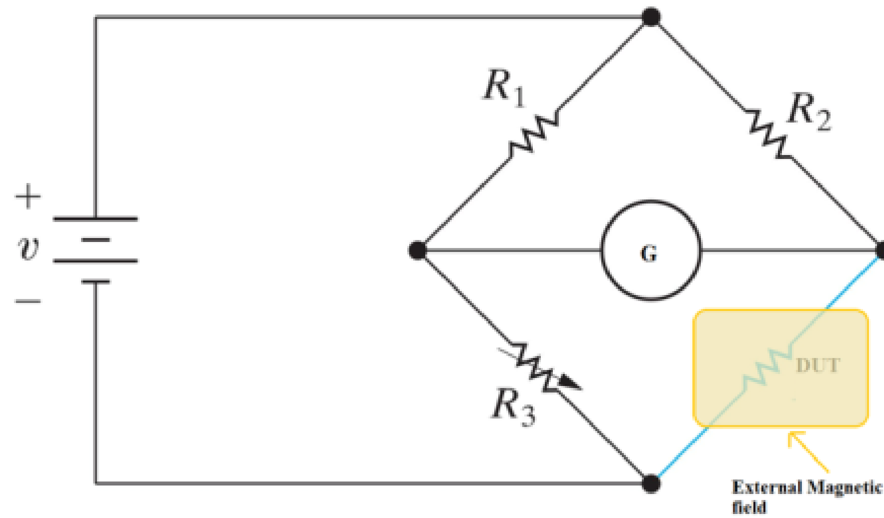

Figure 4-27 Wheatstone bridge and DUT in final sensor.

The integration will help create a 0/1 digital sensor for a narrow band of the magnetic field. The result will yield two types of sensors: one with high sensitivity, and one with low sensitivity. In a high sensitivity sensor, the bridge is normally unstable and the circuit is off; when the GMI sample reaches the desired impedance (which is a function of the magnetic field), the bridge will go to stable mode and the circuit will be on. When the device is turned on, a logic circuit will run and let us know that our exact desired field is sensed. In low sensitivity mode, the bridge will be normally stable and therefore the circuit normally on. After sensing a known amount of magnetic field and above, the impedance will change and break the stable mode. At this point, the circuit will go off and we will be notified of the existence of a measurable range of magnetic field around the sensor.

In order to ensure the quality of the measurement in this section, an Agilent precision impedance analyzer E4990A is employed. A detailed study of measurements using this device is reported in the next section.

4.4.2.2 Impedance Measurement Using Agilent Precision Impedance Analyzer E4990A

Agilent E4990A is a precision impedance analyzer with the ability to do measurements in a sweep frequency range of 20Hz to 120 MHz. This device empowered us to do the measurements in different frequencies and compare the results with the old measurements. Below, a summary of measurement results is presented.

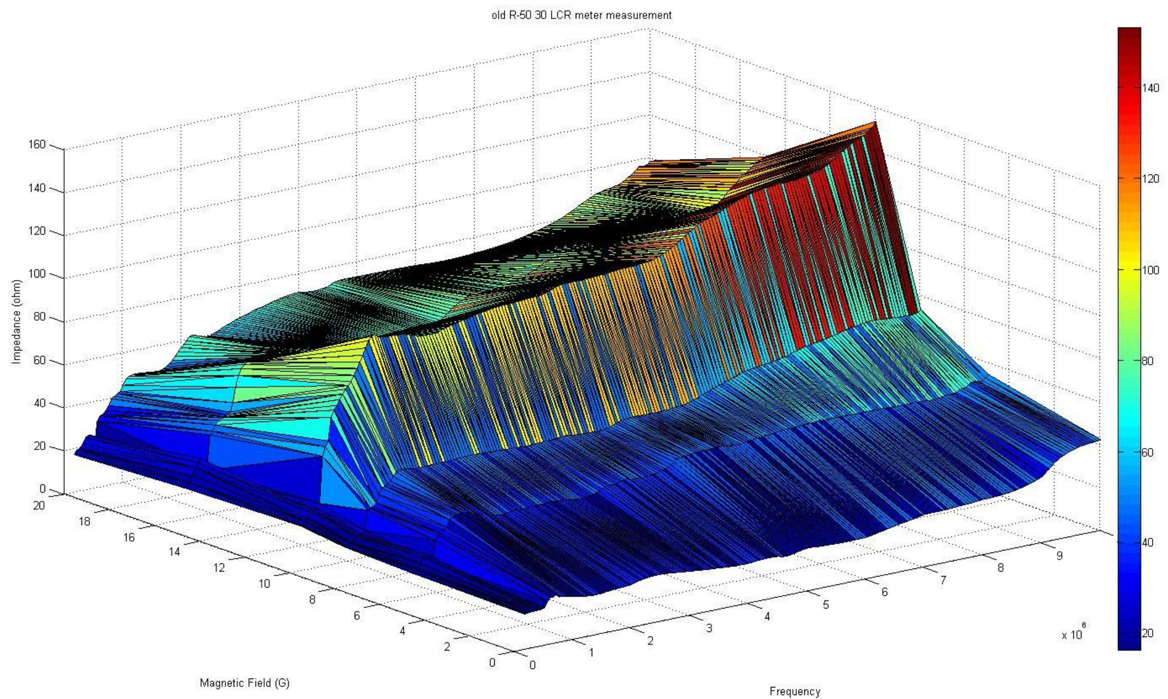

Figure 4-28 Impedance of GMI sample, R-50-30, measured in different magnetic fields in a frequency sweep of 150 Hz to 10 MHz

In order to see the effect of frequency at a constant magnetic field, one can slice the graph at the desired magnetic field. To see the impedance changes at a constant frequency, the same slicing can be done on a 3D graph at the desired frequency. Figure 4-29 shows the changes in impedance at a constant magnetic field. As shown in the figure, frequency increases result in impedance increases. It is also notable that the frequency effect on impedance has almost the same trend for different magnetic fields. From this graph, if we cross a vertical line at 500 kHz, the data from Table 4-1 can be captured.

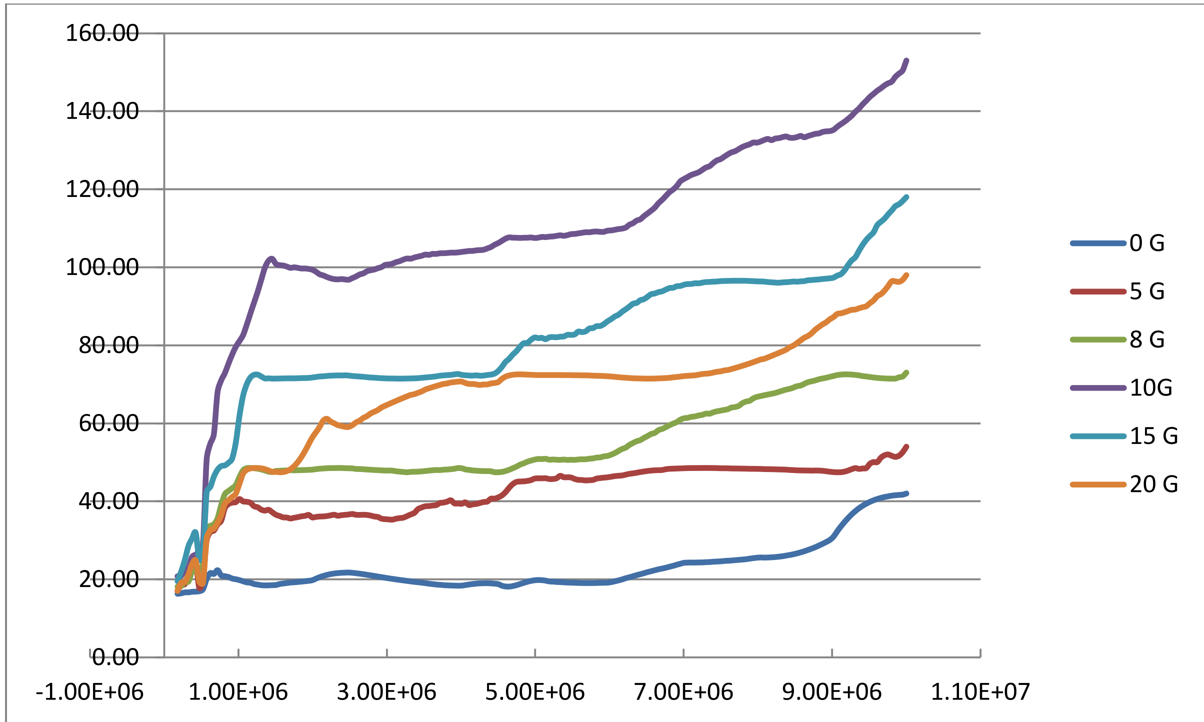

Figure 4-29 Measured impedance for R-50-30 (this is the same sample as previous section) at constant external magnetic fields over a frequency sweep

Table 4-1 Impedance Values for GMI R-50-30 at 500 kHz Measured with Agilent Impedance Analyzer

Frequency	0 G	5 G	8 G	10G	15 G	20 G
5.00E+05	16.95 ohm	17.76 ohm	22.46 ohm	27.07 ohm	24.91 ohm	19.30 ohm

It should be noted that in order to compare the measured value with the previously measured data from the other method, the same sample is tested here. Table 4-2 shows the measured value of this sample with Oscilloscope measurement. Using the data in these two tables, Figure 4-30 illustrates the impedance graph of this sample measured in each method.

Table 4-2Measured Values for GMI R-50-30 in Oscilloscope Measurement of Impedance

		R-50-30		500khz		
B	R(ohm)	V1(V)	V2(V)	V1-V2(V)	R short (ohm)t	Z (ohm)
0	20	3.6	1.98	1.62	7.75	16.69444
5	20	3.6	2.02	1.58	6.36	19.20962
10	20	3.32	2.06	1.26	6.36	26.33841
15	20	3.32	1.98	1.34	6.5	23.05224
20	20	3.6	1.98	1.62	6.44	18.00444
short condition:		2.32	0.56	1.76	6.363636	

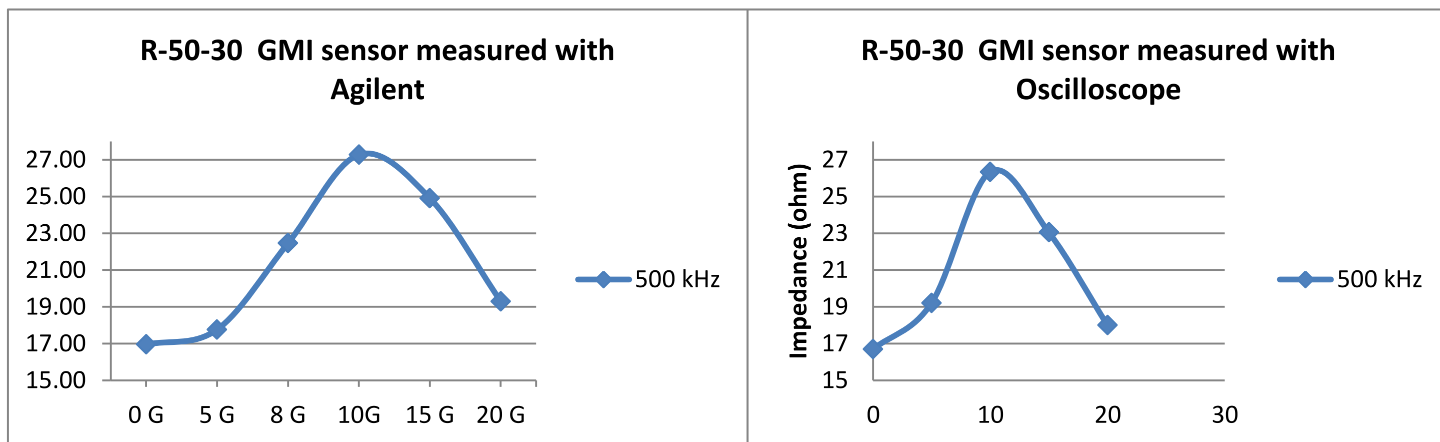

Figure 4-30 The measured impedance for GMI R-50-30 which suing both measurement methods.

along with simulation data for the same sample in the same frequency. As shown in the figure, the simulation results are in a good agreement with the measured values of the two methods.

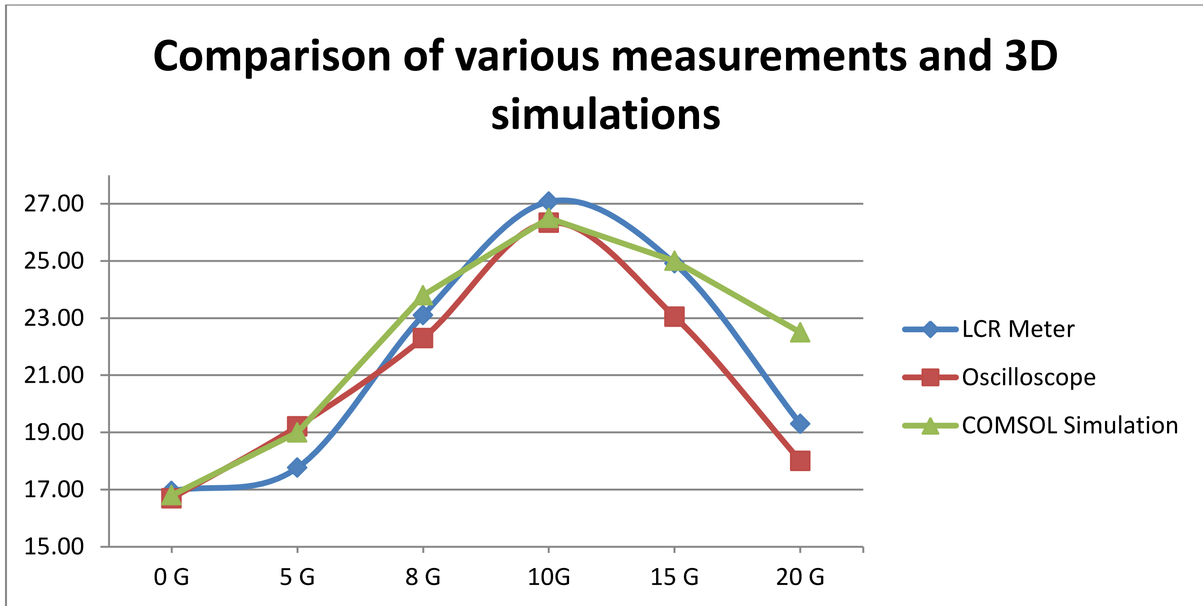

Figure 4-31 A comparison of 3D simulation for GMI R-50-30 and the measured impedances captured with Impedance analyzer (Blue) and Oscilloscope (Red)

After characterizing the post-processing (the details of which are reported in next chapter), sample R-50-30 was processed in the optimal treatment condition. This optimal processing is a magneto-thermal treatment of sample at 550°C for 3 hours in nitrogen ambient. Two ultra-high temperature permanent magnets with magnetic field of 1000 G were place under the die of sample. Figures 4-26 and 4-32 show the new measured values for the impedance of this sample.

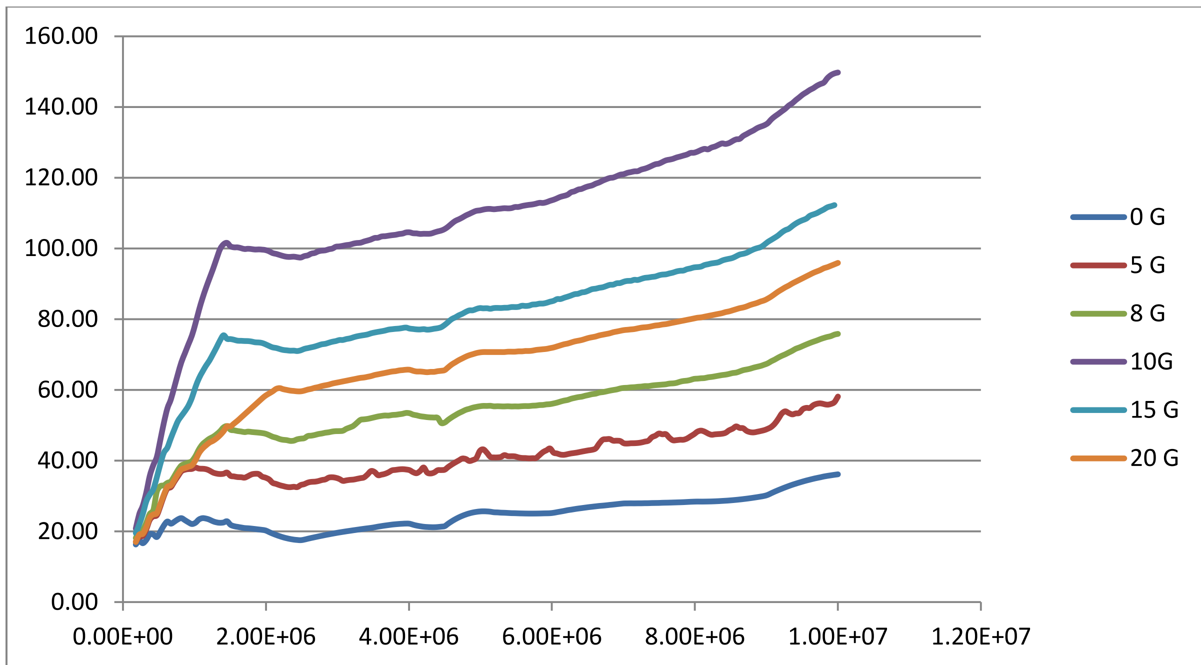

Figure 4-32 Measured impedance for R-50-30 (this sample is post process at the optimal processing condition) at constant external magnetic fields over a frequency sweep

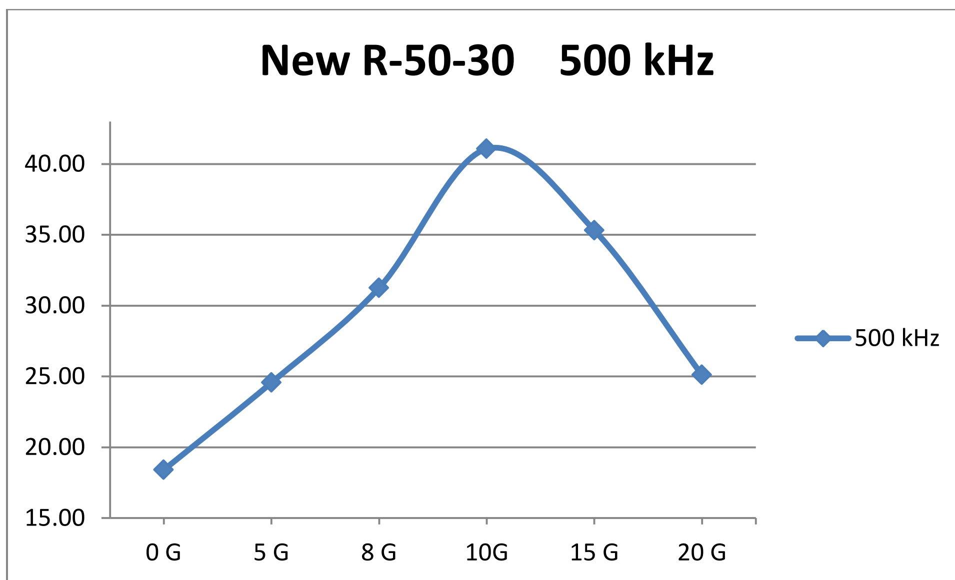

Figure 4-33 Impedance of R-50-30 sample annealed in optimized condition

Figure 4-33 shows an MI ratio of 141%. This is a tremendous improvement in impedance value of the sample with respect to the unprocessed sample and the previously processed samples. Figure 4-34 shows a comparison of measured impedance and MI ratio for R-50-30 in respect to simulations results for higher frequencies.

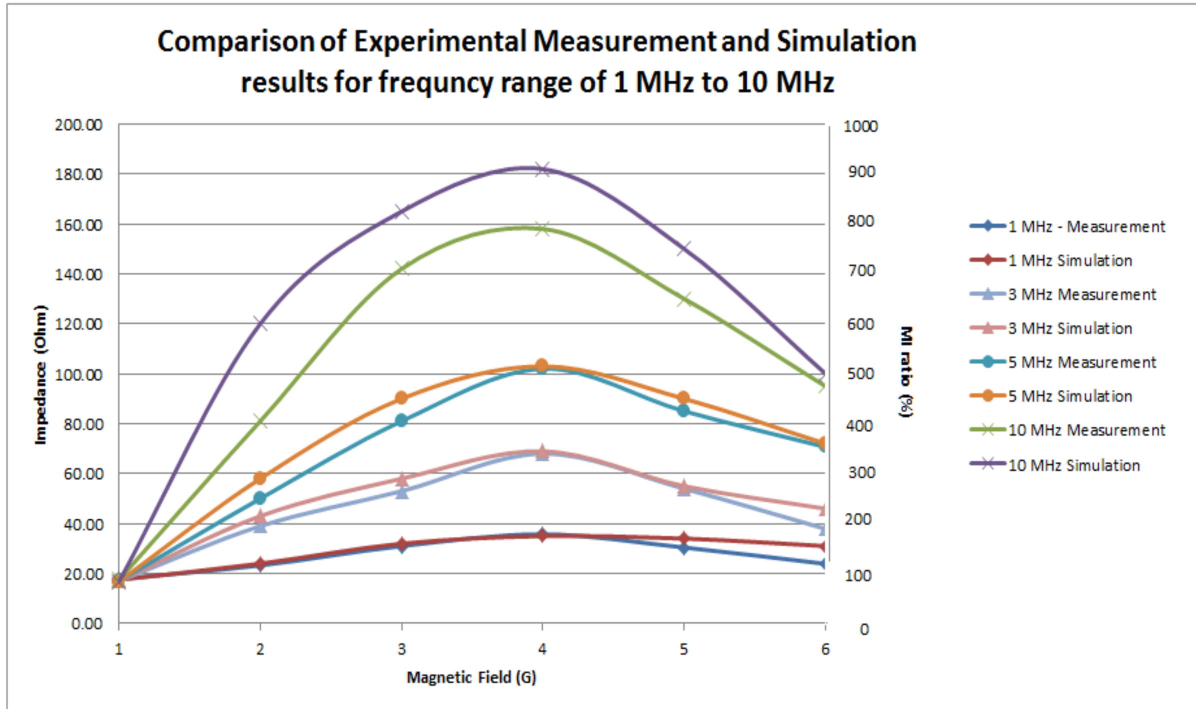

Figure 4-34 Comparison of experimental measurement and simulation results for frequency range of 1 MHz to 10 MHz.

Figure 4-35 shows the dependency of MI ratio and impedance to frequencies in higher frequencies.

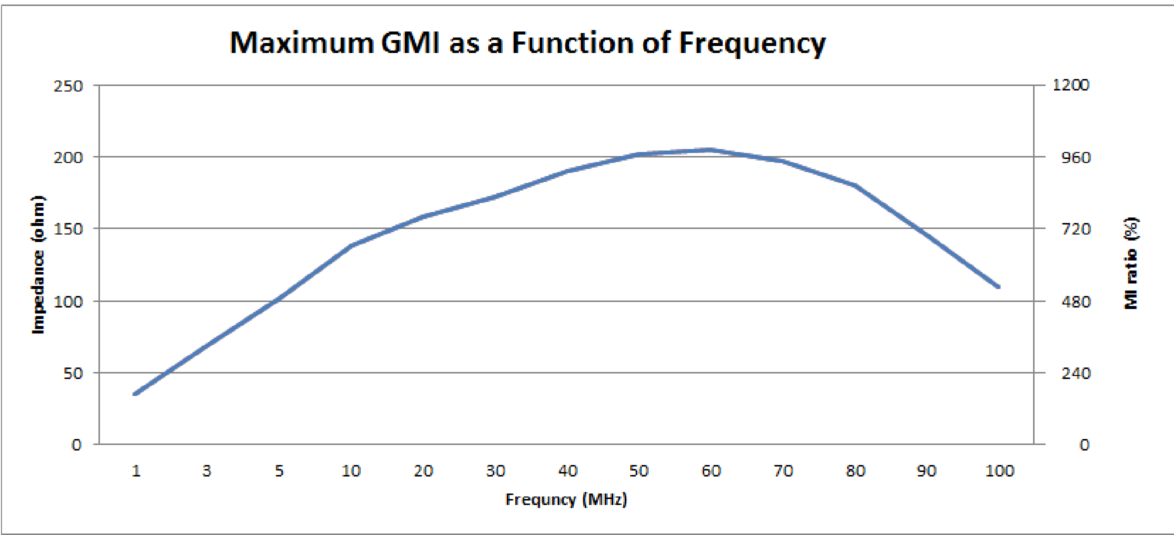

Figure 4-35 Maximum GMI as a Function of frequncy

5 Chapter Five
Characterization of GMI material- CoSiB

In this chapter, CoSiB alloy is developed to enhance the performance of multilayer thin film GMI sensors. The material is investigated for several different post-processing thermal and magneto-thermal treatments, which are categorized to study the effect of temperature, time, and the existence of an external magnetic field. The prepared samples are tested with various magnetics and material characterization tools in order to obtain a detailed understanding of the process and its effects. The post-processing shows a significant impact on the magnetic properties of the material. The causes of this impact are studied in detail. It is shown that CoSiB with enriched magnetic properties has some nano-clusters of cobalt in its amorphous matrix structure. The post-process technique can be employed to facilitate cost-effective fabrication of GMI structures in conventional micro-fabrication facilities.

5.1 Introduction

Sensor technology is one of the most attractive topics to scientists today, both in academia and in the industry [1]. Magnetic sensors are widely employed in various technological fields such as geology, aeronautics, maritime navigation, and the automobile and medical sectors [1-6]. The keen interest in developing reliable, accurate, and miniature sensors makes giant magnet-impedance (GMI) sensors an ideal solution. A giant magneto-impedance phenomenon is the change in impedance of a high-permeability material with a DC magnetic field. This occurs due to the skin effect and skin depth changes in different frequencies [5-10].

The GMI effect has been extensively studied in ferromagnetic wires and ribbons because of the main applications of sensing [6-8]. Recently, some multilayer GMI sensors that take advantage of thin film technology were introduced [3, 9-13]. Because of the dimensions of the thin films, the recent multilayered sensors have enhanced sensitivity to the skin effect and could show better results even at lower frequencies [9-12].

In a multilayer GMI structure, a conductive layer is sandwiched with layers of GMI material and will exhibit changes in the impedance upon sensing an external magnetic field. The GMI material in these structures is magnetized toward the easy axis of the device. The fabrication process of the layers and devices is a unique and highly expensive process that prevents the use of normal microfabrication machines [5, 6, and 8]. This makes them unattractive from an industry perspective.

On the other hand, beyond the study of giant magneto-resistive sensors from a materials point of view [14, 15], many studies have been carried out on the characteristics of GMI material, with the end goal of discovering an alternate (i.e., less 'exotic' and thus more cost-effective) fabrication method for these structures. In our previous work [44 and 45], we fabricated and reported on a multilayer GMI sensor with conventional microfabrication, and did a post-process procedure on devices to expose the GMI phenomenon. In this study, an extensive post-processing study has been implemented on the GMI material CoSiB, and the characterization results are reported and discussed.

5.2 Fabrication and Post-Processing

In this study, a CoSiB amorphous metallic alloy is deposited and investigated. The alloy employed in this study is Co73S12B15, but we later find that the same behavior is expected for the same family of material. The alloy has been sputtered in a DC magnetron sputtering system. Sputtering was performed in Ar plasma at a pressure of 1.5 mTorr and 600 W of DC power at a rate of 3.1 Å/s. Three-hundred nm of material was deposited on a glass wafer, after which the wafer was diced to 1 by 1 cm dies.

In order to perform a meaningful study on post-processing effects, we examined the effects of thermal treatment versus those of magneto-thermal treatment. We also studied the effects of annealing dwell time and temperature on the structure: The post-processing was carried out in two

main categories: a) thermal treatment, and b) magneto-thermal treatment. In each category, the samples are processed over two different dwell times: 3 and 4 h. Furthermore, in each category, the thermal treatments include annealed samples in 300 to 700 °C, with 100 °C increments. The annealing process was done in a clean room using a high-temperature oven with nitrogen ambient. The detailed processes of the samples are as follows:

a) thermal treatment:

In the thermal treatment, the samples are annealed in the oven with nitrogen ambient in dwell temperatures of 300, 400, 500, 600, and 700 °C. The rise time of all annealings was 1 h, and the dwell times were 3 and 4 h. The samples were then cooled to room temperature.

b) magneto-thermal treatment:

In the magneto-thermal treatment two 1000 G high-temperature permanent magnets were placed under the dice of the samples in the oven provided with the external DC magnetic field during the annealing process. With this DC magnetic field, the same thermal process as discussed in a) was implemented on a batch of samples.

5.3 Magnetic Characterizations

After the post-processing, all the samples were characterized to identify their magnetic properties. Permeability and AC susceptibility (in-phase component X' (m^3/kg)) was measured with a model KLY-2 Kappabridge, and hysteresis loops were measured with a Princeton Measurements model 3900 MicroMag vibrating sample magnetometer (VSM) using a maximum field of 1 T.

5.3.1 Permeability Measurement

The relative permeability was measured for both categories of samples, and the results are illustrated in Figures 5-1 and 5-2.

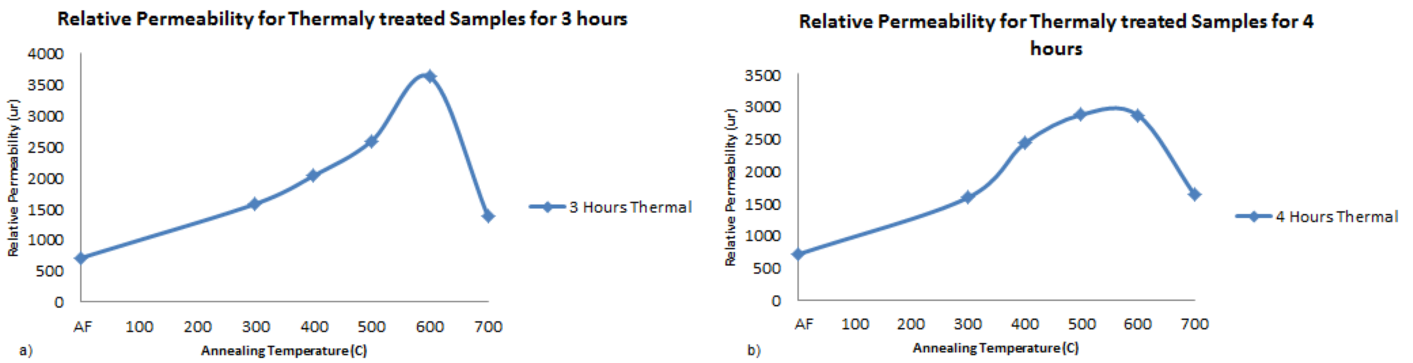

Figure 5-1 The relative permeability of samples thermally treated for 3 h; (b) the same for samples annealed for 4 h.

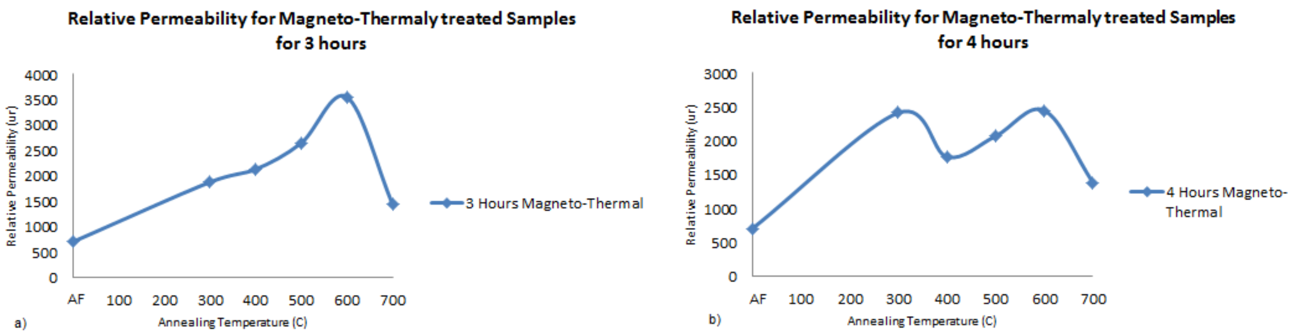

Figure 5-2 (a) The relative permeability of samples treated magneto-thermally for 3 h; (b) the same for samples annealed for 4 h.

Figures 5-1 and 5-2 confirm enhancement of the relative permeability under the thermal treatment. Based on the measurements, the existence of an external magnetic field does not have a significant effect on the permeability improvement of the alloy. It is worth noting that except for the high peaks, the measured points for the magneto-thermal samples have a higher general average of relative permeability than the thermal ones.

Moreover, the results also show a high peak of relative permeability forming around 600 °C. The high peaks of permeability for all four conditions are reported in Table 1:

Table 5-1 High Peaks of The Relative Permeability for Different Post-Processing Conditions

Type of Post-process	Dwell Time (h)	Dwell Temperature (°C)	Peak of Relative Permeability (μr)
Thermal	3	600	3615.56
Thermal	4	500	2868.37
Magneto-thermal	3	600	3551.82
Magneto-thermal	4	600	2446.96

Based on the achieved results, we can see that samples could reach a higher permeability of approximately 3500 μr in 3 h of treatment for both thermal and magneto-thermal processes. We think the local minimum captured in the relative permeability graph of 4 h of magneto-thermal processing could be an error. If the local minimum in Figure 5-2 is assumed to be a measurement error, it can be concluded that the longer annealing dwell time of 4 h leads to a broader relative permeability peak, which allows the user to achieve higher permeability in lower annealing temperatures. As shown in Figure 1, for samples treated for 3-h the recorded permeability of thermal process was 2025 μr at 400

°C, whereas it was 2425 μr for the same temperature and 4 h of annealing. Similarly, Figure 2 also shows 1876 μr for samples treated for 3 h at 300 °C, whereas the relative permeability was 2411 μr for the same temperature but 4 h of treatment. This can prove beneficial for devices with high-temperature limitations in their structures.

The reason for permeability enhancement in the alloy is the formation of nano-clusters of Co within the entire amorphous metal structure. These nano-clusters, which are discussed later in this work, have the main impact on permeability change without changing the morphology of the whole alloy.

5.3.2 Hysteresis Loop and Magnetization

Samples are measured for magnetic hysteresis loop, and the results show mass normalized values. The samples are given a nominal mass of 1 g and a nominal volume of 1 cm3 in order to ease the calculations. Hysteresis is present in ferromagnetic materials and materials with magnetization ability. As soon as a magnetic field is applied, the material becomes magnetic until all the Weiss domains of the material have the same orientation and directions. This state is the maximum magnetization of material. When the external magnetic field is removed, some materials retain a considerable amount of magnetization and remain magnetic. This is the main feature in forming a hysteresis shape [4], and thus a larger loop area represents better magnetization. The hysteresis loop and magnetization curve of the studied post-processed CoSiB are presented below:

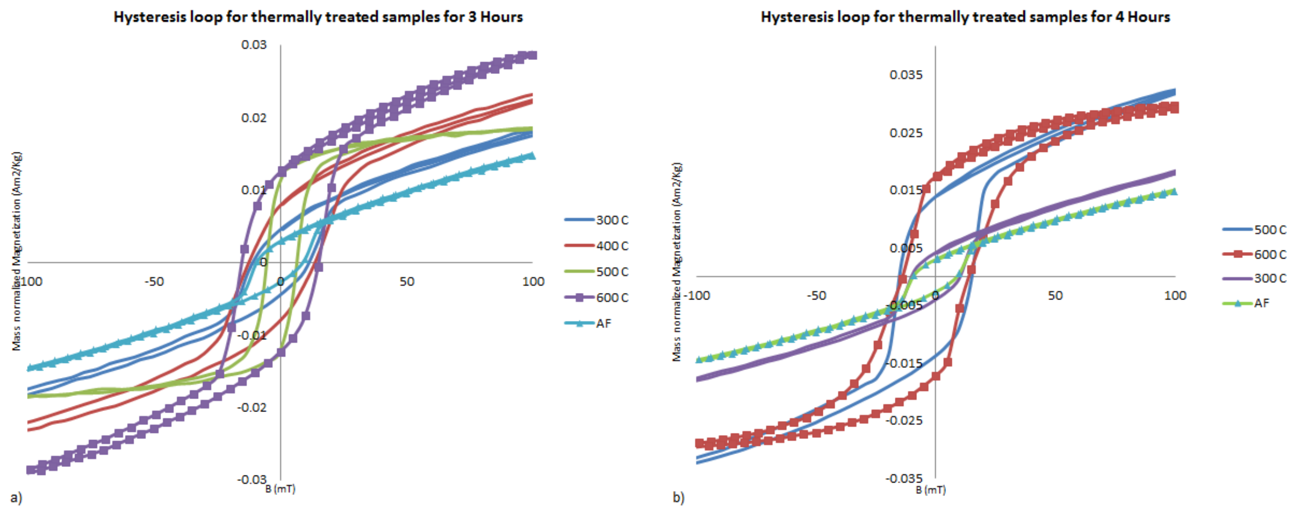

Figure 5-3 (a) The hysteresis loop of samples thermally treated for 3 h; (b) the same samples annealed for 4 h. The square marker shows the loop for the process with the highest permeability, and the triangle marker is for the after fabrication (AF) sample.

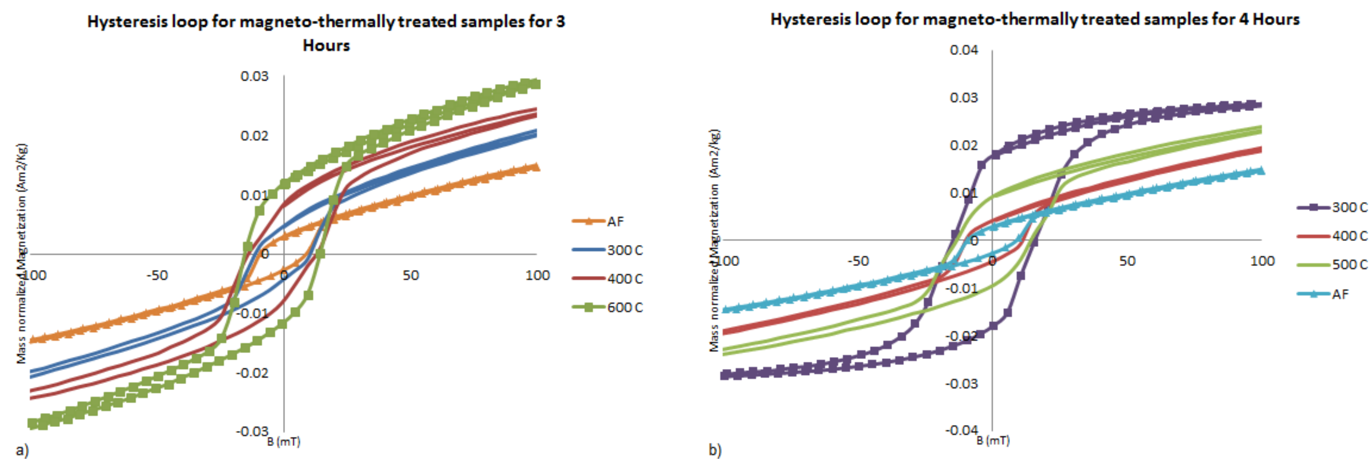

Figure 5-4 (a) The hysteresis loop of samples magneto-thermally treated for 3 h; b) the same annealed for 4 h. The square marker shows the loop for the process with the highest permeability, and the triangle marker is for the after fabrication (AF) sample.

Based on Figures 5- 3 and 5-4, the post-processing improves the magnetizability of the GMI material. The higher magnetizability leads to better magnetization of the GMI layer in a multilayer sensor, which is done by a magneto-thermal process.

5.3.3 Magnetization of CoSiB Layer in a layered structure

After the magnetic properties of the GMI material are improved, the material should be magnetized in order to show the GMI phenomenon and be employed in a multilayer GMI structure. As demonstrated in section III-b, the material has a high potential of magnetization in some known post-processes conditions. A magneto-thermal treatment in specified temperature and time will result in breaking the Weiss domains' walls. Upon losing the magnetic walls, the magnetic domains of material will align in the direction of the exerted magnetic field. This process bypasses the need for a special and expensive sputtering system for GMI material fabrication. Figure 5-5 shows a schematic of this process.

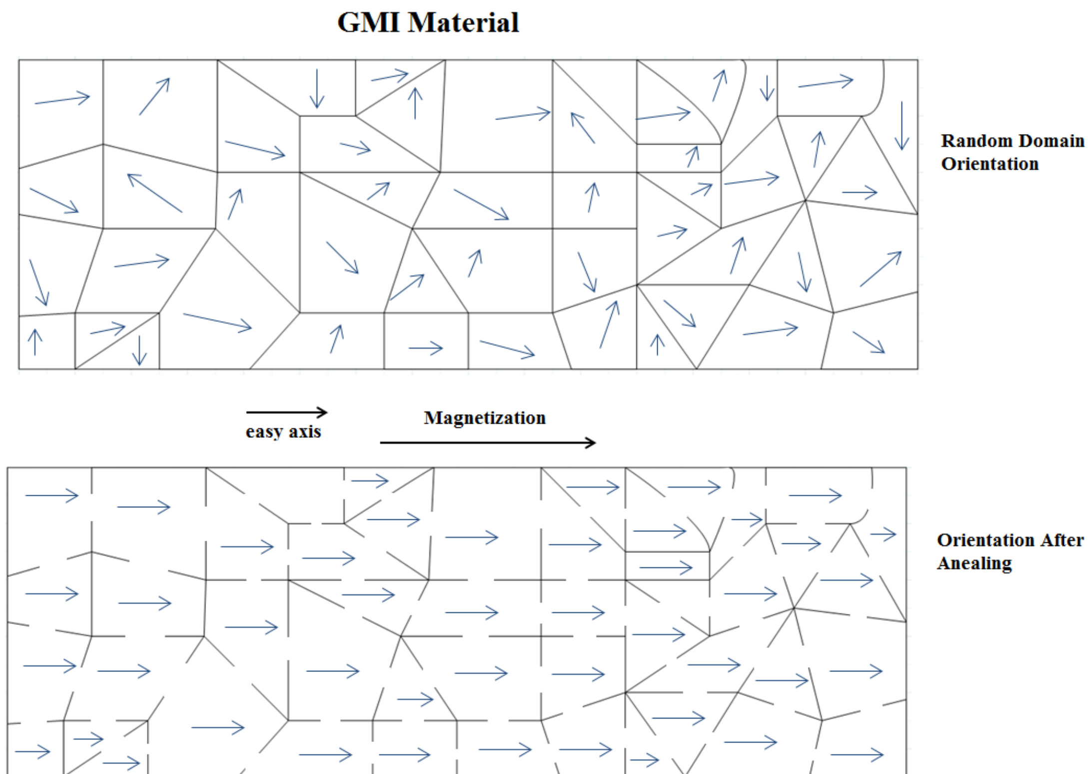

Figure 5-5 Schematic of annealing magnetization under a magneto-thermal post-process. It is shown how the Weiss walls are breaking up and letting the domains be aligned to the external field.

5.4 Material Characterizations

For material characterization, the material is tested using Raman spectroscopy, X-ray diffraction, and energy dispersive X-ray spectroscopy. In the following sections, measurements for each test are illustrated.

5.4.1 Raman Spectroscopy

A Raman test is done on the CoSiB before and after the annealing step to see whether or not the crystallization of material changes during this step. The narrowing and increasing in the intensity of

the Raman band, as well as the shifting in the bands to higher wave numbers, can be attributed to an increase in particle size and improved crystallinity. The Raman test is implemented using Raman spectroscopy and a microscopy machine, Bruker Senterra Confocal Microscope (with 532 and 785 nm lasers). The result of Raman spectroscopy supports the preliminary expectations for higher crystallinity after the treatment. It also shows high quality small-sized crystals of Co in the spectrum. Figures 5-6 and 5-7 give the Raman spectroscopy results for thermal and magneto-thermal samples.

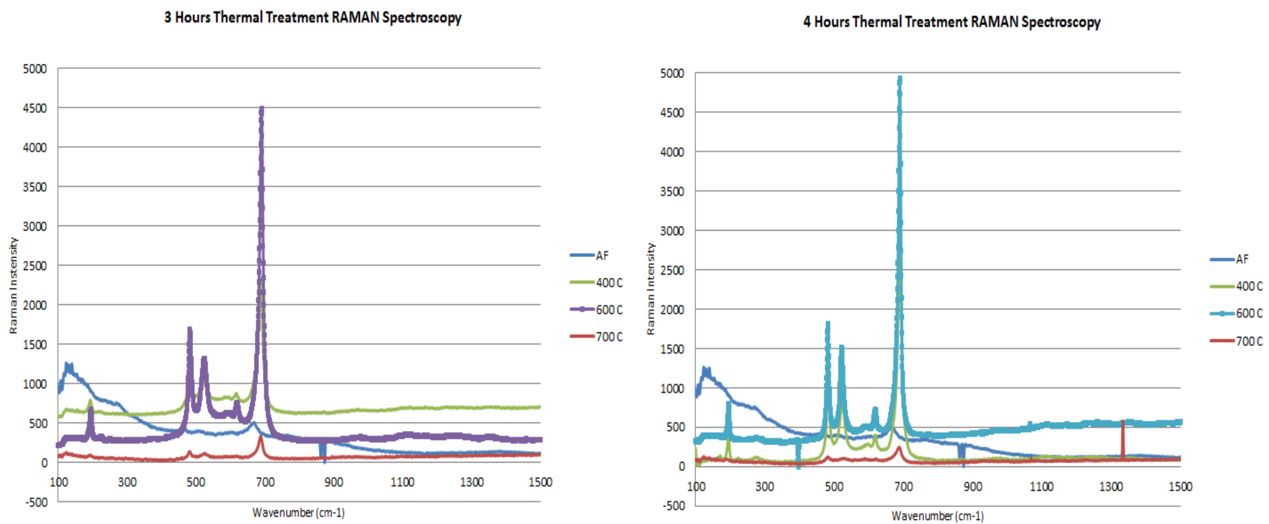

Figure 5-6 Raman spectroscopy for thermal post-processed samples.

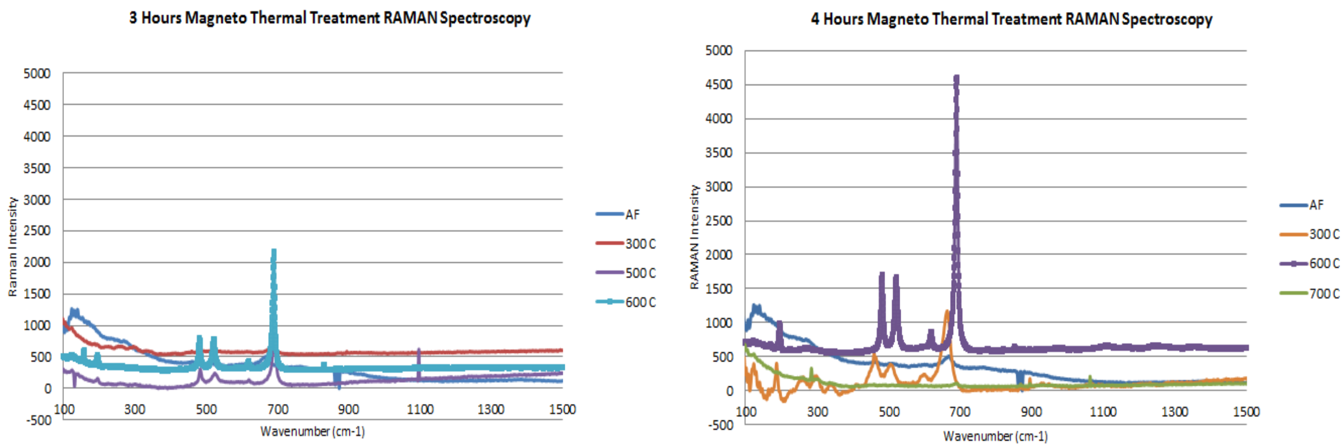

Figure 5-7 Raman spectroscopy for magneto-thermal post-processed samples.

In Figures 5-6 and 5-7, the condition which had the highest permeability is bolded in the graphs. It is interesting to note that the condition corresponding to the highest permeability has higher intensity and better quality peaks in the Raman spectroscopy results as well, which confirms the formation of nano-crystals in the entire metallic glass structure of CoSiB. Another interesting fact in the Raman test is that the treatment of samples at higher temperatures makes a better quality of nano-crystallines until the highest permeability point, after which the crystals lose their quality and vanish. This is due to the probable formation of equilibrium phases of material at temperatures higher than 650 °C. Among those phases, it is probable that boride phases such as Co3B and Co2B will be formed. Boride phases normally decrease the relative permeability of materials [4, 16]. Figures 5-1 and 5-2 verify the assumption of boride formation in temperatures above 650 °C, as they confirm the decreasing of permeability at this temperature.

5.4.2 X-Ray Diffraction

X-ray diffraction (XRD) is done on samples using a bruker d8 advance X-Ray diffractometer system with the capability of testing thin films. The XRD parameters for the experiment are reported in Table 5-2.

Table 5-2 X-Ray Diffractometer Parameters

Parameter	Value
Current intensity of X-ray tube	40 mA
Voltage of X-ray tube	40 kV
Beam wavelength	0.154 nm
Time of counting in one measurement point	5 s
Step between measurement points	0.05 °θ
Range of scan	20-80 °θ

Figures 5-8 and 5-9 illustrate the XRD measurement for thermally treated and magneto-thermally treated samples, respectively.

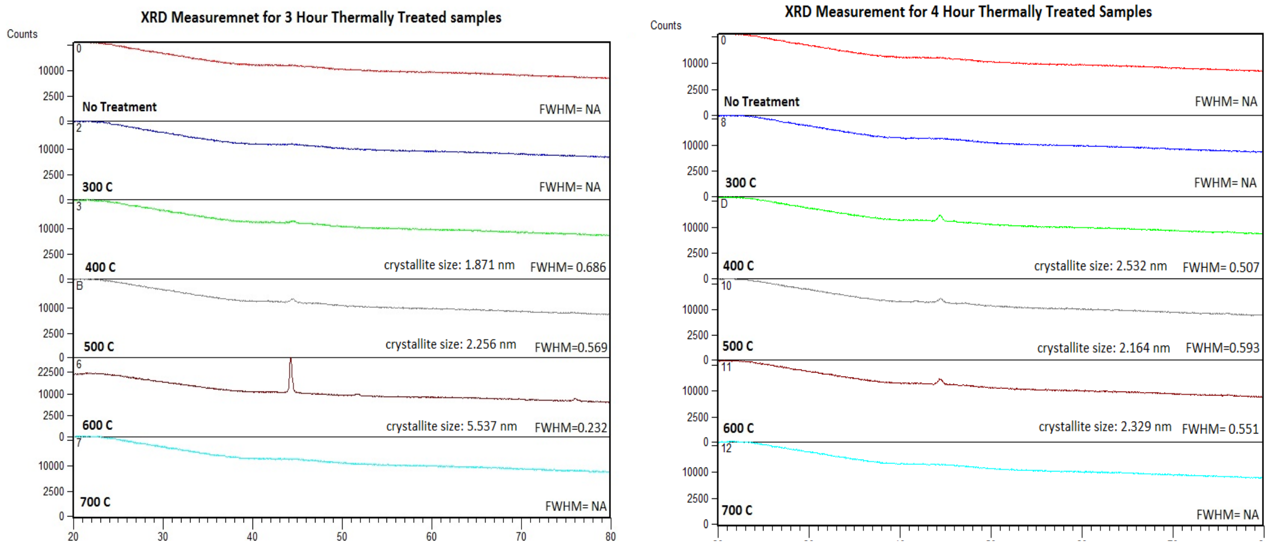

Figure 5-8 XRD graphs of samples thermally treated for 3 and 4 h.

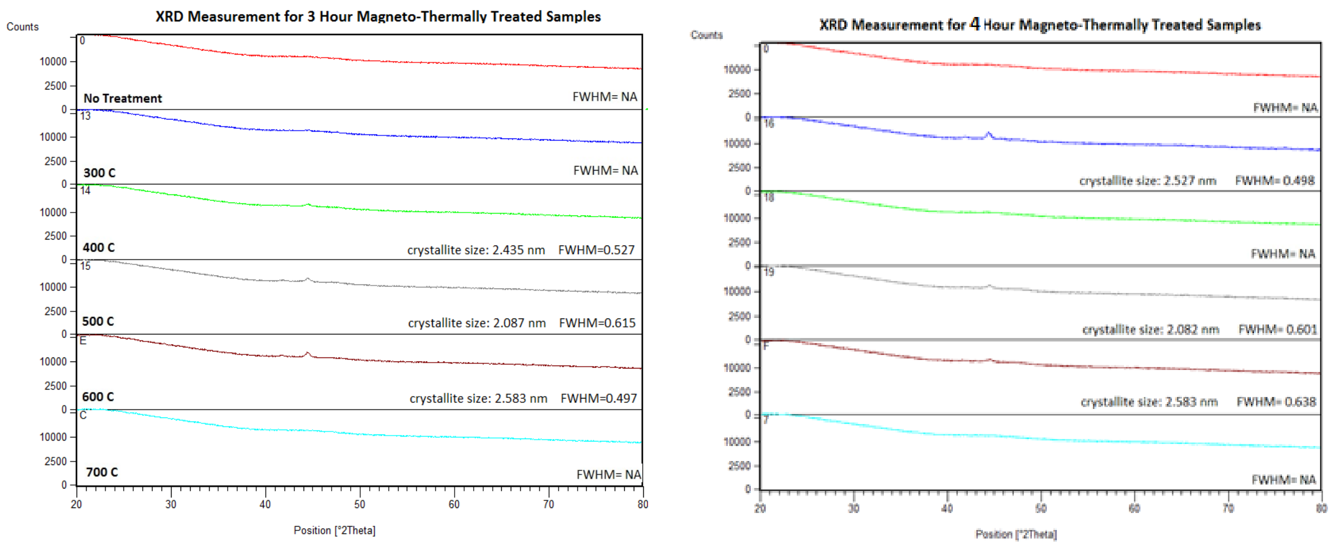

Figure 5-9 XRD graph of samples magneto-thermally treated for 3 and 4 h.

In Figures 5-8 and 5-9, some peaks can be detected in specified angles. Checking these peaks with X'Pert Highscore Plus software (provided with the XRD diffractometer) and comparing the peaks with those found in other research reports reveals that they are all showing α-Co crystalline. The fact that only Co crystalline is detected in XRD supports the idea of the formation of Co nano-clusters in the matrix of an amorphous metallic alloy. Normally in an XRD graph, a higher intensity of baseline is related to a higher quality of amorphous structure. As is shown in Figure 5-8 and 5-9, the baselines of captured streams have high intensity values; even the stream with the crystalline shows a general amorphous structure. For the above data, and using the Scherrer method [17] in the software, the crystallite size of the Co nano-clusters is calculated at around 2.5 nm. In this method, the size is calculated using the Scherrer equation, which relates the size of a crystallite to the beam wavelength, peak angle, and full width at half maximum (FWHM) of the peak [17].

5.4.3 Energy Dispersive X-Ray Spectroscopy

In order to determine the elemental composition of specimens and ensure that the samples have the same alloy ratio as the sputtering target, energy dispersive X-ray spectroscopy (EDX) is performed on samples. The measurement is done using a TEAM EDS analysis system for SEM. EDX measurements for all of the samples are the same, and the same results are captured. The results indicate that annealing does not change the alloy structure and that no external chemical reaction occurs in the main material. Figure 5-10 shows the EDX of a sample thermally treated for 3 h at 600 °C.

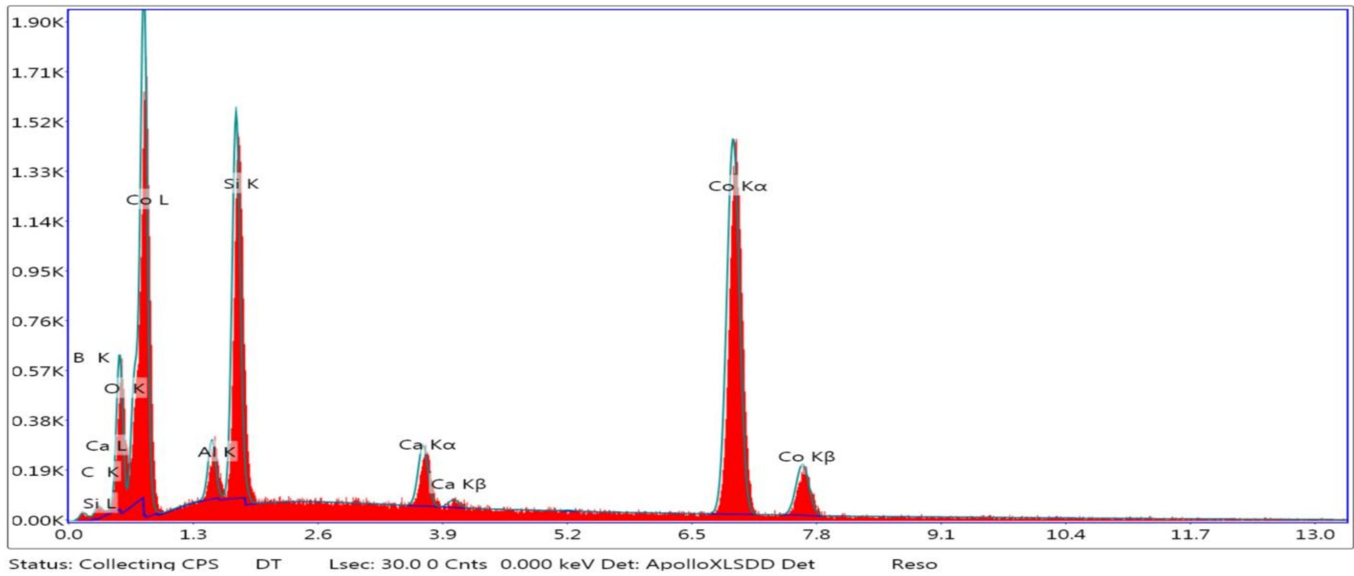

Figure 5-10 EDX graph of a sample magneto-thermally treated for 3 h at 600 °C. It should be noted the same graph is captured for all other samples.

Table 5-3 shows the quantitative measured values for this experiment.

Table 5-3 EDX Captured Quantitative Results. The Main Elements are Highlighted

Element	Weight%	Atomic%
B K	11.31	20.99
C K	1.69	2.01
O K	2.44	3.14
Co L	72.85	57.52
Si K	10.28	12.98
Al K	0.6	0.72
Ca K	0.83	2.64

As can be observed from Table 5-3, the main captured elements are Co, Si and B, with almost the same weight distribution in the alloy as the source of the sputtering. Some other elements with

negligible amounts are also detectable, but these correspond to sample contamination and test environment.

5.5 Results and Discussion

Based on the achieved results for the various magnetic and material characterization tests, it can be concluded that CoSiB GMI material keeps its elemental composition and amorphous shape in post-processing treatments. Furthermore, the results show that some nano-crystallines of Co formed in the amorphous matrix of material. These nano-crystals are congregated together as nano-clusters of Co in the matrix. The formation of Co nano-clusters is the main reason for permeability enhancement in the material. Experiments also indicate the critical temperature at which the highest permeability can be reached. A detailed study of the material properties of the CoSiB confirms the formation of small nano-crystallines of α-Co in the structure.

Moreover, the tests show that the high level of background baseline in XRD measurements confirms the morphology of the material as metallic glass. According to the Raman spectroscopy of the material, the quality of nano-crystals decreases after a critical temperature is reached. This occurs due to the formation of equilibrium phases of material in the alloy, e.g., boride phases. The probable boride phases have a reverse influence on magnetic enhancement, which results in a decrease in permeability. This reduction in permeability can be verified in Figures 5-1 and 5-2 for samples treated at 700 °C.

When viewing this research work, a misconception may arise regarding the source of enhancing magnetic properties of CoSiB. Specifically, it might be assumed that thermal treatment is the sole significant process in enhancing CoSiB's magnetic properties and that a magneto-thermal process will have exactly the same effect, but this would be an inaccurate assumption. To resolve this misconception, note that in order to be able to use CoSiB as a GMI material, especially for a

multilayer structure, the material not only should have high permeability but also must be magnetized. A magneto-thermal post-process leads to both of these properties. At a high temperature, after removing the magnetic domain walls, the domains are all magnetized in the direction of the external magnetic field and cool down in the same magnetic environment, ensuring layer magnetization by the end of process.

In previous publications [3, 10], the authors reported fabrication and testing of multilayer GMI sensors with a magneto-thermal post-process. The reported sensors indicate an impedance increase of 16.69 to 26.33 Ω, and 102 to 123.75 Ω for two different sensors. Since different elemental ratios of CoSiB can be employed as GMI material with the same material morphology and behavior, the above conclusions and qualitative patterns are valid for all CoSiB amorphous metallic alloys.

.

5.6 Experimental Tests on Tri-Layer Thin Film GMI Sensors

A batch of tri-layer thin film GMI sensors is fabricated using the same fabrication recipe. The sensors consist of CoSiB(400nm)/Au(200 nm)/CoSiB(400 nm). The schematic of the fabrication steps and an optical image of the batch of sensors are illustrated in Figure 5-11. Details of the fabrication of these sensors can be found in the authors' previous works [9 and 10].

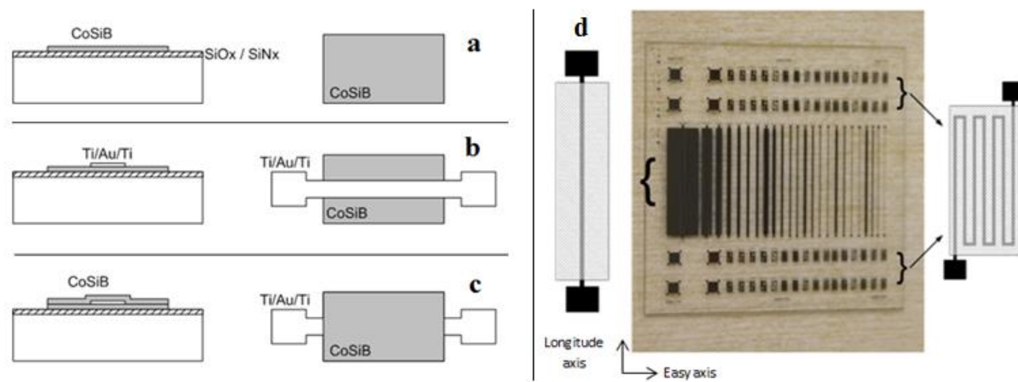

Figure 5-11 GMI thin film samples fabrication process flow a) sputtering and patterning of CoSiB b) Deposition and patterning of Metal trace layer c) sputtering and patterning of CoSiB d) A 1-inch to 1-inch die of glass wafer, containing the thin film GMI samples.

The devices are tested using a custom-made experimental setup and employing Agilent E4990 precision impedance analyzer. Using a Helmholz coil [19], an external magnetic field is exerted on the samples. The sample stage is made of aluminum that is not a magnetic material and will not affect the magnetic flux streams of coil. The test results of one of the samples R-50-30 is reported below. In this sample, the width of CoSiB layer is 50 µm and the width of the Au layer is 30 µm. Three R-50-30 are tested in 3 different phases: immediately after fabrication; after 300°C magneto-thermal after 600°C magneto-thermal treatment and 500 kHz of AC current. The results are shown in Figure 5-12.

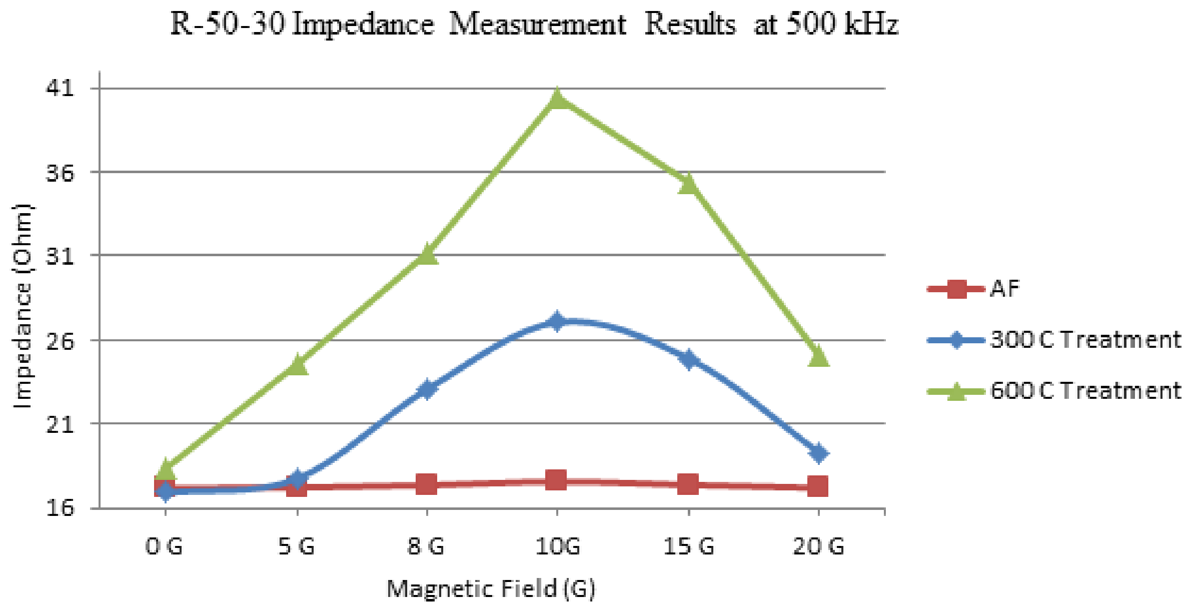

Figure 5-12 Measurement results of GMI R-50-30 in 500 kHz ac current.

As illustrated above, the magneto thermal treatment has drastically increased the impedance change in the tested thin film GMI sensor.

6 Chapter Six
Conclusions and Future Plans

The main focus of this work was realising miniature magnetic sensors. Miniaturizing sensors makes it easier to integrate them with conventional industrial systems and also makes them useful for biomedical applications. Due to high industrial demand for digital 0/1 magnetic sensors in the millitesla range (also known as low field intensities), the goal spec of the sensors was set to this working range. This magnetic field is not harmful to the human body and is in the range of fields generated by biomedical devices. A main application of these devices is hearing aids. Typically when using hearing aid devices, the user cannot speak on a phone or cellphone because a beeping noise occurs in their ears. This problem arises from the conflict between the magnetic field in the hearing aid and that in the speaker. In these cases, cutting one of the fields will resolve the problem. By integrating a miniature magnetic sensor, the hearing aid's magnetic field will be cut when it senses a threshold field of noise generation.

After conducting a broad literature review on the recent advancements of magnetic sensors, we chose two different types of sensors which we deemed well-suited to the scope of the research:

1- MEMS reed sensors
2- Giant Magneto Impendence (GMI) sensors

As reported in the thesis, both of these sensor types were studied in detail, and a miniature version of them was successfully fabricated and tested. Contributions

1- Development of tri-layer MEMS Reed sensors:

A tri-layer MEMS reed sensor was designed, fabricated and tested in this thesis. The multilayer beams were comprised of a Ni layer (3 µm bottom electrode, and 1 µm bottom electrode) sandwiched between two gold layers (75 nm each). These sensors were studied and designed in COMSOL Multiphysics, and were simulated in detail. Using the simulation results, the general working map of these sensors was investigated and presented. The achieved sensors of this study were fabricated using microfabrication technology. The full sensor size was around 300 µm * 100 µm, which is the smallest fabricated MEMS reed sensor so far. The previously reported smallest MEMS reed sensor was 1 mm * 1 mm, which is larger than our sensor by a factor of 10. The final fabricated sensors are normally open switches that provide a 30 ohm contact upon actuation.

.

2- Development of multilayer Giant Magento-impedance thin film sensors:

In addition, this study presented the design and microfabrication of multilayer GMI thin film sensors. The GMI multilayer is comprised of an Au layer (200 nm) sandwiched between two magnetic layers (400 nm). GMI materials need an expensive sputtering system, which provides a magnetic field during their deposition. A new post-processing treatment was investigated and tested that enabled the fabrication of these materials using conventional microfabrication facilities. Moreover, a complete 3D COMSOL simulation of GMI phenomena for multilayer thin film structures was presented. This simulation was among the frontier efforts for simulating sensors using FEM simulation software. Devices were designed based on the simulation results, and these were tested with two different measurement methods. All of the captured results from the simulations and measurements were in the acceptable range and verified each other. The GMI thin film sensors fabricated in this thesis showed an MI ration of up to 100%.

3- Characterization of CoSiB material for GMI applications

CoSiB was studied and developed to be employed as a GMI material and enhance the performance of multilayer GMI structures. This study is a complimentary investigation of post-processing treatment and concludes the optimal post-processing treatment to achieve the best performance of the GMI sensors. The characterization consists of various material characterization tests as well as magnetic characterization tests. The tested samples were each treated at various dwell times and temperatures. The characterizations show the formation of Co nano-clusters in the matrix of GMI amorphous material as a result of the post-treatment. The formed Co nano-clusters were responsible for the magnetic performance enhancement of these materials. To the best knowledge of the authors, this thesis represents the first general study of the characterization of CoSiB as a GMI material.

6.1 Future Works

This thesis has carried out extensive research and investigations into a wide range of topics, aiming to advance the development of miniature magnetic sensors and giant magneto-impedance phenomena. There are several related research problems in this area that could potentially be explored in the future. Below is a small sample of them:

- Developing an array of MEMS sensors in order to sense multilevel threshold magnetic fields. This can be helpful in applications sensitive to various levels of magnetic fields.

- Integrate an on-chip magnetic coil in order to make the systems testable on-chip and compensate the external magnetic field in necessary cases.
- A more extensive study on the effect of time on the post-processing of GMI materials would be beneficial. This study of time should be related to both the dwell time of treatments and the cooling time of samples.
- Ultimately, a GMI material could be employed as the core magnetic material of MEMS reed sensors, and their performance enhanced with thermal treatment (as addressed in Chapter 5). This integration could result in highly sensitive MEMS reed sensors that can be employed for sensing lower magnetic fields. This could also be an initiative to futher miniaturize the structures from the size achieved in this thesis.

Appendix A

Theory and mathematical equations for MEMS REED Sensors

Hybrid BIE/Poisson approach for magnetostatic analysis

The magnetostatic governing equations are derived from Maxwell's equations and can be written as [8]:

$$\nabla \times \boldsymbol{H} = \boldsymbol{J} \tag{1}$$

$$\nabla . \boldsymbol{B} = 0 \tag{2}$$

where H is the magnetic field intensity, B is the magnetic flux density, and J is the current density. B and H are related by the constitutive relation:

$$\boldsymbol{B} = \mu \boldsymbol{H} = \mu_0 \mu_r \boldsymbol{H} = \mu_0 (\boldsymbol{M} + \boldsymbol{H}) \tag{3}$$

where $\mu = \mu_0 \mu_r$ is the permeability of the magnetic material, μ_0 is the permeability of the vacuum and μ_r is the relative permeability of the magnetic material. M is the magnetization [8] of the magnetic material and can be written as:

$$\boldsymbol{M} = (\mu_r - \boldsymbol{1})\boldsymbol{H} = \chi \boldsymbol{H} = \frac{\chi}{\mu}(\boldsymbol{B}) \tag{4}$$

where χ is the magnetic susceptibility. The magnetic material is considered linear when μ_r is constant and nonlinear when

μ_r is a function of the magnetic field. As the magnetic field, B, is divergence-free (Equation (2)), the magnetostatic equations can be expressed using a vector potential, A, as [8]:

$$\nabla \times \left(\frac{1}{\mu_r} \nabla \times \mathbf{A} \right) = \mu_0 \boldsymbol{J} \tag{5}$$

where

$$\mathrm{B} = \nabla \times \boldsymbol{A} \tag{6}$$

For two-dimensional (2D) analysis of a linear homogeneous magnetic material, Equation (5) can be simplified as:

$$\nabla^2 A_z = -\mu J_z \tag{7}$$

where the scalars Az and Jz are the z-components of A and J, respectively, and when the 2D analysis is performed in the X-Y domain. Magnetostatic analysis will be performed by solving Equation (7) in the magnetostatic domain to compute the magnetic field, B, from which the magnetostatic body force (needed in the mechanical analysis) can be computed.

Magnetostatic MEMS switches and relays typically operate in the linear region of magnetic materials [4-5], where μ_r is constant and attractive forces are present. Hence, the linear analysis can be applied for those cases assuming no magnetic dispersion, hysteresis and anisotropy in the magnetic materials. However, the nonlinearity in the magnetic material property $\mu_r = \mu_r(H)$ can easily be incorporated into the hybrid Lagrangian framework, like what COMSOL is doing in the FEM analysis of magnetostatic forces. In this case, Equation (7) would be nonlinear in nature and can be solved using a Newton method.

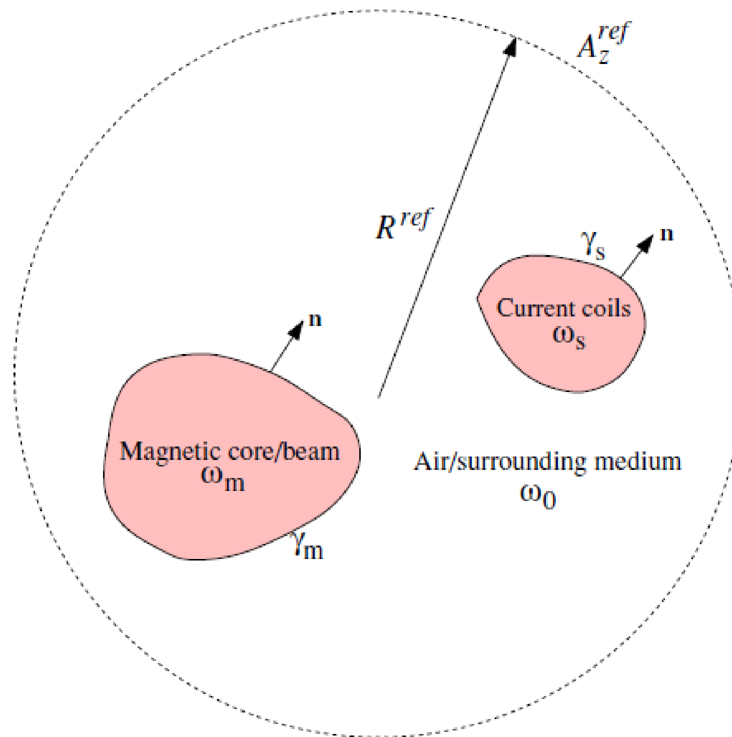

Figure 0-1 The three basic subdomains typically present at magnetic MEMS [8].

Figure 3-2 shows the three basic subdomains typically present in magnetostatic MEMS at any instant in time in their deformed configuration. All magnetic cores and deformable magnetic beams/microstructures (generally, they are ferromagnetic materials with high permeability μ) are denoted by ω_m ($J_z = 0$ in these domains), γ_m is the boundary of ω_m, ω_s represents all the current carrying coils/conductors ($J_z \neq 0$ in these domains), γ_s is the boundary of ω_s, and ω_0 represents the surrounding medium (air or vacuum) whereJ_z is zero. ω_0 also includes any nonmagnetic materials present in the device, such as the substrate shown in Figure 1. Equation (7) is valid in each subdomain and the interface conditions (derived from the integral form of Maxwell's equations) on the boundaries between the subdomains are given by [8].

$$A_z \mid_{\omega_m} = A_z \mid_{\omega_0} \quad and \quad \frac{1}{\mu_m}\frac{\partial A_z}{\partial n} \mid_{\omega_m} = \frac{1}{\mu_0}\frac{\partial A_z}{\partial n} \mid_{\omega_0} \quad on\ \gamma_m \tag{8}$$

$$A_z \mid_{\omega_s} = A_z \mid_{\omega_0} \quad and \quad \frac{1}{\mu_s}\frac{\partial A_z}{\partial n} \mid_{\omega_s} = \frac{1}{\mu_0}\frac{\partial A_z}{\partial n} \mid_{\omega_0} \quad on\ \gamma_s \tag{9}$$

where, for example, $A_z \mid_{\omega_m} = A_z \mid_{\omega_0}$ on γ_m means that the value of A_z obtained by solving the Poisson equation in ω_m and the value of A_z obtained by solving the BIE in ω_0 should be the same on the interface/boundary between ω_m and ω_0, which is γ_m. n is the unit normal in the outward direction, as shown in Figure 2, andμ_m , μ_s and μ_0 are the magnetic permeabilities of the subdomains ω_m, ω_s and ω_0, respectively. The key idea in a hybrid approach for magnetostatic analysis is to solve a boundary integral form of Equation (7) for $J_z = 0$, i.e., $\nabla^2 A_z = 0$, for the unbounded/exterior subdomain, ω_0 , and the Poisson equation (i.e., Equation (7) with $J_z \neq 0$) for the interior subdomains, ω_m and ω_s (see [8] and [39] for details). The subdomains are then coupled to each other using the interface conditions Equations (8) and (9). The boundary integral form of the Laplace equation $\nabla^2 A_z = 0$ for ω_0 is given by [8] (and many basic FEM books):

$$cA_z(x) = \int_{\gamma} A_z(x')\frac{\partial G(x,x')}{\partial n'}\,d\gamma(x') - \int_{\gamma} \frac{\partial A_z(x')}{\partial n'}G(x,x')\,d\gamma(x') + A_z^{ref} \tag{10}$$

$$\int_{\gamma} \frac{\partial A_z(x')}{\partial n'}\,d\gamma(x') = 0 \tag{11}$$

where x is the source point and x' is the field point on the boundary of the subdomains $\gamma = \gamma_m \cup \gamma_s$. c is the corner tensor (c = 1/2 for smooth boundaries [1]), n' is the unit normal in the outward direction at the point x', and G is Green's function. In two dimensions, $G(x, x') = -\ln|x - x'|/2\pi$, where $|x - x'|$ is the is the distance between the source point x and the field point x', and A_z^{ref} is the reference potential (it is the potential at infinity in this case).

At the boundaries γ_m and γ_s, the value of A_z obtained from the BIEs (Equations (10) and (11), solved for the subdomain ω_0) serves as a boundary condition for solving the Poisson equation (Equation (7)) in the subdomains ω_m and ω_s. On the other hand, the normal derivative of A_z, i.e., $\frac{\partial A_z}{\partial n}$, on the boundaries γ_m and γ_s obtained by solving Equation (7) in the

subdomains ω_m and ω_s, respectively, gives the value of $\frac{\partial A_z}{\partial n}$ in the BIEs (Equations (10) and (11), solved for the subdomain ω_0) through equations (8) and (9). A self-consistent solution for the magnetic vector potential, A_z, is obtained by solving the coupled BIE/Poisson problem. As the value of A_z is not specified at any point in the magnetostatic domain, the value of A_z obtained by solving Equations (7), (10) and (11) along with the interface conditions equations (8) and (9) is not unique, although the value of the magnetic flux density, B, obtained is unique [8],[14]. A unique solution of A_z is obtained by fixing the value of A_z at some points in the magnetostatic domain.

Lagrangian formulation

One of the drawbacks of the approach described above and also of the conventional tools for magnetostatic analysis is that the magnetostatic equations are written in the deformed configuration of the domains (Figure 3-3 shows the subdomains in the deformed configuration). As a result, when the microstructure deforms under the application of the magnetostatic force, the geometry has to be updated, rediscretized and the numerical interpolations recalculated before any analysis can be performed. This significantly increases the computational cost. In this report, a Lagrangian formulation of the hybrid magnetostatic equations under arbitrary deformation is presented for efficient analysis of magnetostatic MEMS.

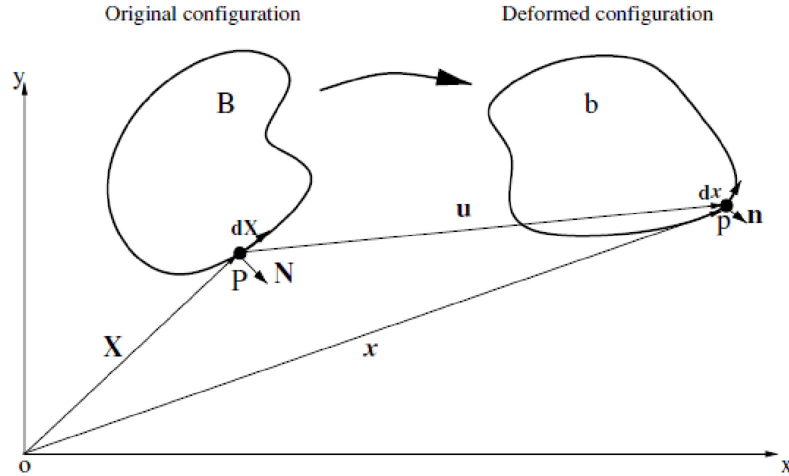

Figure 0-2 Various configurations of a deformed body [8].

When a material body is subjected to a force, either internal or external, its geometrical shape undergoes a change. As shown in Figure 3, the initial or the undeformed configuration of a body is denoted by B (all quantities in the initial configuration are denoted by capital letters) and the deformed configuration of the body is denoted by b (all quantities in the deformed configuration are denoted by lower case letters). Consider an infinitesimal segment on the boundary of B. Let P be the point where the infinitesimal boundary segment is directed from, X be the position vector of P, dX be the vector representing the infinitesimal boundary segment, and N be the unit outward normal at P. When the body deforms from B to b, point P moves to p and its position changes to x. The boundary segment, dX, and the unit outward normal, N, in the initial configuration deform to dx and n in the deformed configuration, respectively. Note that the boundary segment changes not only in length but also in direction when it deforms. The displacement from P to p is denoted by vector u. The physical quantities in the deformed configuration can be expressed by the corresponding physical quantities in the initial configuration (Lagrangian description), as described below [8]:

$$x = \mathbf{X} + \mathbf{u} \tag{12}$$

$$x = \boldsymbol{F} d\boldsymbol{X} \tag{13}$$

$$\mathbf{X} = \boldsymbol{F}^{-1} dx \tag{14}$$

where F is the deformation gradient tensor [8]. The relation between the unit outward normal at the point x in the deformed configuration, n, and the unit outward normal at the point X in the initial configuration, N, is given by Nanson's law [8]:

$$\mathbf{n}\mathrm{d}\gamma = \bar{J}\boldsymbol{F}^{-\boldsymbol{T}}\boldsymbol{N}d\Gamma \tag{15}$$

where dΓ is the length of the infinitesimal boundary segment, dX, in the initial configuration and dγ is the length of the boundary segment, dx, in the deformed configuration (see Figure 3), and $\bar{J} = \det(F)$. Further, using Nanson's law, the following relation between dΓ and dγ can be derived [8]:

$$\mathrm{d}\gamma = \bar{J}\left|\boldsymbol{F}^{-\boldsymbol{T}}\boldsymbol{N}\right|d\Gamma = (\mathbf{T}.\mathbf{CT})^{\frac{1}{2}}d\Gamma \tag{16}$$

where $C = F^T F$ is the Green deformation tensor and T and N are the unit tangential and the normal vectors in the undeformed configuration, respectively. By using the chain rule and Equation (14), the gradient of a physical quantity φ in the deformed configuration can be expressed as [8]:

$$\nabla_x \phi = \boldsymbol{F}^{-\boldsymbol{T}}\nabla_X \phi \tag{17}$$

where $\nabla_X \phi$ and $\nabla_x \phi$ denote the gradient of ϕ in the initial and the deformed configurations, respectively. Equation (17)

shows that the differential operator ∇_x in the deformed configuration can be rewritten in the initial configuration as

$$\nabla_x = \boldsymbol{F}^{-\boldsymbol{T}}\nabla_X \tag{18}$$

The normal derivative of a physical quantity ϕ in the deformed configuration can also be rewritten as [8]:

$$\frac{\partial \phi}{\partial \mathrm{n}} = \nabla_x \phi.\mathbf{n} = \boldsymbol{F}^{-\boldsymbol{T}}\nabla_X \phi \,.\frac{\boldsymbol{F}^{-\boldsymbol{T}}\boldsymbol{N}}{|\boldsymbol{F}^{-\boldsymbol{T}}\boldsymbol{N}|} = \nabla_X \phi \,.\frac{\boldsymbol{F}^{-\boldsymbol{1}}\boldsymbol{F}^{-\boldsymbol{T}}\boldsymbol{N}}{|\boldsymbol{F}^{-\boldsymbol{T}}\boldsymbol{N}|} \tag{19}$$

By using the above relations, the geometry of a deformed structure and the differential operators defined on the deformed structure can be expressed in terms of the geometry and the differential operators in the initial configuration and its deformation information.

The Poisson equation (Equation (7)), which is stated in the deformed configuration, can be transformed into the initial configuration by substituting Equation (18) into Equation (7), which can then be rewritten in the Lagrangian form as:

$$\left(\boldsymbol{F}^{-\boldsymbol{T}}\nabla_X\right).\left(\boldsymbol{F}^{-\boldsymbol{T}}\nabla_X A_z\right) = -\mu J_z \tag{20}$$

Note that, in Equation (20), all of the quantities are mapped to the initial or the undeformed configuration. Next, Equations (10) and (11) are mapped to the initial configuration by representing each component in Equations (10) and (11) by its counterpart in the initial configuration. Using Equation (12), Green's function in two dimensions, $G(x, x')$, can be rewritten as

$$G(x, x') = G(x(\boldsymbol{X}), x'(\boldsymbol{X}')) = \frac{1}{2\pi} ln|X - X' + u - u'| \tag{21}$$

where X and X' are the source and the field points in the initial configuration corresponding to the source and the field points x and x' in the deformed configuration, x(X) denotes x in the deformed configuration mapped to X in the initial configuration with the mapping x = X + u, and u and u' are the displacements of points X and X', respectively.

For magnetostatic MEMS analysis, these displacements are computed by a mechanical analysis. The normal derivative of

Green's function can be rewritten as [8]:

$$\frac{\partial G(x, x')}{\partial \boldsymbol{n}'} = \nabla_{x'} G(x, x').\boldsymbol{n}' = \begin{Bmatrix} -\dfrac{X - X' + u - u'}{2\pi|X - X' + u - u'|^2} \\ -\dfrac{Y - Y' + v - v'}{2\pi|X - X' + u - u'|^2} \end{Bmatrix}.\boldsymbol{n}' \tag{22}$$
$$= \nabla_{X'} G(x(\boldsymbol{X}), x'(\boldsymbol{X}')).\boldsymbol{n}'$$

where u and u' are the X-displacements of the points X and X', respectively, and v and v' are the Y-displacements of the points X and X', respectively. By using Equations (16) and (19), the Lagrangian form of the second term on the right-hand side of Equation (10) can be written as

$$\int_{\gamma} \frac{\partial A_z(x')}{\partial n'} G(x,x')\, d\gamma(x') \tag{23}$$

$$= \int_{\Gamma} [\nabla_{X'} A_z(x'(\boldsymbol{X}')) \,.\, \frac{\boldsymbol{F}^{-1}(\boldsymbol{X}')\boldsymbol{F}^{-T}(\boldsymbol{X}')\boldsymbol{N}(\boldsymbol{X}')}{|\boldsymbol{F}^{-T}(\boldsymbol{X}')\boldsymbol{N}(\boldsymbol{X}')|}$$

$$\times G(x(\boldsymbol{X}), x'(\boldsymbol{X}'))(\mathbf{T}(\boldsymbol{X}').\, \mathbf{C}(\boldsymbol{X}')\mathbf{T}(\boldsymbol{X}'))^{\frac{1}{2}} d\Gamma(\boldsymbol{X}')$$

where Γ is the undeformed configuration of the boundary γ , which is in the deformed configuration. By using equations (15) and (22), the Lagrangian form of the first term on the right-hand side of Equation (10) can be rewritten as

$$\int_{\gamma} A_z(x') \frac{\partial G(x,x')}{\partial n'} d\gamma(x') = \int_{\gamma} A_z(x'(\boldsymbol{X}')) \,.\, \nabla_{x'} G(x(\boldsymbol{X}), x'(\boldsymbol{X}')).\, \boldsymbol{n}' d\gamma(x') \tag{24}$$

$$= \int_{\Gamma} A_z(x'(\boldsymbol{X}'))\, \nabla_{X'} G(x(\boldsymbol{X}), x'(\boldsymbol{X}')).\, \bar{J}(\boldsymbol{X}')\boldsymbol{F}^{-T}(\boldsymbol{X}')\boldsymbol{N}(\boldsymbol{X}') d\Gamma(\boldsymbol{X}')$$

Substituting Equations (23) and (24) into Equation (10), the Lagrangian form of Equation (10) is given by

$$CA_z(x(\boldsymbol{X})) = \int_{\Gamma} A_z(x'(\boldsymbol{X}'))\, \nabla_{X'} G(x(\boldsymbol{X}), x'(\boldsymbol{X}')).\, \bar{J}(\boldsymbol{X}')\boldsymbol{F}^{-T}(\boldsymbol{X}')\boldsymbol{N}(\boldsymbol{X}') d\Gamma(\boldsymbol{X}') + {A_z}^{ref} \tag{25}$$

$$- \int_{\Gamma} [\nabla_{X'} A_z(x'(\boldsymbol{X}')) \,.\, \frac{\boldsymbol{F}^{-1}(\boldsymbol{X}')\boldsymbol{F}^{-T}(\boldsymbol{X}')\boldsymbol{N}(\boldsymbol{X}')}{|\boldsymbol{F}^{-T}(\boldsymbol{X}')\boldsymbol{N}(\boldsymbol{X}')|}$$

$$\times G(x(\boldsymbol{X}), x'(\boldsymbol{X}'))(\mathbf{T}(\boldsymbol{X}').\, \mathbf{C}(\boldsymbol{X}')\mathbf{T}(\boldsymbol{X}'))^{\frac{1}{2}} d\Gamma(\boldsymbol{X}')$$

The Lagrangian form of equation (11) is given by:

$$\int_{\Gamma} [\nabla_{X'} A_z(x'(\boldsymbol{X}')) \,.\, \frac{\boldsymbol{F}^{-1}(\boldsymbol{X}')\boldsymbol{F}^{-T}(\boldsymbol{X}')\boldsymbol{N}(\boldsymbol{X}')}{|\boldsymbol{F}^{-T}(\boldsymbol{X}')\boldsymbol{N}(\boldsymbol{X}')|} \times \left(\mathbf{T}(\boldsymbol{X}').\, \mathbf{C}(\boldsymbol{X}')\mathbf{T}(\boldsymbol{X}')\right)^{\frac{1}{2}} d\Gamma(\boldsymbol{X}') = 0 \tag{26}$$

In the hybrid full-Lagrangian BIE/Poisson technique for magnetostatic analysis presented in this thesis, Equation (20) is solved in the undeformed configuration of the magnetostatic subdomains ω_{m} and ω_{s} and equations (25) and (26) are solved for the subdomain ω_0 on the

undeformed configuration of the boundaries γ_m and γ_s. Equations (8) and (9) can be written in the Lagrangian form using Equation (19) in a straightforward manner and are applied as boundary conditions on the undeformed configuration of the boundaries γ_m and γ_s.

Once A is computed from the magnetostatic analysis, the magnetic field, B, can be computed using the relation $B = F^{-T}\nabla_X \times A$ (derived from Equation (6)). In the case of 2D analysis performed in the X-Y domain, the magnetic field, B, consists of the terms BX and BY (as BZ = 0), which can be computed as

$$\boldsymbol{B} = \begin{Bmatrix} B_X \\ B_Y \end{Bmatrix} = \boldsymbol{F}^{-\boldsymbol{T}} \begin{Bmatrix} \frac{\partial A_z}{\partial Y} \\ -\frac{\partial A_z}{\partial X} \end{Bmatrix} = \begin{bmatrix} 1 + \frac{\partial u}{\partial X} & \frac{\partial u}{\partial Y} \\ \frac{\partial v}{\partial X} & \mathbf{1} + \frac{\partial v}{\partial Y} \end{bmatrix}^{-\boldsymbol{T}} \begin{Bmatrix} \frac{\partial A_z}{\partial Y} \\ -\frac{\partial A_z}{\partial X} \end{Bmatrix} \tag{27}$$

The magnetostatic body force f_{mag} acting on the microstructure in the deformed configuration can be computed as [8]

$$f_{mag} = \boldsymbol{M}.\nabla_x \boldsymbol{B} = \boldsymbol{M}.\boldsymbol{F}^{-\boldsymbol{T}}\nabla_X \boldsymbol{B} \tag{28}$$

where M can be computed from B using Equation (4). In the Lagrangian formulation, the force is mapped back to the undeformed geometry using [8]:

$$F_{mag} = \bar{J} f_{mag} = \bar{J}\boldsymbol{M}.\boldsymbol{F}^{-\boldsymbol{T}}\nabla_X \boldsymbol{B} \tag{29}$$

where F_{mag} is the magnetostatic body force in the undeformed configuration.

For mechanical resorting force, one can find out the spring constant of the beams based on mechanical strength equations and beam dimensions. The equations for various kinds of beams are different. For instance, for a simple cantilever beam, the spring constant is:

$$K = \frac{3EI}{L^3} \tag{30}$$

where E is Young's modulus of beam material, L is beam length and I is moment of inertia of corresponding beam. A cantilever beam can be calculated by (31):

$$I = \frac{wt^3}{12} \tag{31}$$

where w is beam width and t is beam thickness. After calculating the spring constant of the beam, mechanical restoring force can be calculated using Hooks law:

$$F_{mech} = ky \tag{32}$$

Once the magnetic body force is sufficiently high to overcome F_{mech} value in y=gap, the switch will be actuated. It should be noted that more complicated beam models can be employed to calculate mechanical forces, but response errors are negligible between various models. It is also important to note that the spring constant equation will change by altering beam and support shapes.

Appendix B

The design has been developed based on UW-MEMS rules and is briefly described below:
Design rules identify the physical limitations of individual process steps. These rules are extremely important and need to be considered at the design stage. If the guidelines are not respected, the device will not meet the specifications and thus will most likely fail or malfunction.

Generally there are two types of rules. The first type of rule specifies minimum feature and gap sizes. Minimum feature size refers to the minimum width of a trace that will be feasible using the current process. In other words, if this rule is violated, there is no guarantee that the feature will be produced on the wafer. In the same way, the minimum gap specifies the shortest separation distance between two adjacent features. Failure to follow this rule results in a merged feature consisting of the later patterns. The second type of rules specifies crossovers and inter-level spacing. This relates to the alignment of the layers and will be detailed shortly. Both rule types are considered in our study and are reported below.

1-Nickel- bottom electrode

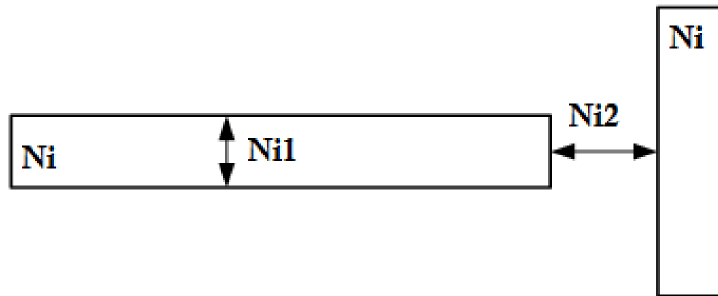

Figure 0-1 Bottom electrode design rules.

Description	Rule Label	Value(μm)
Minimum width/length	Ni1	≥ 60
Minimum distance	Ni2	≥ 60

2-Anchors

Description	Rule Label	Value(μm)

Minimum width/length	anch	≥ 20
Layer 1 overlap with anchor	Ni-anch	≥ 15

3-Dimples

Description	Rule Label	Value(μm)
Minimum width/length	Dimp	≥ 10
Minimum distance	Dimp1	≥ 15

4-Upper beam

Description	Rule Label	Value(μm)
Minimum width/length	Beam1	≥ 15
Layer 1 overlap with layer 4	Beam2	≥ 10
Layer 4 overlap with anchor	Beam-anch	≥ 15

Appendix C

Detailed Microfabrication recipe used for MEMS Reed sensors

1. Create Alumina/Glass/Silicon Superstrate 2.5" square wafers
    - Naming: #1, #2, #3, #4
2. RCA
    - Ratio = 650:130:130 $H_2O:NH_4OH:H_2O_2$
    - Temperature = Bubbling!
    - Time = 15:00
3. Dehydrate
    - Time = 04:00
    - Temperature = 120 ^{0}C
4. INTLVAC Cr/Au
    - 40 nm Cr (e-beam)
    - 70 nm Au (e-beam)
5. Mask "L1"
    - AZ 3330
        - FT = 2 μm
        - Step 1 of 3: 100 RPM for 10 sec.
        - Step 2 of 3: 500 RPM for 10 sec.
        - Step 3 of 3: 3000 RPM for 30 sec.
    - Soft Bake at 110 ^{0}C for 60 sec.
    - Exposure:
        - Intensity at 365 nm = 26 mW.cm^{-2}
        - Time = 4 sec.
    - Post Exposure Bake at 110 ^{0}C for 60 sec.
    - Develop in AZ 300 MIF for 60 sec.
    - Hard Bake at 110 ^{0}C for 120 sec.
6. Wet Etch Cr/Au:

Cr etchant:

W2: 20S+10S+5S. All with agitation. Wash the wafer every time before immersing in the etchant.

Au Etchant for 30 S

7. ELP Ni
    - ELP solution heat to 92C with steering
    - A dommy gold wafer has been placed in oxygen plasma RIE for 1 min (pres:30, O2:30, RIE:50, ICP:50, time:60)
    - Then put in EN plating solution(seems that free electrons resulted from RIE will help initiating of palting) for one minute, plating was done for 0.6 um and roughness was good
    - Total 3um has been deposited.
    - A dektak measurement of thickness is done after deposition each layer.

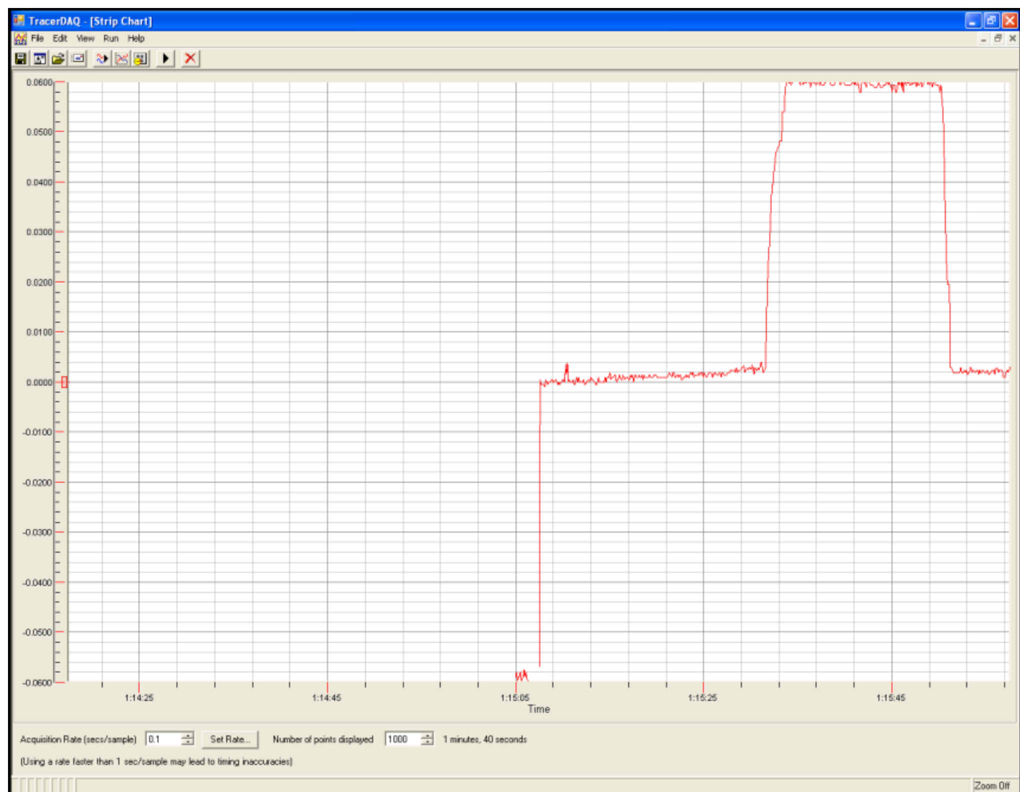

Figure 0-1 Dektak of first layer (Ni) with 0.5KÅ tip, in the above fig , 6 units are covered which results to 3 um

8. Gold Electroless
    - Heating the solution to 70-75 degree the rate is 25nm per min(2 min I used)
9. Polyimide Preparation $\{W_1, W_2, W_3, W_4\}$
    - Spinning:
        - **ADD Aluminum Foil**
        - FT = 2.7 μm
        - Step 1 of 3: 100 RPM for 10 sec.
        - Step 2 of 3: 500 RPM for 10 sec.
        - Step 3 of 3: 1300 RPM for 40 sec.
    - First Bake at 90 ^{0}C for 2:00
    - Second Bake at 150 ^{0}C for 2:00
    - Cure in furnace:
        - 25 ^{0}C - 150 ^{0}C
            - Time = 40:00
        - 150 ^{0}C - 350 ^{0}C
            - Time = 50:00
        - 350 ^{0}C - 350 ^{0}C
            - Time = 30:00
        - 350 ^{0}C - 150 ^{0}C
            - Time = 40:00
        - 150 ^{0}C - 25 ^{0}C
            - Time = 2:00:00
10. Patterning Anchor
    - AZ nLOF 2035
        - FT = 2.6 μm
        - Step 1 of 3: 100 RPM for 10 sec.
        - Step 2 of 3: 500 RPM for 10 sec.
        - Step 3 of 3: 2500 RPM for 30 sec.
    - Soft Bake at 110 ^{0}C for 60 sec.
    - Exposure:
        - Intensity at 365 nm = 26 $mW.cm^{-2}$
        - Time = 3 sec.

- Post Exposure Bake at 110 ^{0}C for 60 sec.
- Develop in MIF 300 for 120 sec.
- Hard Bake at 120 ^{0}C for 120 sec.

11. Dry Etch PI to pattern anchor

    RIE O2 plasma on W1, W3 and W5

    - Pressure = 50
    - ICP = 150
    - RIE = 50
    - O2 = 30
    - Wafers needed some O2 plasma to clean them from sturdy resist spots
    - Time = 30 sec.
    - Wafers look BETTER.

12. Dry etch Dimple like step 10

13. Gold Sputtering

    Intelvac 0.1um GOLD, SPUTTERING

14. Final mask patterning
15. Wet etch gold 25 Sec
16. ELP Ni for 3 min
17. ELP Gold for 2 min
18. PR coating BEFORE dicing
    - Spin AZ 3330 using 500 RPM for 15 sec. then 2000 RPM for 45 sec.
    - Bake at 110^{0}C for 3 min.
19. EKC of devices
    - 30 min. (more than 20 min. to guarantee the release)
    - 60 C
20. IPA of W3 devices
    - Total time = 3*8:00 min.
21. CO2 CPD of devices
    - The whole chamber, glass, carrier and lid are cleaned with IPA
    - A new cylinder is being used
    - 4 different designs of W3 devices are inside the chamber for CPD release

- CPD process was successful

Bibliography

[1] J. Lenz and A. S. Edelstein (2006), "Magnetic Sensors and Their Applications", IEEE Sensors Journal, 6(3), pp. 631-649.

[2] P. Ripka (2001). Magnetic Sensors and Magnetometers. Artech House, Norwood, MA.

[3] R. L. Fagaly (2006), "Superconducting quantum interference device instruments and applications", Rev. Sci. Instrum., 77, pp. 101-145.

[4] L. D. Landau and E. M. Lifshitz (1960). Electrodynamics of Continuous Media. Pergamon Press, Oxford.

[5] G. T. Rado and V. J. Folen (1961), "Observation of the Magnetically Induced Magnetoelectric Effect and Evidence for Antiferromagnetic Domains", Phys. Rev. Lett., 7, pp. 310-311.

[6] R. Ramesh and N. A. Spaldin (2007), "Multiferroics: progress and prospects in thin films", Nature Mater, 6, pp. 21-29.

[7] W. Eerenstein, N. D. Mathur, and J. F. Scott (2006) "Multiferroic and magnetoelectric materials", Nature, 442, pp. 759-765.

[8] S. De and N. Aluru, "A hybrid full-Lagrangian technique for the static and dynamic analysis of magnetostatic MEMS", Journal of Micromechanics and Microengineering, 16 (2006) 2646-2658.

[9] M. Tang, Y. Lee, R. Kumar, R. Shankar, and O. Neel, "A MEMS Micro-Reed Switch Designed for Portable Applications", Transducers'11, Beijing, China, June 5-9, 2011.

[10] M. Tang, E. Liao, Ch. Cheng, D. Lee,Y. Lee, R. Kumar, R. Shankar, O. Neel, G. Noviello, and F. Italia, "A Magnetostatic MEMS Switch Designed for Portable Applications", Journal Of Microelectromechanical Systems, Vol. 19, No. 5, October 2010.

[11] S. Marauska, R. Jahn, H. Greve, E. Quandt, R. Knochel, and B. Wagner, " MEMS magnetic field sensor based on magnetoelectric composites", Journal of Micromechanics and Microengineering, Vol. 22, No. 6.

[12] M. Tang, E. Liao, Ch. Cheng, D. Lee,Y. Lee, R. Kumar, R. Shankar, O. Neel, G. Noviello, and F. Italia, "A MEMS Microreed Switch with One Reed Embedded in the Silicon Substrate", JMEMS, Vol. 20, Issue 6.

[13] H. Yanga, N. Myung, J. Yeea, Y. Park, B. Yoob, M. Schwartz, K. Nobe, and J. Judya, "Ferromagnetic micromechanical magnetometer", Sensors and Actuators, 2002, Vol. 97.

[14] D. DiLellaa, L. J. Whitmana, R. J. Coltona, and T. W. Kenny, "A micromachined magnetic-field sensor based on an electron tunneling displacement transducer", Sensors and Actuators, 2000, Vol. 86.

[15] R. B. Givens, J. C. Murphy, R. Osiander, T. J. Kistenmacher, and D. K. Wickenden, "A high sensitivity, wide dynamic range magnetometer designed on a xylophone resonator", Applied Physics Letter, 1996, Vol. 96.

[16] A. S. Edelstein and G. A. Fischer, "Minimizing 1/f noise in magnetic sensors using a microelectromechanical system flux concentrator", J. Appl. Phys., Vol. 91, pp. 7795-7797, 2002.

[17] H. H. Gatzen, E. Obermeier, T. Kohlmeier, T. Budde, H. D. Ngo, B. Mukhopadhya, and M. Farr 2003, "An electromagnetically actuated bi-stable MEMS optical microswitch", Int. Conf. on Solid-State Sensors and Actuators: Transducers, pp. 1514-7.

[18] Z. Nami, C. H. Ahn, and M. G. Allen, 1996, "An energy-based design criterion for magnetic microactuators", J. Micromech. Microeng. 6 337-44.

[19] A. Frangi, P. F. Ragani, and L. Ghezzi, 2005, "Magneto-mechanical simulations by a coupled fast multipole method-finite element method and multigrid solvers", Comput. Struct. 83 718-26.

[20] A. Nicolet, F. Delince, A. Genon, and W. Legros, 1992, "Finite elements-boundary elements coupling for the movement modeling in two dimensional structures", J. Physique III 2 2035-44

[21] M.-H. Phan and H.-X. Peng. Progress in Materials Science. 53 (2008) 323-420.

[22] J. E. Lenz, "A review of magnetic sensors", Proc IEEE 1990;78:973-89.

[23] T. Meydan. Application of amorphous materials to sensors. J Magn Magn Mater 1995;133:525-32.

[24] P. Ripka, "Magnetic sensors and magnetometers", Artech House Publishers, 2001.

[25] L. V. Panina and K. Mohri. Magneto-impedance effect in amorphous wires. Appl Phys Lett 1994;65:1189-91.

[26] L. V. Panina, K. Mohri, T. Uchiyama, and M. Noda. Giant magneto-impedance in Co-rich amorphous wires and films. IEEE Trans Magn 1995;31:1249-60.

[27] M. Vazquez and A. Hernando. A soft magnetic wire for sensor applications. J Phys D: Appl Phys 1996;29:939-49.

[28] H. Chiriac and T. A. Ovari. Amorphous glass-covered magnetic wires: preparation, properties, applications. Prog Mater Sci 1996;40:333-407.

[29] M. Vazquez. Giant magnetoimpedance in soft magnetic ‘‘wires’’. J Magn Magn Mater 2001;226-230:693-9.

[30] M. Knobel and K. R. Pirota. Giant magnetoimpedance: concepts and recent progress. J Magn Magn Mater 2002;242-245:33-40.

[31] M. Knobel, M. Vazquez, and L. Kraus. Giant magnetoimpedance. In: Buschow KH, editor. Handbook of magnetic materials, Vol. 15. Amsterdam: Elsevier Science B.V.; 2003. pp. 1-69 [Chapter 5].

[32] L. Kraus. GMI modeling and material optimization. Sens Acta A 2003;106:187-94.

[33] C. Tannous and J. Gieraltowski. Giant magneto-impedance and its applications. J Mater Sci: Mater Electro 2004;15:125-33.

[34] K. Mohri, T. Kohsawa, K. Kawashima, H. Yoshida, and L. V. Panina. Magneto-inductive effect (MI effect) in amorphous wires. IEEE Trans Magn 1992;28:3150-2.

[35] D. Menard, M. Britel, P. Ciureanu, and A. Yelon. Giant magnetoimpedance in a cylindrical magnetic conductor. J Appl Phys 1998;84:2805-14.

[36] A. Yelon, D. Menard, M. Brittel, and P. Ciureanu. Calculations of giant magnetoimpedance and of ferromagnetic resonance response are rigorously equivalent. Appl Phys Lett 1996;69:3084-5.

[37] L. V. Panina and K. Mohri, “Magneto-Impedance in Multilayer Films”, 2000, Sensors and Actuators A, Vol. 81, 71-76.

[38] T. Morikawa, Y. Nishibe, H. Yamadera, Y. Nonomura, M. Takeuchi, and Y. Taga, “Giant Magneto-Impedance Effect in Layered Thin Films”, IEEE Transactions on Magnetics, Vol. 33, 1997.

[39] Z. Ren, F. Bouillault, A. Razek, and J. C. Verite, “Comparison of different boundary integral formulations when coupled with finite elements in three dimensions”, IEE Proc., 1988, 135 501-7.

[40] Y. Hui, T. X. Nan, N. X. Sun, and M. Rinaldi, (2013, January). MEMS resonant magnetic field sensor based on an AlN/F e G a B bilayer nano-plate resonator. In *Micro Electro Mechanical Systems (MEMS), 2013 IEEE 26th International Conference on* (pp. 721-724). IEEE.

[41] C. I. Chang, M. H. Tsai, C. M. Sun, and W. Fang, (2014). Development of CMOS-MEMS in-plane magnetic coils for application as a three-axis resonant magnetic sensor. *Journal of Micromechanics and Microengineering*, *24*(3), 035016.

[42] S. Park, M. S. Al-Ghamdi, M. Khater, E. Abdel-Rahman, and M. Yavuz, (2014, August). Adjustable Sensitivity MEMS Magnetic Sensor. In *ASME 2014 International Design Engineering Technical Conferences and Computers and Information in Engineering Conference* (pp. V004T09A016-V004T09A016). American Society of Mechanical Engineers.

[43] S. Gudoshnikov, N. Usov, A. Nozdrin, M. Ipatov, A. Zhukov, and V. Zhukova, (2014). Highly sensitive magnetometer based on the off-diagonal GMI effect in Co-rich glass-coated microwire. *physica status solidi (a)*, *211*(5), 980-985.

[44] S. NazariNejad, A. Akhavan Fomani and R. Mansour, 'Giant Magneto-Impedance Thin Film Magnetic Sensor', IEEE Transactions on Magnetics, vol. 49, no. 7, pp. 3874-3877, 2013.

[45] S. NazariNejad, A. A. Fomani, & R. R. Mansour "Multilayer Giant Magneto-Impedance sensor for low field sensing", IEEE SENSORS 2013, IEEE (pp. 1-4). November 2013.

[46] F. Barazandeh, S. NazariNejad, R. Nadafi, A. MehdiAbadi and Z. Ghasemi, 'Design and microfabrication of a compliant microgripper using nonbrittle and biocompatible material', *Proceedings of the Institution of Mechanical Engineers, Part C: Journal of Mechanical Engineering Science*, vol. 227, no. 12, pp. 2886-2896, 2013.

[47] M. Hajhashemi, F. Barazandeh, S. Nejad and R. Nadafi DB, 'Design and microfabrication of a constant-force microgripper', *Proceedings of the Institution of Mechanical Engineers, Part C: Journal of Mechanical Engineering Science*, vol. 225, no. 11, pp. 2739-2748, 2011.

[48] R. Nadafi DB, S. Nazari Nejad, M. Kabganian and A. Dinparast Djadid, 'Adaptive control of a legged capsular microrobot based on Lyapunov stability criteria', *Proceedings of the Institution of Mechanical Engineers, Part C: Journal of Mechanical Engineering Science*, vol. 226, no. 4, pp. 887-899, 2011.

[49] H. Parsaiyan, F. Barazandeh, S. Nazari Nejad, S. Rezaei, M. Kabganian, M. Parsaiyan and M. Safdari, 'Theoretical and experimental study of a novel microfabricated fibrillar structure', *Proceedings of the Institution of Mechanical Engineers, Part L: Journal of Materials: Design and Applications*, vol. 224, no. 4, pp. 199-207, 2010.

[50] Reza Nadafi, D. B., S. N Nejad, M. Kabganian, & F. Barazandeh, (2010, May). "Neural network calibration of a semiconductor metal oxide micro smell sensor" , Test Integration and Packaging of MEMS/MOEMS (DTIP), 2010 Symposium on (pp. 154-157). IEEE.

[51] R. Nadafi, F. Edalatfar, P. Zomorodian, S. N. Nejad, M. Kabganian, & F. Barazandeh, "A comparative design study on in-pipe inspection micro robots using AHP method." Design Test Integration and Packaging of MEMS/MOEMS (DTIP), 2010 Symposium on. IEEE, 2010.

[52] N. Sayyaf, F. Barazandeh, S. N. Nejad, & M. R. Razfar, (2009, December). Design and Fabrication of a Novel Micro Angle Sensor. In 2009 Fifth International Conference on MEMS NANO, and Smart Systems (pp. 37-40). IEEE.

[53] C. Dong; S. Chen; T. Y. Hsu, "A simple model of giant magneto-impedance effect in amorphous thin films." Journal of magnetism and magnetic materials 250 (2002): 288-294.

[54] E. Costa Silva; L. Gusmão; L. Hall; E. Costa Monteiro, "Magnetic field transducers based on the phase characteristics of GMI sensors and aimed at biomedical applications", 13TH International Conference on Biomedical Engineering, 2009, Singapore.

[55] A. García-Arribas; J. M. Barandiaran; D. De Cos, (2008), Finite element method calculations of GMI in thin films and sandwiched structures: size and edge effects. Journal of Magnetism and Magnetic Materials, 320(14), e4-e7.

[56] L. Kraus, "GMI modeling and material optimization." Sensors and Actuators A: Physical 106.1 (2003): 187-194.

[57] B. Li and J. Kosel, 'Optimized 425MHz passive wireless magnetic field sensor', 2014 IEEE MTT-S International Microwave Symposium (IMS2014), 2014.

[58] R. Popovic, & H. P. Baltes, (1987). U.S. Patent No. 4,700,211. Washington, DC: U.S. Patent and Trademark Office.